

Max-Planck-Institut für Intelligente Systeme
(ehemals Max-Planck-Institut für Metallforschung)
Stuttgart

Microstructure and grain growth of nanosized materials

Gayatri Koyar Rane

Dissertation
an der
Universität Stuttgart

Bericht Nr. 241
Mai 2012

Microstructure and grain growth of nanosized materials

Von der Fakultät Chemie der Universität Stuttgart
zur Erlangung der Würde eines Doktors der Naturwissenschaften (Dr. rer. nat.)
genehmigte Abhandlung

vorgelegt von
Gayatri Koyar Rane
aus Karwar (Karnataka), Indien

Hauptberichter:	Prof. Dr. Ir. E. J. Mittemeijer
Mitberichter:	Prof. Dr. J. Bill
Prüfungsvorsitzender:	Prof. Dr. T. Schleid

Tag der Einreichung:	14.03.2012
Tag der mündlichen Prüfung:	23.05.2012

MAX-PLANCK-INSTITUT FÜR INTELLIGENTE SYSTEME, STUTTGART
(ehemals MAX-PLANCK-INSTITUT FÜR METALLFORSCHUNG)
INSTITUT FÜR MATERIALWISSENSCHAFT DER UNIVERSITÄT STUTTGART

2012

Dedicated to Baba..

Contents

1. Introduction	9
1.1 General Introduction	9
1.2 Nanocrystalline materials fabricated by mechanical attrition	11
1.3 Size dependence of lattice parameter	14
1.4 Grain growth studies.....	14
1.5 Grain growth stabilisation	16
1.6 Main methodology of characterization.....	17
1.6.1 Line-profile decomposition methods.....	18
1.6.1.1 Single-line method	18
1.6.1.2 Williamson-Hall (WH) method	19
1.6.1.3 Warren-Averbach (W-A) method	19
1.6.2 Line profile synthesis method : Whole powder pattern modeling	20
1.6.3 Comparison of the different methods of line-profile analysis	20
1.6.4 X-ray diffraction instrumentation.....	21
1.7 Outline of the thesis.....	22
2. Non-monotonic lattice parameter variation with crystallite size in nanocrystalline ball milled powders.	25
2.1 Introduction.....	26
2.2 Theoretical background.....	28
2.2.1 Lattice contraction	28
2.2.2 Lattice expansion.....	28
2.3 Experimental procedures and data evaluation.....	30
2.3.1 Specimen preparation and processing	30
2.3.2 Microstructure investigation	31
2.3.3 X-ray diffraction measurements and line profile analysis.....	31
2.3.4 Lattice-parameter determination.....	33
2.4 Results	35
2.4.1 Microstructure of the ball-milled powders	35
2.4.2 Grain size-dependence of the lattice parameters	37
2.5 Discussion	38
2.5.1 Microstructural evolution with milling	38
2.5.2 Non-monotonic lattice parameter variation with grain size	39
2.5.3 Fitting lattice contraction and expansion.....	39

2.6	Conclusion	42
3.	Grain growth studies on nanocrystalline Ni powder	45
3.1	Introduction.....	46
3.2	Theoretical background.....	47
3.2.1	Grain-growth kinetics.....	47
3.2.2	X-ray diffraction line-profile analysis.....	49
3.2.2.1	Integral breadth method: Single-line analysis	49
3.2.2.2	Whole powder pattern modelling	50
3.2.2.3	Warren - Averbach method	51
3.3	Experimental details.....	53
3.3.1	Specimen preparation and processing	53
3.3.2	X-ray diffraction measurements.....	53
3.4	Results and Discussion.....	54
3.4.1	Microstructural evolution upon milling.....	54
3.4.2	Microstructural evolution upon annealing.....	56
3.4.2.1	Isothermal grain-growth studies.....	58
3.4.2.2	The grain-size distribution (GSD) upon annealing.....	60
3.4.2.3	Grain-growth kinetics.....	63
3.5	Conclusion	68
4.	The microstructural evolution and thermal stability of nanocrystalline, ball milled Ni – 15 at. % W powder	71
4.1	Introduction:.....	72
4.2	Theoretical background: X-ray diffraction line-profile analysis.....	74
4.2.1	Integral-breadth methods:.....	74
4.2.1.1	Single-line method.....	74
4.2.1.2	Williamson-Hall (WH) method	74
4.2.2	Whole powder pattern modelling	75
4.3	Experimental procedures.....	76
4.3.1	Ball milling.....	76
4.3.2	X-ray diffraction measurements.....	76
4.3.3	Scanning and transmission electron microscopy	77
4.3.4	Differential Scanning Calorimetry.....	78
4.4	Results and discussions.....	78
4.4.1	Microstructural evolution upon milling.....	78
4.4.1.1	Scanning electron microscopy investigations of the milled powders.....	78
4.4.1.2	X-ray diffraction survey scans; W dissolution in Ni	79
4.4.1.3	Line-broadening analysis	81

4.4.2	Microstructural evolution upon annealing after milling: Non-ambient X-ray diffraction measurements	85
4.4.2.1	Line-broadening analysis	85
4.4.2.2	Composition of the Ni(W) solid solution formed on annealing.	91
4.4.2.3	Heat evolution upon annealing after milling; differential scanning calorimetry	91
4.5	Summary	93
5.	Summary.....	95
6.	Zusammenfassung in deutscher Sprache	101
	References.....	107
	Acknowledgements	117
	Curriculum Vitae.....	119

Chapter 1

Introduction

1.1 General Introduction

Nanoscience, a field that has grown continuously in the last three decades, even though already predicted in the late 19th century [1], has been one of the most rapidly growing fields encompassing widely the natural sciences but also increasingly finding links in interdisciplinary fields. Nanocrystalline materials, defined as materials with an average grain/crystallite size typically below 100 nanometers, exhibit unique properties as compared to coarse-grained materials [2-5]. Nanocrystalline materials exhibit variations in properties such as the mechanical behaviour [6-8], improved ductility/toughness [9], elastic modulus, enhanced sintering and alloying ability [10], enhanced diffusivity [11], increased specific heat, higher thermal expansion coefficient, lower thermal conductivity, enhanced magnetic properties [12-14] and different thermodynamic properties [15] in comparison with conventional coarse-grained materials ([16, 17] and references therein).

Hence, possibilities for a wide range of new applications have been revealed which can be achieved by means of controlled manipulation of the crystallite size in the nanometer regime. More insight on these materials was gained by studying the structural and interfacial peculiarities, giving impetus to increased scientific interest and applications-driven technology. The extensive investigations in recent years on structure-property correlations in nanocrystalline materials have begun to unravel the complexities of these materials, and paved the way to the synthesis of better materials than hitherto available.

The deviations of properties of nanocrystalline materials with respect to the properties occurring in coarse-grained materials can be attributed primarily to two effects: The 'size effect' which arises when the characteristic size of the building blocks of the microstructure (e.g. the crystallite size), in any dimension, is reduced to a size corresponding to the critical length scale of a physical phenomena (e.g. the mean free paths of electrons or phonons, a coherency length, a screening length, etc.). The second effect is an 'interface effect': Due to the reduced dimensionality a significant volume of atoms resides at the grain boundaries (forming the intercrystalline regions) and/or at surfaces,

leading to a large volume fraction of interfacial/surface atoms. According to simple geometrical models, the grain boundary (GB) volume fraction is as much as 50% for a grain size of ~ 2.4 nm, assuming a grain boundary thickness value of 0.5 nm [18]. Thus, it can be expected that this interfacial volume fraction will have significant effect on the properties, which becomes more pronounced with decreasing grain sizes [17, 19].

Moreover, the grain-boundary structure in nanocrystalline materials differs from the grain-boundary structure of conventional coarse-grained materials by the increased presence of features such as triple and quadruple junctions which impart additional anomalies to the properties [20, 21]. It is apparent that the presence of such interfaces will have an effect on the interfacial energetic, which can then be engineered to tailor particular properties. Hence, grain boundary engineering has become a subject of research also for nano-crystalline materials [22-24].

In addition to these inherent features which are related intrinsically to the small crystallite size, the presence of defects such as dislocations, vacancies, second phase materials etc. make nanocrystalline materials all the more interesting. For e.g., the unusual mechanical behaviour of nanocrystalline materials [25] such as showing greatly enhanced ductility [18, 26], dramatically increased strength and hardness [27, 28] is thought to arise from the intricate interplay between dislocation and grain-boundary processes [29]. In particular, in recent years, many theoretical models have studied the evolution of defects and GB structures with the focus placed on specific features of physical mechanisms of plastic flow and diffusion in nanocrystalline materials. These models deal with factors such as: the nanoscale and interface effects on lattice-dislocation slip (serving as the basic deformation mechanism in conventional coarse-grained polycrystals), deformation mechanisms associated with the active role of GBs, the competition and interaction between various deformations mechanisms [30-33] etc.

A reduction in the crystallite size leads to an increase in the Gibbs free energy due to the Gibbs-Thomson effect [34-36]. As compared with conventional coarse-grained materials, the thermal stability of nanocrystalline materials is strongly affected by the large volume fraction of grain boundaries; their thermal properties cannot be adequately described by the basic thermodynamic functions. From a thermodynamic point of view, the structure of the nanograin boundaries has been found to influence the configurational and vibrational entropy as well as the enthalpy of the system [37-39]. Hence, the presence of a high density of interfaces has an associated energy penalty and thus nanocrystalline materials tend to be unstable with respect to thermally activated structural changes. This

intrinsic instability has stimulated a number of studies in recent years to find ways to stabilize these materials against coarsening. The inherent non-equilibrium state of the nanocrystalline system makes the control of the structural features a challenge and hence the study of the kinetics of grain growth process all the more essential.

The motivation for the study in this work has been directed towards these basic problems of the nanocrystalline materials. The work involves the fabrication of nanocrystalline materials accompanied by the study of the evolution of microstructural features associated with the lattice and the grain boundaries of, in particular, nanocrystalline pure metals. Further the thermal stability of these structures has been studied in-depth by investigating the kinetics of the grain growth process. In the framework of the thermal stability studies, the stabilization effect by the addition of an alloying element has also been investigated.

A brief overview of the materials investigated, the experimental methods employed, the analytical tools and the theoretical background of the studies performed have been outlined in the following sections. A short synopsis of the thesis describing the scope of the present work is also presented.

1.2 Nanocrystalline materials fabricated by mechanical attrition

Mechanical attrition is a top-down processing technique that enables the production of large quantities of nanocrystalline powders, which can be used as powders but can also be consolidated into bulk forms. It was first developed as a powder metallurgy method to produce dispersion-strengthened alloys with fine, uniform dispersoid distributions [40]. Subsequently, it has attracted considerable attention also as a powerful non-equilibrium processing method that allows the fabrication of a variety of metastable or far-from equilibrium microstructures [41]. It is often considered attractive due to its simplicity, the inexpensive nature of the required equipment, its applicability to a wide material class, and the ease with which the process can be scaled to produce large quantities of powder. Mechanical attrition characterizes a milling process of powders of uniform composition, such as pure metals, intermetallics or pre-alloyed powders, while mechanical alloying refers to milling processes involving mixtures of powders to produce a solid solution, intermetallic phases or amorphous materials.

Two types of mills have been employed in the present work: a planetary mill and a high-energy shaker mill. The working principle of a planetary ball mill which was

employed in the present studies is shown in Figure 1.1a. In a planetary ball mill, the milling vessel is arranged on a rotating support disk which rotates in the opposite direction of the vessel. The opposite movement of the vessel and the support disk lead to the exertion of a centrifugal force which cause the ball-powder-ball and ball-powder-wall collisions (Figure 1.1b). In a shaker mill, the milling vessel is mounted into a clamp (Figure 1.1c). The vessel is shaken in a complex motion which combines back and forth swings, with short lateral movements, where each end of the vessel is describing a figure-8.

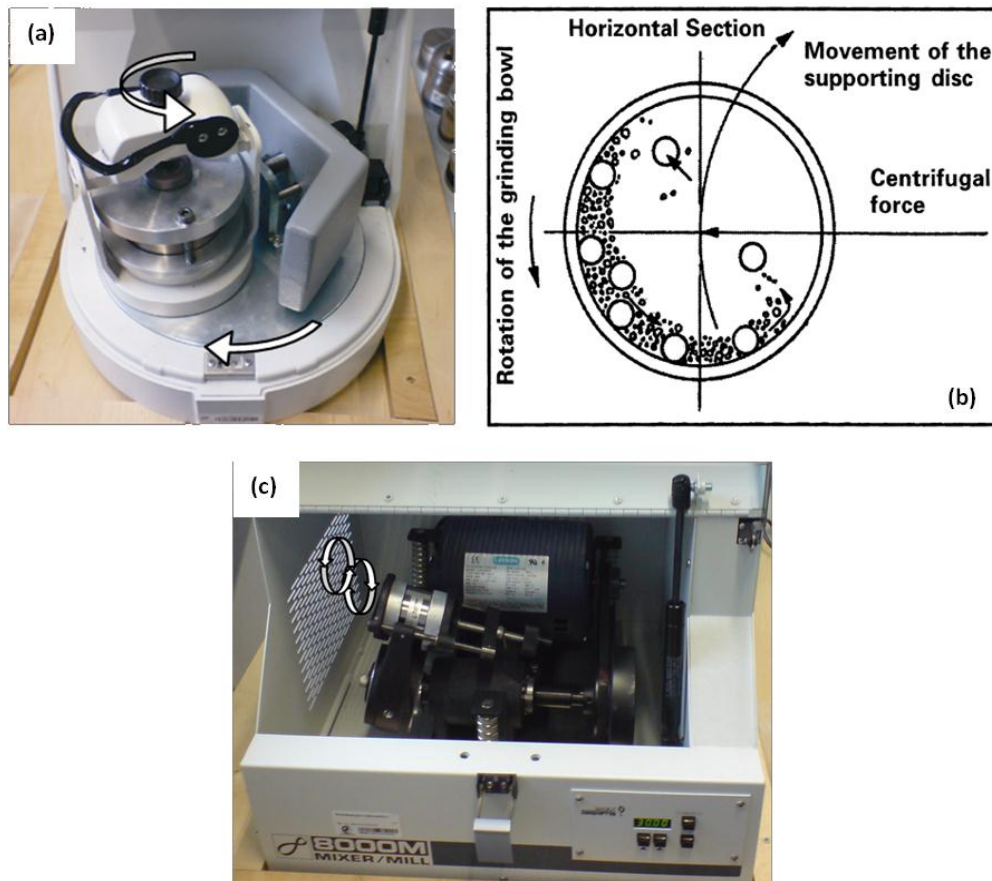


Figure 1.1: (a) Operating mode of a planetary ball mill; (b) Sketch of the ball motion inside the planetary ball mill; (c) Operating mode of a shaker mill.

In both mills, the transfer of mechanical energy to the powder particles results in introduction of strain into the powder through the generation of crystalline defects, such as dislocations, grain-boundaries, stacking faults, vacancies etc. leading to severe plastic deformation. Formation of nanocrystalline microstructures by mechanical attrition occurs in three stages [42]:

- Stage 1: Localization of deformation in shear bands containing a high density of dislocations

- Stage 2: Dislocation annihilation/recombination/rearrangement to form subgrains structures with nanoscale dimensions- prolonged milling extends this structure homogeneously throughout the sample.
- Stage 3: Reorientation of grains randomly leading to the disappearance of low-angle grain boundaries and formation of high-angle grain boundaries, presumably by grain boundary sliding/rotation or by 'discontinuous' dynamic recrystallisation.

Once an entirely nanocrystalline state is achieved, the subgrains reach a critical value of refinement attributed to a balance between the defect structure introduced by plastic deformation upon milling and its recovery by thermally activated processes. The minimum grain size achievable is dependent on several milling variables as well as the property of the materials being milled.

Similarly, mechanical alloying involves the synthesis of a variety of equilibrium and non-equilibrium alloy phases starting from blended elemental or pre-alloyed powders. The strain introduced upon milling, as a result of defects, has an effect on diffusion. Additionally, the refinement of particle and crystallite size leads to a reduction in the diffusion distances. These effects along with a local increase of temperature, upon impact, lead to alloying of the blended elemental powders on an atomic level during the milling process. The result could be constitutional changes leading to formation of nanocrystalline solid solutions (both equilibrium and supersaturated), intermetallic phases (equilibrium, metastable and quasicrystalline), and amorphous materials.

While a highly defective microstructure is fabricated upon milling, it is observed that highly defective non-equilibrium grain boundaries are also formed in mechanically synthesized nanocrystalline materials. These high-density ensembles of non-equilibrium grain-boundary defects exhibit the highest concentration in as-prepared nanocrystalline specimens and during some relaxation time interval after fabrication, these non-equilibrium dislocation structures at grain boundaries undergo transformations driven by a release of their elastic energy: Non-equilibrium dislocations move to new positions where they annihilate or form more ordered low-energy configurations. These effects are found to further enhance the diffusion properties of mechanically synthesized nanocrystalline materials also when compared with those of nanocrystalline materials fabricated by non-mechanical (more equilibrium than mechanical) methods and those of coarse-grained counterparts [43].

1.3 Size dependence of lattice parameter

One of the many controversial properties of nanocrystalline materials is the crystallite-size dependence of the lattice parameter of nanocrystalline material [44]. With decreasing crystallite size, the lattice parameters of nanocrystalline materials can, apparently, both contract [45-47]) and expand [48, 49]. Moreover, inconsistent experimental results have been presented: for example, both lattice contraction in Ni [50] and Pd [51], and lattice expansion in Ni [52-54] and Pd [55] have been reported. Several models/approaches have been proposed to understand the crystallite-size dependence of the lattice parameter(s). These consider the role of, for example, intracrystalline pressure [52, 56], interface stress [57], interfacial excess volume [58], grain-boundary enthalpy [59], excess grain-boundary volume [60] and the Madelung theory [61]. However, these explanations are of limited generality and none of them can explain all experimental findings.

Pure metals in the nanocrystalline state, fabricated by mechanical milling, have been investigated in the present work. The choice of the metals is based not only on their different crystal structures, but also on their contrasting properties: FCC Ni and Cu (lower melting point) and BCC Fe and W (paramagnetic; highest melting point) have been all subjected to ball milling under similar conditions. The microstructural evolution, in terms of crystallite size and microstrain, has been followed. In parallel, a precise determination of the lattice parameter has been carried out by taking particular care of different factors affecting its determination.

1.4 Grain growth studies

As a consequence of their extremely fine structural length scales and large volume fraction of grain boundaries, nanocrystalline materials reside in a non-equilibrium state. This energetically unfavourable condition leads to rapid grain growth in pure nanocrystalline materials at relatively low homologous temperatures, T/T_m , where T_m is the melting temperature of the material). It is evident that the nature of grain boundary and microstructure as well as the evolution of the grain boundary structure (grain boundary relaxation) plays a dominant role in determining the kinetics of grain-growth, and the growth kinetics is as such different from that in coarse grained metals.

Grain growth in conventional materials can generally be described by the equation $D_t^n - D_0^n = k_0 \exp\left(-\frac{Q}{RT}\right)t$, where D is the grain size after annealing a sample at

temperature T for time t , D_0 is the initial grain size, n is the grain-growth exponent, k_0 is a pre-exponential constant, Q is the activation energy for grain growth, and R is the gas constant [62]. Both Q and n are important parameters in describing the kinetics and mechanism of grain growth. Ideally, n is expected to be 2, suggesting a parabolic relationship for grain growth; but the observed values in nanocrystalline materials have been found to take values between 2 and 10 [63]. Studies have indicated that the value of n decreases toward 2 upon annealing at relatively high homologous temperatures. Further, the other parameter, i.e. the activation energy for grain growth process in nanocrystalline materials corresponds to the activation energy for either lattice (Q_l) or grain boundary (Q_{gb}) diffusion in coarse-grained materials. While in most of the studies the activation energy for grain growth in nanocrystalline materials compares more favourably with Q_{gb} than with Q_l , a few exceptions have been reported. It has also been reported that the activation energy for grain growth at higher temperatures compares favourably with Q_l , while at lower temperatures, it compares favourably with Q_{gb} , suggesting a change in mechanism with temperature [64]. However, contrary to expectations, grain growth in nanocrystalline materials can also be restricted at relatively high homologous temperatures. This suppression of grain growth has been attributed to factors such as a narrow grain size distribution, equiaxed grain morphology, low-energy grain boundary structures, relatively flat grain boundary configurations, and porosity of the consolidated samples ([65, 66] and references therein). Different studies thus report a wide spectrum of observations on nanograin growth. Moreover, the fabrication technique employed introduces structures that are unique to the method and hence the nanocrystalline materials prepared by various methods may behave differently.

In general, isothermal annealing experiments report a linear growth that later changes to normal parabolic grain growth [67-69], the crossover being dependent either on the annealing temperatures or on a particular critical grain size. The grain growth kinetics have been investigated for over two decades and several theoretical models have been proposed based on experimental studies [67, 70] and simulations [71-73]. Mechanisms such as grain rotations [74], triple-quadruple junction drags [75, 76], vacancy generation [77], excess free volume at the grain boundaries [78], abnormal grain growth [79] have been invoked to explain particular experimental result. However, a full understanding of the grain growth kinetics of nanocrystalline materials is still incomplete.

Stemming from the motivation to determine the thermal stability of the nanocrystalline metal fabricated in this work, grain growth kinetics studies have been

carried out on two pure nickel metal specimens with different initial microstructures. The thermal behaviour of the metal has been traced by both temperature varying as well as isothermal annealing while making *in-situ* studies on the microstructural evolution by means of X-ray diffraction measurements.

1.5 Grain growth stabilisation

From a technological point of view, concerning nanocrystalline powders, e.g. produced through mechanical milling as in this work, the thermal stability is important for consolidation of these powder particles into bulk form without coarsening the microstructure, therewith maintaining the exceptional properties of the nanocrystalline state. Significant stabilization can be attained in these materials by the incorporation of a chemically different component, i.e., by alloying or also by impurities [80, 81].

The suppression of grain growth by such a method has been rationalized by considering both kinetic and thermodynamic mechanisms. Kinetic descriptions involve classical mechanisms in which solute atoms or precipitates impose drag forces on the interface motion [82-84], whereas thermodynamic descriptions are unique to the nanocrystalline state and are based on substantial changes in grain boundary energy due to alloying [85-87], by reducing the overall energy penalty of the large volume fraction of intercrystalline regions by grain-boundary segregation.

The stabilization mechanism relevant upon alloying Ni with W has been investigated in this work. Nickel-tungsten alloys with a high W content have found extensive applications due to their high density and strength [88]. Further, Ni-W coatings are nominated as a promising environmental friendly alloys to replace hard chromium coatings, due to the satisfactory appearance of coatings, and good mechanical and anti-corrosion properties [89, 90]. Figure 1.2 shows the phase diagram of Ni-W [91]. The equilibrium solubility of W in Ni at room temperature is about 12 at. % rising to 17.5 at. % at 1495 °C, whereas the solubility of Ni in W is negligible (approx. 0.3 at. % at 1495 °C). Additionally, the intermetallic phases Ni_4W , NiW and NiW_2 can occur.

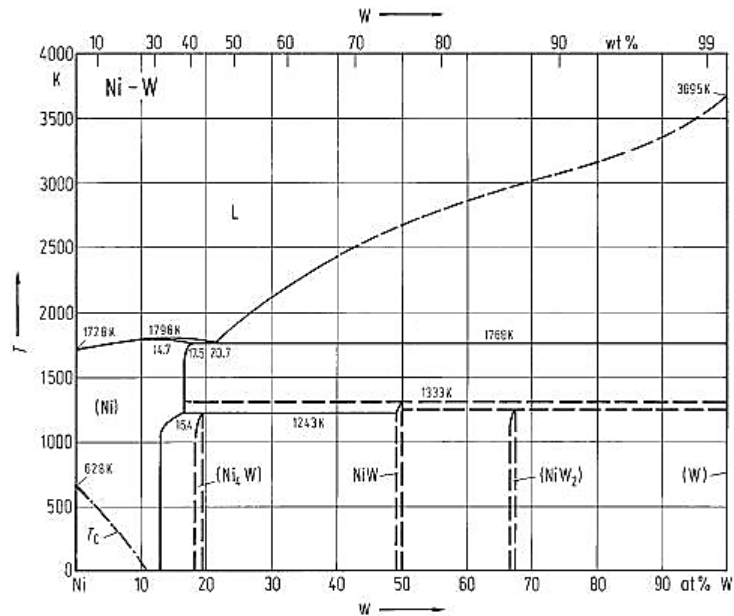


Figure 1.2: Phase diagram of Ni-W [91].

A Ni-W solid solution fabricated by mechanical alloying the elemental powder mixture (with a nominal composition of 15 at. % W) has been studied in this work. The structural evolution as well as the solid-solution formation has been followed as a function of milling time. Further the thermal stability of the alloy formed has been investigated by X-ray diffraction measurements *in-situ* during annealing.

1.6 Main methodology of characterization

X-ray diffraction proves to be a very appropriate tool for investigation of the microstructure of nanocrystalline materials due to its versatility in nondestructively obtaining microstructural information averaged over a moderately large volume ($\sim 1 \text{ mm}^3$), thus providing statistically relevant information, as compared to methods such as transmission electron microscopy (TEM). In particular, from line-profile analysis, i.e. from the analysis of the (possibly asymmetric) broadening and the (shift of the) position of diffraction lines, a wealth of information can be obtained about the imperfect crystalline structure in terms of effective crystallite (domain) size, microstrain and macrostrain, from which parameters as the crystallite size (distribution), stacking fault probability, mechanical stresses, the dislocation density, concentration variations, etc. can be derived [92, 93].

In this work extensive X-ray diffraction line profile analysis has been employed to extract the microstructural information. A brief description of the methods employed is provided in the following sections.

A measured diffraction-line profile consists of instrumental effects, such as wavelength dispersion and non-ideal optics, which are convoluted with the line broadening induced by microstructural effects ('structural line broadening') and hence the instrumental contribution to the profile has to be characterized and corrected for prior to the extraction of microstructural parameters.

Usually, structural line broadening is subdivided into crystallite-size broadening and microstrain broadening. A variety of approaches exist for the evaluation of the size and strain parameters from the broadened line profiles [94]. The microstructural information can be extracted from the profile parameters either from single or multiple diffraction lines using more or less realistic, general assumptions on the material imperfection/line shape and such methods generally are called 'line-profile decomposition' methods. On the other hand, microstructural parameters can be determined by fitting line profiles, calculated on the basis of a model for the microstructure specific for the material investigated to measured profiles, called as 'line-profile synthesis' methods (i.e. no specific, a-priori line-shape assumptions are employed) [95]. A brief description of the methods employed in this work is provided below with more specific details in the following chapters of the thesis.

1.6.1 Line-profile decomposition methods

1.6.1.1 Single-line method [96].

A diffraction line is conceived as a convolution of a Gaussian and a Lorentzian (also called Cauchy) profile (i.e. as a Voigt function), where the Gaussian component is due to microstrain and the Lorentzian component is due to finite crystallite size. The measured profile h is a convolution of the specimen profile f and the instrumental profile g . If it is assumed that the instrumental profile g and the measured profile h can also be represented by Voigt functions, a simple correction for instrumental diffraction line broadening on the basis of the integral breadths and Voigt parameters of the measured and instrumentally broadened line profiles is possible as well by subtracting the instrumental Lorentzian and Gaussian integral breadths of the instrumental profile from the Lorentzian and Gaussian integral breadths of the measured profile linearly and quadratically, respectively [96].

The integral breadths β_C^f and β_G^f of the Lorentzian (Cauchy) and Gaussian components, respectively, can be related to the volume-weighted column length L and the microstrain ε as:

$$\beta_C^f = \frac{\lambda}{L \cos \theta} \quad (1.1)$$

$$\beta_G^f = 4 \varepsilon \tan \theta \quad (1.2)$$

where λ is the wavelength and θ is the Bragg angle.

1.6.1.2 Williamson-Hall (WH) method [97].

Assuming that the size- and strain-profile components are Lorentzian profiles, the corresponding integral breadths given by Eqs. (1.1) and (1.2) are linearly additive to obtain the total integral breadth in reciprocal space $\beta^* = \beta \cos \theta / \lambda$ with $d^* = 2 \sin \theta / \lambda$:

$$(\beta^f)^* = \frac{1}{L} + 2 \varepsilon d^*. \quad (1.3)$$

Hence a plot of $(\beta^f)^*$ vs d^* should result in a straight line and then the values for grain size and strain can be obtained from the intercept and the slope in a straight line, respectively. Hence, size-strain separation is achieved under the assumption that size broadening does not depend on the length of the diffraction vector whereas strain broadening does. Other variants of the WH method exist [e.g. adopting Gaussian shaped functions, taking into account anisotropic line broadening as due to dislocations etc.], but all are based on the assumption of specific profile shapes [98, 99].

1.6.1.3 Warren-Averbach (W-A) method [93, 100, 101]

The W-A method is a Fourier method which does not assume a specific profile shape for size and strain broadening. The convolution of the size-broadened and strain-broadened profiles in real space corresponds to the product of their Fourier coefficients in reciprocal space. Usually, only the cosine Fourier coefficients are considered. The sine coefficients are non-zero only in the case of asymmetric diffraction profiles and are usually not physically interpreted. Hence the cosine Fourier coefficients of the structurally broadened profile $A(L, S_i)$ are given by

$$A(L, S_i) = A^S(L)A^d(L, S_i) \quad (1.4)$$

where $A^S(L)$ denotes the order-independent, cosine Fourier coefficient and $A^d(L, S_i)$ is the order-dependent cosine Fourier coefficient and L is a correlation distance in the crystals perpendicular to the diffracting planes. The superscripts S and D signify the frequently adopted interpretation in terms of size- and distortion-related broadening effects. If more than one order of reflection is available and the dependence of $A^d(L, S_i)$ on the order of the reflection is specified, separate information on $A^S(L)$ and $A^d(L, S_i)$ can be extracted.

Assuming either small strains or approximately Gaussian strain distributions, $p(\varepsilon_L)$, for all values of L , separation of size and strain can be realized using the equation

$$\ln A(L, S_i) = \ln A^S(L) + \ln A^d(L, S_i) \cong \ln A^S(L) - 2\pi^2 L^2 S_i^2 \langle \varepsilon^2(L) \rangle \quad (1.5)$$

where $\langle \varepsilon^2(L) \rangle$ is the mean-squared strain for the correlation distance L . From the straight line obtained in a plot (at fixed L) of $A^d(L, S_i)$ versus S_i^2 for several (at least two) reflections, $A^S(L)$ and $\langle \varepsilon^2(L) \rangle$ are obtained. The area-weighted column length can be determined from the size coefficients [99, 102].

1.6.2 Line profile synthesis method : Whole powder pattern modeling [103]

A line-profile synthesis method that has gained momentum in the last 10 years is the Whole Powder Pattern Modelling (WPPM) approach. This method involves the use of physical models of the microstructure (e.g., involving crystallites size/shape and lattice defect type, density and distribution) to describe the line profile. Profile modelling then is intended as a procedure to reproduce the observed line profiles by adapting (optimizing) some physical parameters (e.g., mean domain size, shape parameters, density of defects, etc.). Therefore, results can directly be interpreted in terms of these physical parameters, instead of using generic profile parameters like Gaussian or Lorentzian fraction and breadth, typical of profile fitting.

The observed diffraction line profile, a convolution of the line profiles produced by all contributing effects, is given as

$$I(s) = I^{IP}(s) \otimes I^S(s) \otimes I^D(s) \otimes I^F(s) \otimes I^{APB}(s) \otimes I^C(s) \otimes I^{GRS}(s) \dots \quad (1.6)$$

where s is the reciprocal space variable ($= 2 \sin \theta/\lambda$), IP is the instrumental profile, S the coherent scattering domain size, D the lattice distortions (e.g. due to dislocations), F for faulting (twin and deformation faults), APB the anti-phase boundaries, C for composition fluctuations, GRS for grain surface relaxation. As such several contributions can be incorporated by adding the corresponding profile function in the above equation. The above convolutions can be simplified simply as the product of the Fourier Transforms of the terms and can be therefore written as:

$$I(s) = \int_{-\infty}^{\infty} \left[A_{hkl}^{IP}(L) * A_{hkl}^S(L) * A_{hkl}^D(L) * \left(A_{hkl}^F(L) * iB_{hkl}^F(L) \right) * A_{hkl}^{APB}(L) \dots \right] e^{-2\pi i L s} dL$$

where L is the Fourier length and A_i are the Fourier transforms of the individual profile functions proposed from eq. 1.6.

1.6.3 Comparison of the different methods of line-profile analysis

The challenge of line-profile analysis is the unravelling of the various contributions to the observed, broadened diffraction lines and the interpretation of these unravelled

contributions in terms of parameters that are commonly used in materials science, as dislocation densities, faulting probabilities and crystallite size. Line-profile synthesis methods, as the Whole Powder-Pattern Modelling approach can provide a direct relation between such microstructural parameters and diffraction-line broadening. Moreover, a direct calculation of the diffraction-line shape has the advantage that no a priori assumptions on the line-profile shape are required. However, in many practical situations the very large expenditure of time and effort, as required for whole powder-pattern modelling, e.g. in case of the analysis of in-situ, non-ambient measurements where high quality data are unattainable, is extravagant or even impossible. Then, a simple analysis of integral breadths may be appropriate for obtaining semi-quantitative estimates of crystallite size and microstrain. Thus, different methods of line-profile analysis have been employed in this work, where the selection of a particular method has been based on the type (and quality) of the available diffraction data and the desired level (detail and quantitative nature) of microstructural information.

A summary of underlying assumptions and size and strain parameters for the different methods of line-profile analysis used in this work are reported in Table 1.1.

Table 1.1: Summary of the line-profile analysis methods employed in this work [95].

Method	Assumptions	Size	Strain
Williamson-Hall	Lorentzian shaped peaks	Volume weighted column length	Maximum strain related to local mean squared strain for Gaussian strain distributions.
Single line analysis	Voigt shaped peak profiles	Volume weighted column length	Maximum strain related to local mean squared strain for Gaussian strain distributions.
Warren-Averbach	Gaussian strain distribution or small strains	Area weighted column length	Mean squared strain related to $A^d(L)$
Whole powder pattern modeling	No assumption regarding profile function. Refinement of microstructural parameters by direct modelling of the experimental pattern	Grain diameter (based on assumption of a grain shape and a size distribution)	Dislocation density

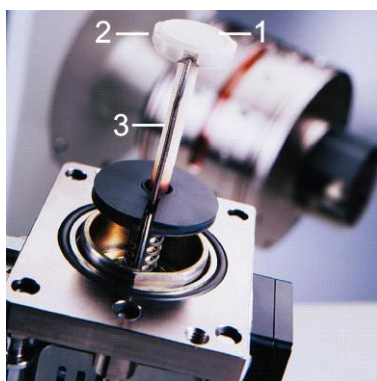
1.6.4 X-ray diffraction instrumentation

The materials under study have been characterized using a Bruker AXS D8 Advance θ - θ diffractometer operating in Bragg-Brentano geometry using Cu-K α radiation. The diffractometer is equipped with a Cu X-ray tube and a Ni absorption edge filter (to remove

Cu- $K\beta$ radiation) positioned in front of the 1D position-sensitive VANTEC-1 detector (Bruker AXS). The X-ray tube is operated at a tube voltage of 40 kV and a tube current of 40 mA. Heating experiments were conducted under N_2 - H_2 atmosphere (98 % N_2 - 2 % H_2) with a gas flow of 0.7 l/min, in an Anton Paar HTK 1200N oven chamber.

A thick specimen for X-ray diffraction measurements was prepared by filling a sufficient amount of powder (~ 1 g) in the sample carrier (Figure 1.3). The powder was slightly compacted and the surface was flattened. The setup ensures that the specimen surface is exactly positioned in the center of the goniometer.

Additional diffraction measurements were carried out using a Panalytical (formerly Philips) MRD Pro diffractometer operating in parallel-beam geometry, which was equipped with an X-ray lens in the incident beam and a parallel-plate collimator, a flat graphite monochromator and a proportional counter in the diffracted beam.



1. Sample carrier (Al_2O_3)
2. Fixing ring
3. Thermocouple

Figure 1.3: Sample holder for XRD measurements in the oven chamber.

The measurements with a parallel beam geometry were carried out in order to determine precisely the lattice parameter: Measurements employing parallel-beam geometry enable a more precise lattice-parameter determination since aberrations due to specimen roughness, transparency and displacement that would occur in a powder diffractometer based on a (para-) focusing geometry (e.g. Bragg-Brentano geometry) are less critical in the parallel beam set-up.

1.7 Outline of the thesis

The thesis has been divided into three sections, each of which reports investigations of nanocrystalline materials fabricated by means of mechanical milling. The microstructural studies of these materials form the background of the entire work. Apart from X-ray

diffraction, transmission electron microscopy, scanning electron microscopy as well as differential scanning calorimetry investigations were used.

The second chapter deals with the crystallite size dependence of the lattice parameter of pure metals (Ni, Fe, Cu and W) fabricated by ball milling. It was observed that the lattice parameter exhibits an anomalous variation with decreasing crystallite size, i.e., a lattice contraction followed by lattice expansion takes place upon decreasing the crystallite size for all the materials investigated. Based on two competing mechanisms, a lattice contraction due to the Gibbs-Thomson effect and a lattice expansion resulting from the presence of an increasing amount of excess free volume in the grain boundaries of the heavily deformed nanocrystalline powders, the non-monotonic variation of the lattice parameter has been rationalized.

The third chapter reports investigations on the thermal stability of the nanocrystalline microstructure of pure ball-milled nickel powder samples. The microstructural evolution has been investigated by both temperature varying as well as isothermal annealing. Detailed investigations have been carried out using in particular different X-ray diffraction line-profile analysis methods. Two different samples of nickel with different initial microstructures have been analyzed. Peculiarly, a higher stability of the finer-grained microstructure has been observed. These findings have been discussed on the basis of several factors that could contribute to the peculiar grain-growth behaviour observed.

The last chapter describes the study of the thermal stability of nanocrystalline Ni alloyed with W: The microstructural evolution of ball-milled nickel - tungsten (with ~15at.-%W) upon milling and upon annealing has been investigated. Ball milling of elemental Ni and W powder results in the formation of a Ni(W) solid solution. A considerable improvement in the thermal stability of the nanocrystalline microstructure of the Ni(W) solid solution as compared to pure Ni was observed: A nanocrystalline microstructure was retained even up to an annealing temperature of 700 °C. The increased thermal stability of the alloy system as compared to pure Ni in the nanocrystalline state has been discussed.

Chapter 2

Non-monotonic lattice parameter variation with crystallite size in nanocrystalline ball milled powders.

G. K. Rane, U. Welzel, E. J. Mittemeijer

Abstract

An anomalous dependence of the lattice parameter on the crystallite size of nanocrystalline ball-milled powders of metals was observed: *lattice contraction* followed by *lattice expansion* with decreasing crystallite size. These data were determined by application of detailed X-ray diffraction measurements. To this end, the lattice parameters of all the metals were accurately determined by correcting for influences of stacking faults in FCC metals as well as by correcting for instrument-related aberrations. The non-monotonic variation of the lattice constant was proposed to be a result of two competing mechanisms: interface-stress induced contraction versus expansion as a result of the stress field generated at the crystallite boundary due to the increased excess free volume in the crystallite boundary upon decreasing crystallite size.

2.1 Introduction

Studies on the class of bulk solids with a nanocrystalline microstructure, over more than a decade now, have only partially revealed the underlying mechanisms which lead to the anomalously altered or completely unique properties they exhibit (as, for example, extreme ductility without strain hardening, higher strength and hardness, larger linear coefficient of thermal expansion as compared to coarse-grained materials etc.) [19, 25, 104-108]. These distinct properties are governed by the small grain size implying an increased surface (interface) to volume ratio and an inherent defect structure: the grain boundary volume fraction is almost 50 % at a grain size of about 2.5 nm [109].

Several studies indicate that an excess, free volume contained in the grain boundaries of nanocrystalline materials is of central importance for the properties of nanocrystalline materials ([110-112] and references therein). Accordingly, with a large volume fraction of grain boundary, nanocrystalline materials are considered to be inherently heterogeneous - formed of ordered crystallites embedded in a highly disordered grain boundary matrix (with a different atomic distance distribution) [113-115]. Although this paradigm concerning the inherent structure of nanocrystalline materials is still controversial, in any case the paramount role of grain boundaries in nanocrystalline materials cannot be ignored ([6] and references therein).

One such anomalous effect related to the atomistic structure of nanocrystalline materials is the lattice distortion. Investigations on the crystallite-size dependence of the crystal-lattice parameter(s) of nanocrystalline material have shown ambiguous results indicating both contraction and expansion of the lattice with decreasing grain size (see Table 2.1). Processing/fabricating techniques might also play a role in the uniqueness of a microstructure (since nanocrystalline materials are often synthesized under highly non-equilibrium conditions). Lattice expansion has been predominantly observed in all materials processed by 'non-equilibrium' (severe plastic deformation SPD) processing while lattice contraction was observed predominantly for either consolidated or equilibrated structures. To understand these phenomena, several models/approaches have been proposed, involving, for example, the effect of intracrystalline pressure [52], interface stress [116], grain-boundary enthalpy [59], excess grain-boundary volume [60, 117] and a supersaturation of vacancies [118].

Also, for the same system, for instance in Pd (Table 2.1), disparate behaviour is observed in different investigations – at smaller grain sizes < 8 nm, lattice expansion was

observed [114] while for grain sizes > 8 nm, lattice contraction occurs [119]. This hints at the importance of the grain-size regime for the occurrence of expansion or contraction.

Table 2.1: Literature reports of lattice-parameter change with decreasing grain size.

Sample	Grain size (nm)	Processing method	Lattice parameter variation
Nb [120] Fe [112] Si [121] Ge [122]	40 – 10 60 – 15 20 – 8 40 - 4	Ball milling	Expansion
Pd [114]	7.5 – 5.5 5 – 2	Thin film by PVD	
Cr [123]	79 – 11	Inert gas condensation (IGC)	
Ge [49]	75 - 20	Sputter deposited film – annealed at higher temperature to obtain different grain sizes	
Ni [118]	15 – 6	Thin film by JG-PF high frequency ion beam sputtering	
Pd [124] Pd [119] Fe [125]	8 100 – 10 50 - 7	IGC followed by consolidation IGC followed by pre-annealing to equilibrate the GB	Contraction
Cu [126]	95	(SPD) Torsion straining with axial rotation under pressure	
V [51]	> 60	Ball milling	
Cu [127] Pd [127]	100 – 10 50 - 10	Magnetron sputtering followed by loop annealing to obtain higher grain size.	
Cu, Au, Sn, Bi ([128] and references therein)		Nanoparticles (particles of nano size)	

In particular, a previous study of our group [129] on nanocrystalline Ni prepared by ball milling and by magnetron sputtering techniques indicated a non-monotonic variation of the lattice parameter with grain size exhibiting contraction down to a particular critical grain size followed by a change to lattice expansion for smaller grain sizes. In order to confirm and evaluate the observed effect, in the present work the dependence of the lattice parameter on crystallite size has been investigated for nanocrystalline Fe, W and Cu produced by ball milling on the basis of a very precise X-ray diffraction analyses. Peak shifts due to instrumental aberrations and due to stacking faults in FCC Cu and Ni have been accounted for. For all the metals, a non-monotonic dependence of the lattice parameter on crystallite size has been established (see Section 2.4.2). The possible background for this phenomenon is presented in Section 2.2.

2.2 Theoretical background

2.2.1 Lattice contraction

The concept of surface/interface stress ('Gibbs-Thomson effect') [130] implies the occurrence of a hydrostatic compression induced by interface/ surface stress leading to lattice contraction given by [131]

$$\Delta a_1 = -\frac{4}{3K} \frac{\sigma_s a_0}{D} \quad (2.1)$$

where σ_s is the interface tension, D is the spherical grain diameter, K is the bulk modulus and a_0 is the lattice parameter of the undistorted coarse grained material. Eq. 2.1 is hereafter called 'interface effect'.

With decreasing grain size, the effect of interface stress will become significant and a **lattice contraction** is observed.

This view originally concerned the effect of surface tension on isolated particles of smaller dimension. It should be noted that the 'surfaces' in the nanocrystalline material considered here are the interfaces/ grain boundaries (of the nanocrystalline *grains* in a bulk system). In the last case, a lesser hydrostatic pressure may operate than in the case of free surfaces of similar sized *particles*, since the interfacial energy (or grain-boundary energy) is much smaller than the free-surface energy.

2.2.2 Lattice expansion

Properties of nanocrystalline materials are largely influenced by its fabrication technique which frequently is neglected in understanding the anomalous effects they exhibit [124, 132, 133] (as could also be suggested from the results in Table 2.1). An example is the production of nanocrystalline materials by the method of severe plastic deformation (SPD) by ball milling which leads to the formation of highly non-equilibrium defected structures (along with a high density of vacancy defects - close to the amount of thermal vacancies at melting [134]) as opposed to other fabrication techniques. We now consider the effects of the microstructure of such SPD processed nanocrystalline materials.

Characteristically, the high density of defects generated in such processes have been classified into *statistically stored* (formed at early stages of conventional plastic deformation processes) and *geometrically necessary* dislocations (associated with the existence of grain boundaries, which are typically introduced by strong strain gradients, and are likely to be the largest fraction at grain boundaries at the nanograin level – its high density also leading

to the formation of excess dislocation boundaries). These ‘excess’ grain-boundary dislocations are commonly distributed chaotically along a grain boundary. Also, presumably, dislocations being in an unstable configuration in the grain interiors, they are repelled to the grain boundaries leaving the bulk of the nanograins relatively defect free and a disordered grain boundary structure. Likewise, partial relaxation/recovery of the internal defected structure could also occur. It is proposed that climb and glide of excess dislocations are characteristic processes of relaxation (or annihilation- at the grain boundaries) of dislocations in nanocrystalline materials. A negative climb of edge dislocations is accompanied by vacancy emission - contributing to the excess vacancies observed in nanocrystalline materials [135, 136]. Generally, grain boundaries can act as vacancy sources (or sinks) [137, 138]; accumulation of vacancies would lead to the formation of voids at the grain boundaries [139].

Several experimental studies indicated the presence of vacancies in excess and vacancy clusters/voids (nanopores) [140-142] and a highly disordered structure at grain boundaries [113, 143] of nanocrystalline materials. These defects, considered as structural elements of nanocrystalline materials, together with the geometrical constraints to the grain-boundary structure, give rise to the notion of *excess free volume* (ΔV) [111, 144] at the grain boundaries. It can be expected that the excess free volume would lead to stresses in such a system causing distortion of the local lattice structure based on the effect of the displacement fields they generate [145-147]. A vacancy generates a radial displacement field which leads to long range inward relaxation of the neighbouring atoms towards the vacancy [41]. Thus, the presence of excess vacancies inside the grains and at the grain boundaries would lead to a radial hydrostatic pressure which causes short range disturbances that diminish as a function of $1/r^2$ where r is the distance from the defect [148].

Such a model, which considers the effect of vacancies (neglecting effects from dislocation interaction with each other as well as with vacancies) contributing to the excess volume at the grain boundaries and the stress field generated by these vacancies, was developed by Qin et. al. [44] to quantify the lattice distortion (expansion) of nanostructured materials. This simplistic model has been applied to our data to explain **lattice expansion** with decreasing crystallite size.

According to this model, defining the excess volume at the grain boundaries as ΔV , the deviation of atoms in the grains from their ideal position can be calculated. Then assuming a grain boundary thickness ξ , the lattice parameter change relative to the coarse grained lattice parameter a_0 is given as [44]:

$$\Delta a_2 = \frac{a_0}{2(D-a_0)} \left[\frac{\xi(\xi+2a_0)}{(\xi+a_0)} - \frac{\xi^2(\xi+2a_0)^2}{(\xi+a_0)(2D+\xi)(2D+\xi-2a_0)} \right] (\sqrt[3]{1+\Delta V} - 1) \quad (2.2)$$

where $\Delta V = (V_{gb} - V_{cr})/V_{cr}$ where V_{gb} is the volume of the grain boundary and V_{cr} is the volume to be occupied by the atoms in the grain boundary if they would be arranged as the atoms inside the crystalline grains.

The excess free volume in grain boundaries of ball milled metals has been assessed by positron annihilation studies and, in that case, appears to be proportional to the reciprocal grain size [149]. To assess the excess free volume, simple geometric models may be proposed implying that a fraction of the grain boundary width, ξ , may be conceived as representing the excess free volume in the grain boundary. One such model has been proposed in ref. [149] and it has been proposed $\Delta V = ((D + \xi/2)^2 - D^2)/D^2$ where D is the size of the grain taken as a sphere of diameter D (note ξ is not comprised in D).

Combining Δa_1 (eq. 2.1) due to interface stress and Δa_2 (eq. 2.2) due to excess free volume at the grain boundary would give the total lattice parameter change Δa with decreasing crystallite size D as

$$\Delta a = \Delta a_1 + \Delta a_2 = \frac{a_0}{2(D-a_0)} \left[\frac{\xi(\xi+2a_0)}{(\xi+a_0)} - \frac{\xi^2(\xi+2a_0)^2}{(\xi+a_0)(2D+\xi)(2D+\xi-2a_0)} \right] (\sqrt[3]{1+\Delta V} - 1) - \frac{4}{3K} \frac{\sigma_s a_0}{D} \quad (2.3)$$

Equation 2.3 thus gives the total lattice distortion considering the effect of both, interface stress induced lattice contraction and excess volume induced lattice expansion with decreasing grain size.

In the present work, a grain boundary width $\xi = 1$ nm is taken which is typical for ball milled specimens [26].

2.3 Experimental procedures and data evaluation

2.3.1 Specimen preparation and processing

Ball milling of Ni, Fe and Cu powders was carried out in a planetary mill (Fritsch Pulverisette P6, operated at 150 rpm with a ball to powder weight ratio of 10:1). W powder was milled in a high energy shaker mill (SPEX 8000M, ball to powder weight ratio of 4:1). Ni (99.8 wt. %, ≤ 300 mesh) was milled in a vessel made of Ni with Ni milling balls, Fe (99.9 wt. %, ≤ 10 microns) and Cu (99.9 wt. %, -100+325 mesh) was milled with balls and vessel made of steel and W (99.95 Wt. %, ≤ 200 mesh) with WC milling balls and vessel for avoiding contamination by abrasion of the milling vessel and the milling balls. To avoid oxidation of the elemental powders in as far as possible during the milling process,

handling of the powders and filling and sealing of the milling vessels was carried out in an argon box.

The as-received powders were encapsulated in evacuated quartz tubes and heated to 900 °C in a furnace for the preparation of coarse-grained reference samples containing no significant concentrations of crystal imperfections. These powders were used for determining the reference lattice parameter.

All powder specimens were analyzed for metallic impurities by inductively-coupled optical emission spectroscopy and for oxygen and nitrogen impurities by carrier gas hot extraction. For the specimen milled for the longest duration for each element, oxygen contamination was found to be about 0.5 at. % and nitrogen contamination was found to be less than 0.01 at. %. The X-ray diffraction patterns of all the powder specimens did not show any presence of impurity phases.

2.3.2 Microstructure investigation

High Resolution Transmission electron microscopy (HRTEM) studies were performed on Ni powder on a TEM JEOL 4000 FX operating at 400 kV. The pictures were made with a 2k × 2k CCD camera from Gatan (type orius 200 SC). Specimens of the Ni powder milled for the longest duration (i.e. 80 h) were prepared using a FIB Nova Nanolab 600 by the lift-out technique [150] applied to individual powder particles. The procedure is as follows: a protective Pt layer was deposited all around on the surface of a selected powder particle to prevent Ga⁺ damage in the region of interest during the following cutting and thinning process. Subsequently, applying a focusing Ga⁺ ion beam operating at 30 keV, a thin slice of the Ni powder particle was cut and ion-beam cleaned. This slice of the powder particle was picked up thereafter using a micro-manipulator and then welded onto a Cu grid for TEM examination. Finally, this sample was thinned to electron transparency using low Ga⁺ ion currents of 10–30 pA.

2.3.3 X-ray diffraction measurements and line profile analysis

X-ray diffraction (XRD) line-broadening measurements for microstructural investigations were made with Cu-K α radiation employing a Bruker D8 Advance θ - θ diffractometer operating in Bragg-Brentano geometry equipped with a Ni K α absorption edge filter in front of a 1D position-sensitive VANTEC-1 detector. Fe samples were measured using Co-K α radiation (to avoid a high fluorescence background which would occur using Cu-K α radiation) employing a Panalytical (formerly Phillips) X'Pert θ - θ diffractometer operating in

Bragg-Brentano geometry equipped with a diffracted-beam monochromator and a proportional counter. The measured diffraction patterns were analyzed using the Philips Profile Fit V1.0c software [151] by fitting a pseudo-Voigt function with the α_2/α_1 ratio set to 0.5 for the determination of the diffraction-line positions, the intensities, the full widths at half maximum and the peak-shape parameters. The instrumental broadening was characterized by measuring a LaB₆ powder specimen (NIST Standard Reference Material 660a).

In order to avoid contribution to peak shifts due to aberrations related to the diffractometer and specimen, lattice-parameter measurements were made with a Philips (now: Panalytical) MRD pro diffractometer with Cu K α radiation, operating in parallel-beam geometry equipped with an X-ray lens in the incident beam, a parallel-plate collimator in the diffracted beam and a proportional counter. A Panalytical MRD pro diffractometer, operating in the parallel-beam geometry, equipped with an X-ray lens in the incident beam, a parallel-plate collimator in the diffracted beam and a proportional counter was used for measuring the Fe powders employing Co K α radiation. The parallel-beam geometry avoids peak-position aberrations related to specimen roughness, transparency and displacement that would occur in a powder diffractometer based on focusing geometry (e.g. Bragg-Brentano geometry). [152, 153]. The specimens for the measurement were prepared by spreading the powder on a double sided tape on a glass slide.

For a precise determination of changes of the lattice constant, the lattice-(diffraction-) strain measurements should have a precision of the order 10^{-5} . The measurement of peak shifts ($\Delta 2\theta$) with the required precision poses no problems when the diffractometer is well aligned (note that alignment errors are less critical in the parallel beam set-up used in this work, as compared to a focusing, e.g. Bragg-Brentano geometry), sufficiently long counting times are used and the measurement temperature is controlled to within about one Kelvin and the temperature of the cooling water of the X-ray source is controlled to within a few Kelvin. These conditions were well fulfilled for the measurements performed in this work. The offset of the diffraction angle scale was corrected on the basis of measurement of the peak positions of a LaB₆ (NIST SRM660a) standard powder sample.

The crystallite sizes and microstrain evolution upon continued ball milling were traced by employing the single-line broadening analysis applied to all the reflections measurable in the 2θ range $20^\circ - 140^\circ$ for all the samples. The results were averaged over all the measurable reflections. Assuming that the Cauchy component of the structurally

broadened profile is due to the small crystallite size and that the Gaussian component of the structurally broadened profile, f , is due to microstrain, the crystallite size, D , and the microstrain, ε , can be obtained from [99]:

$$\beta_C^f = \frac{K\lambda}{D \cos \theta} \quad (2.3)$$

$$\beta_G^f = 4\varepsilon \tan \theta \quad (2.4)$$

where β_C^f and β_G^f are the integral breadths of the Cauchy- and Gaussian components of the structurally broadened profiles, respectively, the crystallite size, D , is the volume-weighted crystallite size in the direction parallel to the diffraction vector, λ is the wavelength and θ is the position of the diffraction-line maximum. The shape factor, K , used in this work was set to equal to unity. In order to determine the instrumentally broadened profile of the diffractometer as function of diffraction angle 2θ , 13 hkl reflections of the LaB₆ (NIST SRM660a) standard powder sample were measured (see above). The integral breadths and the Voigt parameters of the instrumental profile at the diffraction angles of the (Ni, Fe, Cu and W) reflections were then determined by interpolation and a Voigt-function approach was used to subtract instrumental broadening [154].

Line broadening induced due to the presence of stacking faults (mainly in fcc metals as Ni and Cu) has been neglected herein since the stacking fault probabilities obtained for the powders do not exceed 1 % (see Section 2.4.1) and hence the relative contribution of the stacking faults to line broadening is marginal which can be neglected in the line-broadening analysis for the Ni and Cu powders investigated in this work (the effect of stacking faults must be and is considered in the analysis of line *positions*; see below).

2.3.4 Lattice-parameter determination

Mechanical milling induces severe plastic deformation (SPD) that can lead to a considerable density of defects, in particular, a high density of planar, stacking faults in FCC metals. A precise determination of the lattice parameter in such faulted materials requires a correction for such stacking faults as stacking faults on the (111) planes of a FCC metal produce (broadening *and*) shifting of diffraction lines [155]. It is difficult to obtain information about faulting from only line-broadening measurements as the broadening is affected by both crystallite size and microstrain. However, the peak-maximum position is affected solely by faulting (in the absence of macrostrain) so that a direct determination of the stacking fault probability can be made using such data. The stacking fault probability α

can be determined from a change of the diffraction-angular separation of the 111 and 200 reflections with respect to a powder specimen containing no stacking faults. The diffraction-angular separation of the 111 and 200 diffraction lines, $(2\theta_{200} - 2\theta_{111})$, in the absence of stacking faults was obtained from a powder sample annealed at 900°C. The absence of crystal defects in this reference sample was verified by comparing its diffraction-line broadening with the instrumental line broadening as recorded from a LaB₆ powder sample: The line broadening (characterized by, for example, the full width at half maximum (FWHM)) of the powder sample was identical to that of the instrumental line broadening (obtained by interpolating the FWHM of the LaB₆ diffraction lines at the peak positions of the Ni/ Cu peaks). The effect of stacking faults is to move the 111 diffraction line to higher and the 200 diffraction line to lower diffraction angles; thus, the spacing between the 111 and 200 reflection lines decreases with increasing stacking fault probability according to [156].

$$\Delta(2\theta_{200} - 2\theta_{111})(^\circ) = -45\sqrt{3} \frac{2 \tan \theta_{200} + \tan \theta_{111}}{2\pi^2} \alpha \quad (2.5)$$

After determination of the stacking fault probability α on the basis of Eq. 2.6, the positions of all the measured diffraction lines investigated were corrected for peak shifts induced by the presence of stacking faults according to:

$$\Delta(2\theta) = -\frac{360}{\pi} G_{hkl} \alpha \tan \theta \quad (2.6)$$

where the factor G_{hkl} depends on the reflection hkl (for details and tabulated values of G_{hkl} , see Ref. [157]). This value of α calculated from 111 peak shift was used to correct the lattice parameter of Ni and Cu for individual hkl reflections.

After having performed the correction for peaks shifts induced by stacking faults, the offset of the diffraction-angle scale was corrected. As the measurements of the nanocrystalline powder specimens were carried out over an extended period of time, small changes of the offset might have occurred over this time period. For a rigorous correction of a possible instrumental offset of the diffraction-angle scale, a Nelson-Riley plot (i.e. a plot of the lattice parameter determined from individual reflections versus $\cos^2\theta/\sin\theta$) [158] was made and the lattice parameter was determined from the intercept of the ordinate in the Nelson-Riley plot. As an alternative to the Nelson-Riley extrapolation for determination of the lattice parameter, a simultaneous least-squares refinement of the lattice parameter and the offset of the diffraction-angle scale were performed employing seven different hkl reflections. These two procedures led to identical results for the lattice parameter within experimental accuracy.

2.4 Results

2.4.1 Microstructure of the ball-milled powders

The microstructure of the Ni powder ball milled for 80 h was investigated employing HRTEM analysis. Analysis of several micrographs (see Figure 2.1 for a representative example) indicates the presence of grains of the size of about 5-10 nm (overlapping grains obstruct the demarcation of the individual grains and hence to determine a size distribution quantitatively). The grain size determined from the TEM analysis is compatible with the grain size obtained from the X-ray diffraction-line broadening analysis (see below and Figure 2.2). Strongly varying contrast in the image indicates a highly defective structure. In a few suitably oriented grains edge dislocations can be identified. The grains are more or less spherical as opposed to the slightly elongated grains which were observed for the sample milled for smaller duration of 5 h [129], revealing a change of grain morphology upon prolonged milling.

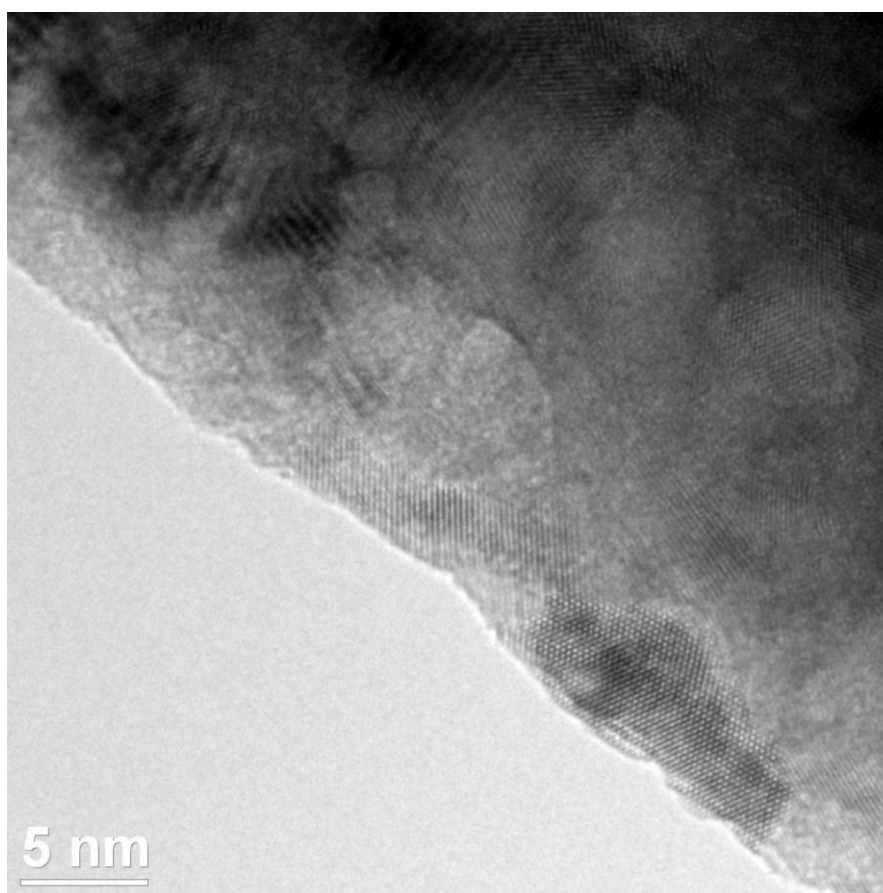


Figure 2.1: High resolution transmission electron micrograph of Ni powder after ball milling for 80 h. Image shows the presence of small crystallites of the size of \sim 5-10 nm.

XRD line-profile analysis shows that upon ball-milling, the crystallite size D of all metals investigated decreases rapidly, typically within about first 5 hours of milling time, and then continues to decrease at a lower rate followed by a saturation size for longer milling times (Figure 2.2). The microstrain correspondingly increases steadily with increasing milling time, indicating an increasing amount of crystal imperfection introduced upon continued milling. The decrease in grain size and increase of microstrain is faster for W milled in the SPEX mill, which is a higher energy mill.

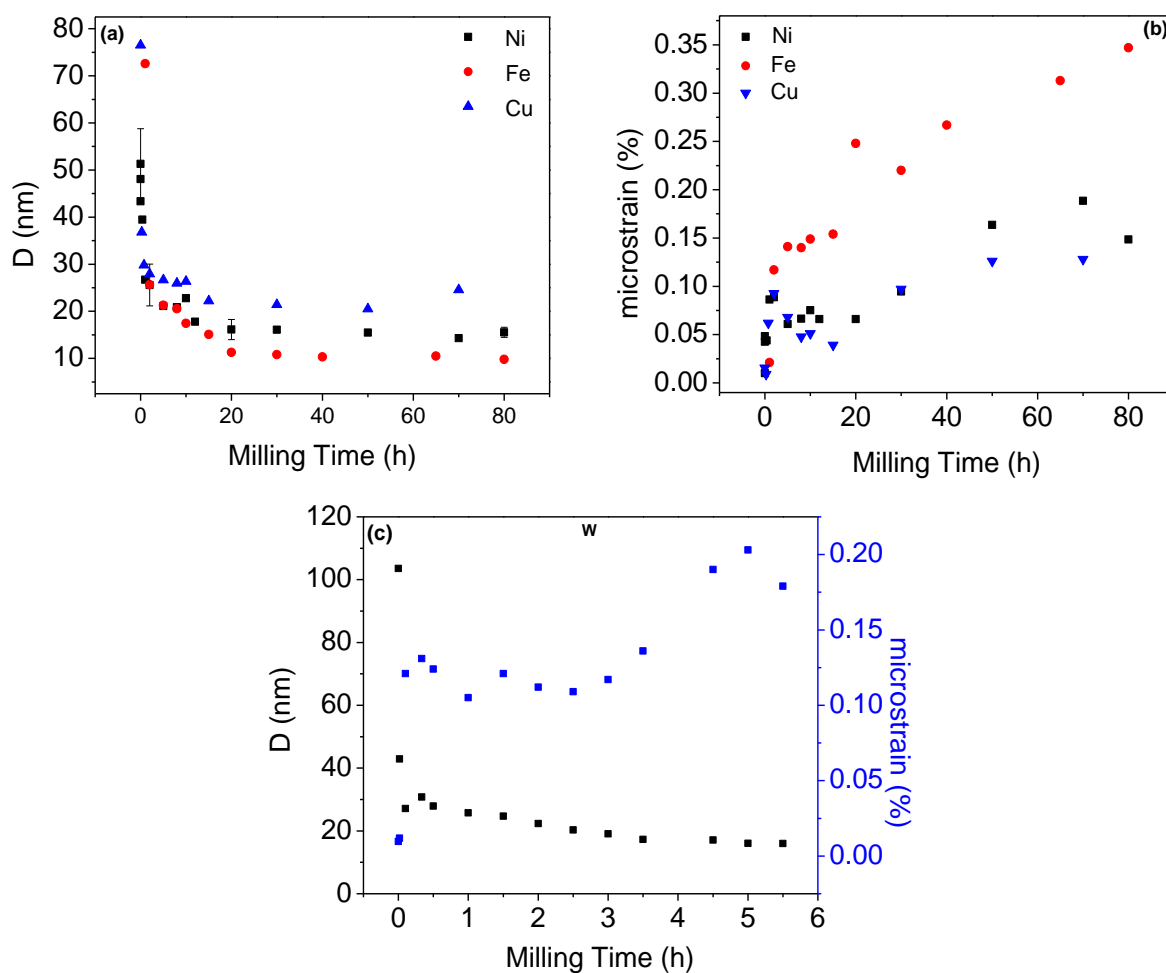


Figure 2.2: Crystallite size (D) and microstrain as function of ball-milling time. (a),(b): Powders milled in planetary mill (c) W milled in shaker mill.(Error bars for the microstrain values have not been included, as their size would be of the order of the size of the symbol used)

The stacking fault probability, α , for Ni and Cu is shown in Figure 2.3 as function of ball-milling time. With increasing milling time, the stacking fault probability increases for Ni to about 0.7 % and for Cu to about 1 %.

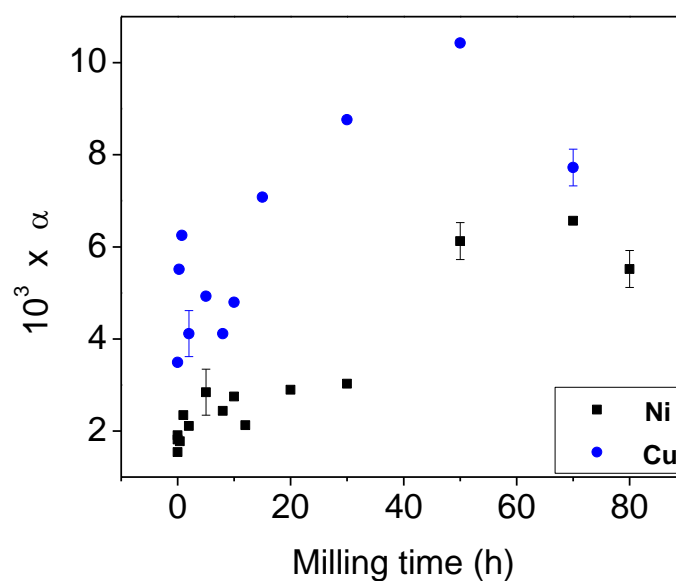


Figure 2.3: Stacking fault probability, α , of the Ni and Cu powders as function of ball-milling time.

2.4.2 Grain size-dependence of the lattice parameters

The lattice parameter changes (with respect to the lattice parameter (a_0) of coarse grained material) of the powder specimens have been plotted as function of the reciprocal crystallite size in Figure 2.4. A non-monotonic variation is observed for all the 4 metals investigated: with decreasing crystallite size, the lattice parameter first decreases and below a particular crystallite size, the lattice parameter starts increasing. Such a trend is observed in the ferromagnetic Fe and Ni powders as well as the non-magnetic W and Cu powders (with W milled in a higher energy mill).

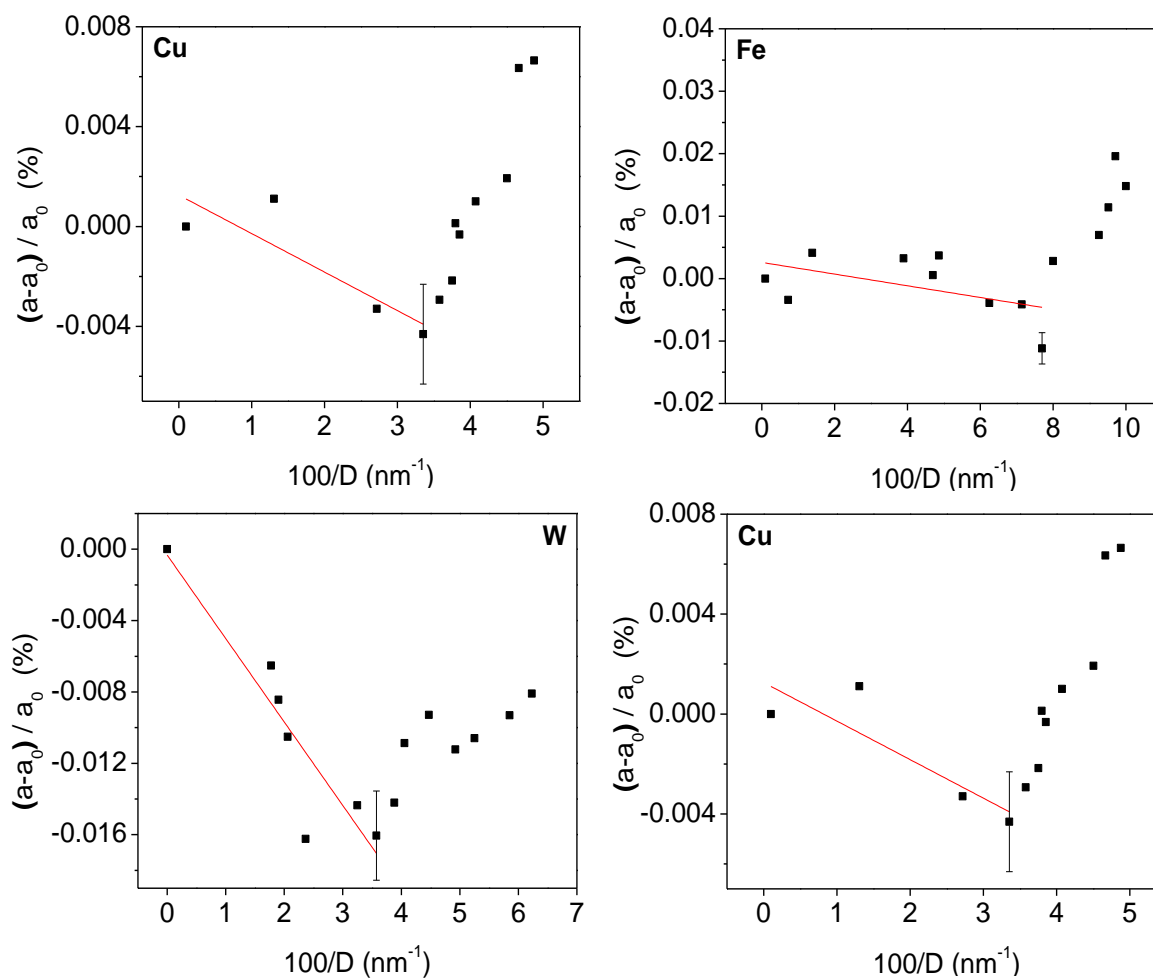


Figure 2.4: Relative change of the lattice parameter, $(a-a_0)/a_0$, (a_0 is the lattice parameter obtained for the as-received powder after annealing at 900°C for 10 min) as a function of the reciprocal crystallite size, D^{-1} , as measured from the powders (Ni, Fe, W and Cu) after ball-milling. (The line is a linear fit of the lattice parameter change with reciprocal grain size according to eq. 2.1– details in section 2.2.1)

2.5 Discussion

2.5.1 Microstructural evolution with milling

After an initial rapid decrease of the crystallite size with increasing milling time, the rate of grain-size reduction decreases and a minimal, stable crystallite size is obtained after about 30 h of milling (Figure 2.2). The microstrain values continually increase upon prolonged milling. This observation is typical for the microstructural development upon ball-milling [159]: The minimal achievable grain size and microstrain evolution is governed by a balance between the generation of crystal imperfection and dynamic recovery processes

due to the energy dissipation arising by trapping of powder particles during collisions between milling balls and between millings balls and the container.

The dependence of crystallite/grain size on milling time of FCC Cu and FCC Ni found in this work is in line with literature results for various FCC metals, where the smallest grain size is obtained for the metal with the largest bulk modulus and highest melting point (here: Ni) [160]. Similarly, the highest achievable microstrain value is dependent on the melting point of the material. Faster recovery simultaneously occurring with plastic deformation leads to lower microstrain values for metals with a lower melting points (here: Cu). Comparing FCC and BCC metals, a smaller saturation grain size is usually obtained for BCC metals exhibiting a higher melting point compared to FCC metals when milled under the same conditions (cf. results for W versus those for Ni and Cu in Figure 2.2).

The stacking fault probability (Figure 2.3), α , is significantly higher in the case of Cu as is expected on the basis of Cu having a lower stacking fault energy than Ni [161]. A decrease in α is observed for both Cu and Ni for the longest milled sample. A possible reason for this decrease could be the annihilation of deformation faults.

2.5.2 Non-monotonic lattice parameter variation with grain size

The lattice parameter decreases with decreasing grain size, reaches a minimal value and then starts increasing with further decrease of grain size. This contraction-expansion transition occurs for all metals studied. Only for W the lattice parameter for the smallest crystallite size is still below that of the coarse-grained. The grain size at which the expansion is observed obeys the inequality $D_{Cu} > D_{Ni} > D_{Fe}$ and thus complies with the order of the melting points. For W, which has a much higher melting point than Ni, Fe and Cu, the transition could thus be expected to occur at a much smaller grain size.

2.5.3 Fitting lattice contraction and expansion

The application of equation (2.3) for the crystallite/grain-size dependence of the lattice parameters requires data for the bulk modulus, interface stress and the grain-boundary width. The grain-boundary width can be taken as 1 nm [26] and the bulk modulus can be obtained from literature ($K_{Ni} = 177.3$, $K_{Fe} = 169.8$, $K_W = 311$, $K_{Cu} = 137$; [40]) Using equation (2.1) (c.f. section 2.2.1) and fitting the lattice-contraction region in the linear parts of the plots shown in Figure 2.4, leads to interface-stress values of 0.39 Nm^{-1} for Ni, 0.12 Nm^{-1} for Fe, 1.12 Nm^{-1} for W and 0.22 Nm^{-1} for Cu. When these interface stress values are inserted in

equation 2.3, it follows that with decreasing grain size, only lattice expansion would be expected, which is in striking contrast with the experimental results presented here. As determination of the interface stress on the basis of equation 2.1 ignores the effect of grain-boundary excess volume on the lattice parameter, this approach would only be correct if the lattice parameter variation in the region of grain size employed for fitting would be dominated by the Gibbs-Thomson effect. Indeed, exemplary calculations (see Figure 2.5 for an example) demonstrate that this approximation is not valid.

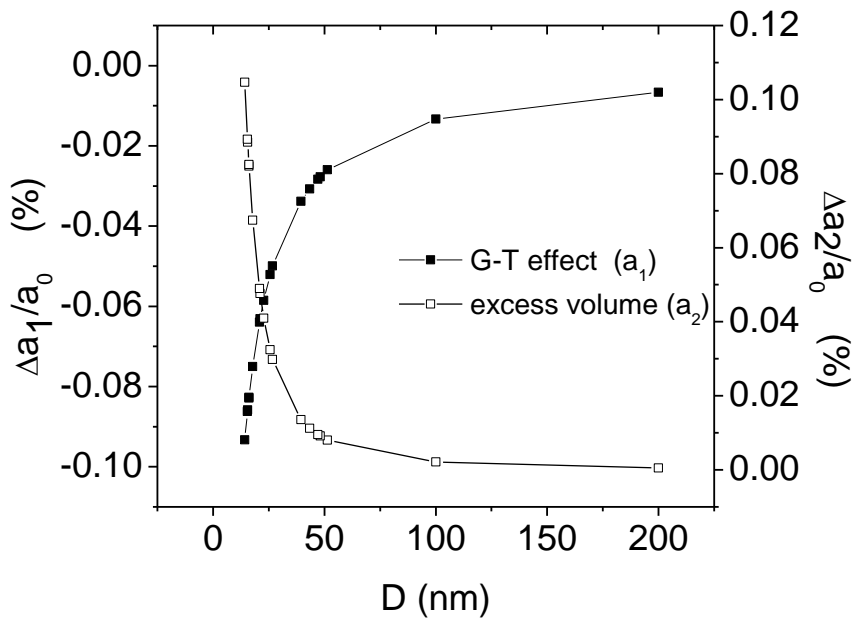


Figure 2.5: Relative change of lattice parameter as function of grain size according to equation 2.1 and according to equation 2.2.

Consequently, the combined expression for lattice parameter variation (i.e. equation 2.3) has to be fitted to the experimental data, where the interface stress value σ_s is the only fitting parameter. Such a fitting, indeed, is compatible with the contraction \rightarrow expansion behaviour of the lattice parameter. Results of such fits are shown in Figure 2.6. In view of the simplicity of the model represented by eq. 2.3, the quality of the fits should be considered reasonable.

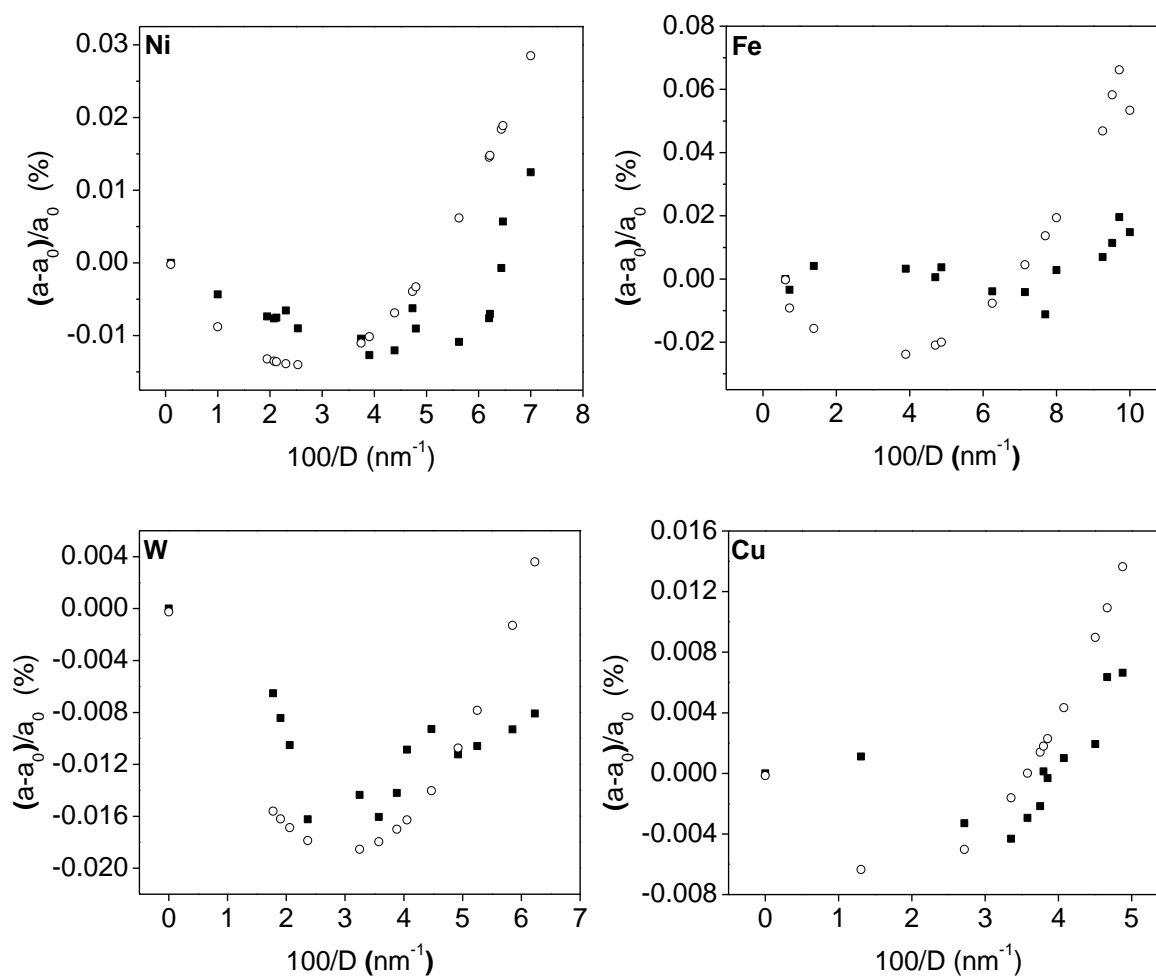


Figure 2.6: Relative change of the lattice parameter as a function of reciprocal grain size, as obtained experimentally (closed symbol) and as obtained by fitting equation 2.3 to determine a value for the interfacial stress (open symbol) for Ni, Fe, W and Cu.

The interface stress values obtained by this approach are: 1.47 Nm^{-1} for Ni, 1.8 Nm^{-1} for Fe, 2.9 Nm^{-1} for W and 0.8 Nm^{-1} for Cu (indeed, distinctly different from the above mentioned values (see Table 2.2)).

Table 2.2: Values of grain-boundary interface stress as obtained by fitting equation 2.1 (based on the G-T effect) and as obtained by fitting eq. 2.3 to the contraction and expansion parts of the lattice parameter as a function of the grain size for the elemental ball milled powders.

σ_s (N/m)	Cu	Ni	Fe	W
Equation 2.1	0.22	0.39	0.12	1.12
Equation 2.3	0.8	1.47	1.8	2.9

The values obtained from fitting eq. 2.1 to the contraction part are much smaller than the values obtained by fitting eq. 2.3 which, moreover, correlate with literature data (see Figure 2.7). It has been observed empirically that the interfacial stress value increases (linearly) with the melting temperature [50], which complies with the present results for Ni, Cu, Fe and W.

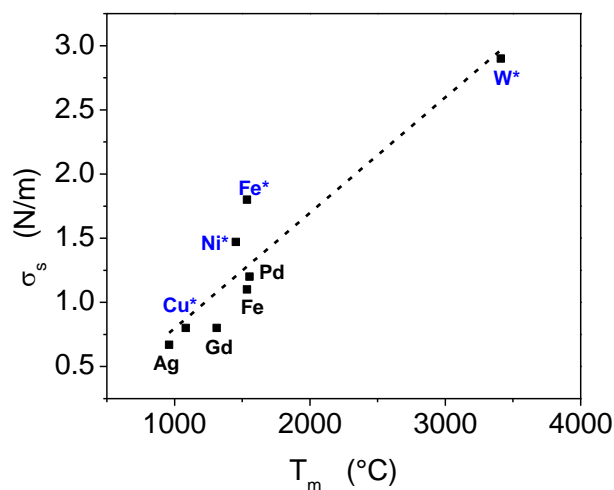


Figure 2.7: Grain-boundary interface stress as a function of melting temperature (T_m) (* mark the data obtained in the present work); Ag [50], Gd [162], Pd [119] and Fe [125].

These results of the present investigation thus lead to the following model description: Upon ball milling, with decreasing grain size down to about 50-30 nm, the excess volume generated in the grain boundaries is relatively small and the interface-stress induced lattice contraction predominates. Upon prolonged ball milling (approximately after 20 h of milling), at grain sizes smaller than about 50-30 nm, the excess volume induced lattice expansion prevails (i.e. the increasing Δa_2 (equation 2.2) has become larger than the decreasing Δa_1 (equation (2.1)) for the same grain size).

2.6 Conclusion

- 1) A non-monotonic variation of lattice parameter with crystallite size has been observed in the ball milled powder specimens of Ni, Fe, Cu and W: lattice contraction followed by lattice expansion upon decreasing crystallite/ grain size.
- 2) The non-monotonic variation of the lattice parameter can be understood as follows: Upon decreasing grain size, the hydrostatic pressure on the grain boundaries induced by interface stress results in lattice contraction. Upon continued decrease of grain size, a critical grain size value is passed beyond

which the lattice parameter increases as a consequence of the stress field induced by excess free volume in grain boundaries.

- 3) A simple model combining the effects of excess free volume (Ref. [44]) and the interface stress can be used to assess the value of the interface stress by fitting this model to the experimental data, with the interface stress as the only fit parameter. The interface stress appears to increase almost linearly with increasing melting point. The interface stress values thus obtained are comparable with literature values.

Chapter 3

Grain growth studies on nanocrystalline Ni powder

G. K. Rane, U. Welzel, E. J. Mittemeijer

Abstract

The microstructure of nanocrystalline Ni powder produced by ball milling and its thermal stability has been investigated by applying different methods of X-ray diffraction line-profile analysis: Single-line analysis, whole powder-pattern modelling and the Warren-Averbach method have been employed. The kinetics of grain growth have been investigated both by *ex-situ* and *in-situ* X-ray diffraction measurements. With increasing milling time, the grain-size reduction is accompanied by a considerable narrowing of the size distribution and an increase of the microstrain. Upon annealing, initial, rapid grain growth occurs which is accompanied by the (almost complete) annihilation of microstrain; for longer annealing times, the grain-growth kinetics depend on the initial microstructure: a smaller microstrain with a broader grain size distribution leads to linear grain growth followed by parabolic grain growth, whereas a larger microstrain with a narrow grain-size distribution leads to incessant linear grain growth. These effects have been interpreted on the basis of annihilation of defects at grain boundaries and the resulting changes in the excess free volume at the grain boundaries.

3.1 Introduction

Studies of nanocrystalline materials, for over two decades now, have revealed great possibilities for fundamental scientific as well as applied research in view of their interesting and anomalous properties (which moreover are often superior to the properties of coarse-grained materials) [6, 163]. The major cause of the special properties of nanocrystalline materials appears to be the large volume fraction of atoms situated at grain boundaries, as compared to coarse grained materials [19, 65]. The nanocrystalline state is far from equilibrium, in particular, because of this large grain-boundary area and this explains an intrinsic instability of the nanocrystalline microstructure against grain growth upon annealing.

Grain growth is driven by the system's desire to stabilize itself by minimizing its Gibbs energy which can be achieved by the reduction of grain-boundary area [164]. Several studies have indicated unexpected and, in particular, adverse differences in the grain-growth process in nanocrystalline materials [64, 67, 68]. For example, while some studies observed the onset of grain growth at homologous temperatures much lower than that for coarse-grained materials [64], few other studies indicated occurrence of grain growth for nanocrystalline materials at temperatures higher than for coarse-grained materials [64]. Moreover, the isothermal growth kinetics was found to be incompatible with that observed for coarse-grained materials; in certain studies an incubation period before the onset of grain growth was observed [165] and in other studies a rapid initial grain growth was followed by abrupt stagnation of grain growth [70].

The classical interpretation for grain growth in coarse-grained materials, as governed by the decrease of total grain-boundary energy, may not suffice for nanocrystalline material because, apart from the significant role of grain boundary energy, (energy effects of) other features such as triple lines [166], quadrupole junctions [76], excess vacancies in the bulk of the grains or excess volume at the grain boundaries [167, 168] can also affect the kinetics of grain growth.

Ball milling introduces severe plastic deformation of the powder particles which results in refinement of the grains down to the nanometer regime [159, 169]. As such, the deformation leads to the formation of nanocrystalline material with a complex microstructure manifested by the presence of defects such as dislocations, deformation (planar) faults, introduction of excess vacancies and a high grain boundary density with high-density ensembles of non-equilibrium dislocations in the grain boundaries which

results in an overall high energy (non-equilibrium) state of such nanocrystalline systems [69, 145]. As a consequence, some studies revealed that nanocrystalline materials synthesized by mechanical means exhibited enhanced diffusivities[43]: self-diffusion coefficients in such prepared nanocrystalline fcc materials can be about 2 to 4 orders of magnitude larger than the grain-boundary self-diffusion coefficients in their conventional, polycrystalline coarse-grained counterparts [170, 171].

Some studies have shown that the grain-boundary mobility is relatively small in nanocrystalline systems due to the large strain accumulated in the grain-boundary adjoining regions [172], which strain is mainly due to a high density of grain-boundary dislocations [173]. Moreover, excess free volume freed during grain growth is transformed into vacancies that leads to a retarding effect on the grain-growth kinetics [174] by reduction in the driving force for grain growth below a critical grain size [70] by ‘locking’ the grain boundaries [168]. It was suggested in Ref. [70] that enhanced stability against coarsening resulted from the redistribution of the excess volume in the grain-boundary cores.

In any case, it can be concluded that the grain-growth behaviour in nanocrystalline material is distinctly different from that in coarse-grained materials. The rate-controlling mechanisms for grain growth may change in the nano-regime, e.g. from an initial fast exponential growth possibly controlled by quadruple junction motion to a linear growth possibly controlled by triple junction (TJ) motion, followed by the normal grain-boundary (GB) curvature driven parabolic growth [76]. Further, in a recent study [79] abnormal grain growth was suggested to be the rate-controlling mechanism for grain growth in the transition region from TJ to GB curvature driven kinetics.

In view of the above described inconclusive understanding of grain growth in nanocrystalline materials, the aim of this present work was to understand the grain growth process in severely deformed nanocrystalline Ni powder prepared by ball milling. Several growth models have been applied to our data and the merits and flaws of these models have been discussed in a comparative manner.

3.2 Theoretical background

3.2.1 Grain-growth kinetics

Classically, grain-coarsening [62, 68] is ascribed to the movement of grain boundaries induced by their curvature: the pressure acting on a grain boundary is given by $\alpha \cdot 2\gamma/r$

where r is an average radius of curvature, α is a geometrical constant ($\alpha = 1$ for a spherical grain boundary) and γ the (grain-boundary) interfacial energy assumed to be a constant for all grain boundaries. The grain-boundary velocity then is given as $v = dr/dt \propto M * 2 \gamma/r$ where M is the grain boundary mobility. Then adopting $2r$ as an estimate for the average grain size, D , the rate of grain growth can be given by

$$dD(t)/dt = a_1/D(t) \quad (3.1)$$

where a_1 incorporates the terms introduced above. Upon integrating it is obtained

$$D(t)^2 - D(0)^2 = k_1 t \quad (3.2a)$$

To allow deviations of the value of the exponent in this equation one often writes

$$D(t)^n - D(0)^n = k_1 t \quad (3.2b)$$

which is called the *generalized parabolic grain growth model*. The rate constant k_1 is temperature dependent and is used for the determination of the activation energy of the grain-growth process. The grain-growth exponent, n , is found to differ from 2 for nanocrystalline materials [175] and also appears to be temperature dependent [64].

This theory was modified [164, 176] in order to account for grain-growth stagnation upon prolonged annealing (as due to a vanishing driving pressure, grain-boundary pinning by second phase particles (Zener drag), solute drag, pore drag, etc.) leading to a saturation grain size D_∞ at each annealing temperature. Therefore, Eq. 3.1 was supplemented with a growth-retarding term, b_2 , yielding

$$\frac{dD(t)}{dt} = \frac{a_2}{D(t)} - b_2 \quad (3.3)$$

which is called the *grain-growth model with impediment*. This model was further modified [84] based on the argument that the growth-retarding effect should be a function of the grain size ($b_2 \propto D$) since the impurity concentration in the grain boundaries increases during grain growth, recognizing that the grain boundary area/volume fraction decreases, and thus

$$\frac{dD(t)}{dt} = \frac{a_3}{D(t)} - b_3 D(t) \quad (3.4)$$

which is called the *grain-growth model with size-dependent impediment*.

It should be noted that literature on the grain-growth process in nanocrystalline materials, as referred to in section 3.1, suggests that not a single growth controlling mechanism at all length scales occurs, but that the growth process involves different mechanisms at different length scales, even in the absence of impurities. For example, based on simulation studies [77], it was proposed that, below a (temperature-dependent) critical grain size D_c , the excess volume in the grain-boundary region (relative to the single crystalline state), released during grain growth, is incorporated into the bulk of the

crystalline regions as vacancies. With increasing concentration of these vacancies, the system experiences an increase of the energy. This increased energy counteracts the decrease of energy realized by the reduction in grain-boundary area during grain growth and thus an overall slowdown of the grain-growth rate can occur causing an only linear increase in grain size with annealing time. The growth kinetics below this critical grain size D_c can be given as [77]:

$$D(t) = D_0 + \frac{\gamma D_{SD}}{12 N k_B T Z [\delta V/A]^2} t \quad (3.5)$$

where D_0 is the initial grain size, D_{SD} is the bulk self-diffusion coefficient, N is the number of atoms per unit volume, k_B is the Boltzmann constant, T the annealing temperature, Z the atomic coordination number, γ the grain-boundary energy and $\delta V/A$ represents the excess volume per unit grain boundary area. The model was applied to grain growth in nanocrystalline-Fe [70].

3.2.2 X-ray diffraction line-profile analysis

In order to study changes in the microstructure, X-ray diffraction (XRD) is a non-destructive powerful tool in particular for application to nanocrystalline materials [94, 95]. XRD is often the most (also and in particular statistically) reliable tool at hand when studying bulk specimens. From the diffraction-line parameters as peak width, position, shape and intensity of the diffraction lines, information regarding the distribution of phases, crystallite size and shape distribution, concentration and distribution of crystal defects such as dislocations, faults, twins etc. can be determined [94-96].

In this work, the grain (crystallite) size and the microstrain (and dislocation density) and faulting parameters of the (heavily deformed) nanocrystalline material have been extracted from measured powder diffraction patterns. Whereas size and microstrain are derived from the line broadening, the faulting probability can be determined from the line-position shift (e.g. from the diffraction angular separation of Ni 111 and 200 reflections as compared to its defect-free counterpart – for details, see ref. [129]). Three different diffraction profile-analysis methods have been applied in the present work, which have been briefly described below.

3.2.2.1 Integral breadth method: Single-line analysis [154]

The measured profile h is a convolution of the specimen profile f and the instrumental profile g . If it is assumed that the instrumental profile g and the measured profile h can also be represented by Voigt functions, a simple correction for instrumental

diffraction line-broadening on the basis of the integral breadths and Voigt parameters of the measured and instrumentally broadened line profiles is possible as well [96] by subtracting the instrumental Lorentzian and Gaussian integral breadths of the instrumental profile from the Lorentzian and Gaussian integral breadths of the measured profile linear and quadratically, respectively.

It is assumed that the specimen profile f can be described by a Voigt profile, which is a convolution of a Gaussian and a Lorentzian profile, where the Gaussian component of the profile is due to the microstrain ε and the Lorentzian component of the profile is due to the finite crystallite size [96, 154]. The integral breadths β_C^f and β_G^f of the Lorentzian (Cauchy) and Gaussian components, respectively, can be related to the volume-weighted column length, L , and the microstrain ε :

$$\beta_C^f = \frac{\lambda}{L \cos \theta} \quad (3.6)$$

$$\beta_G^f = 4 \varepsilon \tan \theta \quad (3.7)$$

where λ is the wavelength and θ is the Bragg angle.

The volume-weighted crystallite size (diameter) D_v can be calculated from the volume-weighted column length L if an assumption for the crystallite shape is adopted [177]. In this work, a spherical crystallite shape has been assumed, hence $L = 3D_v/4$.

3.2.2.2 Whole powder pattern modelling [94, 103, 178, 179]

In the whole powder pattern modelling (WPPM) method a pattern is synthesized directly from physical models describing the microstructure of the material under study and the model parameters are then fitted to the measured data, thus overcoming the bias which is introduced in integral breadth methods due to the arbitrariness of using analytical profile functions. The method has been applied to several cases; for a review, see Ref. [180]. The theoretical basis is briefly described here. The diffraction profile can be written as

$$I_{(hkl)}(d^*, d_{(hkl)}^*) = k(d^*) \sum_{hkl} w_{hkl} \int_{-\infty}^{\infty} \mathcal{C}_{hkl}(L) \exp[2\pi i L (d^* - d_{\{hkl\}}^* - \delta_{hkl})] dL \quad (3.8)$$

where $d_{(hkl)}^*$ is the value of the reciprocal space variable d^* in the Bragg position and $k(d^*)$ includes constants and known functions of d^* . w_{hkl} and δ_{hkl} are, respectively, the weight of a reflection (related to its multiplicity) and the shift of a reflection from the exact Bragg position for an (hkl) member of the $\{hkl\}$ family of crystallographic planes. The last parameter is related to lattice defects, like faulting, which, in addition to a profile broadening, cause different shifts of the various (hkl) subcomponents. As a consequence, the observed peak profile is expressed as a weighted sum of all the different subcomponents.

The Fourier transform $C_{hkl}(L)$ includes all the instrumental and specimen related effects such as the instrumental profile, domain size, faulting, dislocations, antiphase domain boundaries all of which are described by physical models.

In the present work, the XRD patterns were modelled by using the PM2K [178], a software based on the WPPM approach that allows refinement of the data by non-linear least squares routine. The instrumental component is handled by a pseudo – Voigt fit of a suitable line profile standard (eg. LaB₆ NIST SRM660a). The background (described with a Chebyshev polynomial of degree 3), peak intensities, specimen displacement and the lattice parameter of Ni were refined simultaneously for each pattern. A spherical-shaped lognormal distribution of crystallite size was adopted for the fitting. The specimen-related physical broadening parameters (to be determined by the fitting) were the mean (μ) and variance (σ) of a lognormal size distribution adopted for the spherical crystallites/domains, the dislocation density (ρ) and the effective outer cut-off radius of Ni. Additionally, the faulting parameters α (deformation) and β (twin) were included for Ni which has an fcc crystal structure. The average contrast factors for edge and screw dislocations were calculated for the $\langle 110 \rangle \{111\}$ slip system with Burgers vector $a_0/(2^{1/2})$ for Ni.

3.2.2.3 Warren - Averbach method [95, 96, 100, 101, 181]

The Warren – Averbach (W-A) method [100, 101] is a Fourier method which also allows the separation of size and strain effects and in principle could enable determination of the crystallite/grain-size distribution. The convolution of the size-broadened and the strain-broadened profiles in real space corresponds to the product of their Fourier transforms in reciprocal space. Thus the Fourier coefficients of a physically broadened line profile are the product of size and distortion coefficients:

$$A(L, S_i) = A^S(L)A^d(L, S_i) \quad (3.9)$$

where $A^S(L)$ denotes the order-independent size Fourier coefficient, $A^d(L, S_i)$ is the order-dependent strain, Fourier coefficient, and L is a correlation distance in the crystals perpendicular to the diffracting planes. If more than one order of reflection is available and the dependence of $A^d(L, S_i)$ on the order of the reflection is specified, separate information on $A^S(L)$ and $A^d(L, S_i)$ can be obtained. Assuming a Gaussian strain distribution for all values of L , dependence of $A(L, S_i)$ on the order of reflection then is given by

$$\ln A(L, S_i) = \ln A^S(L) - 2 \pi^2 S_i^2 L^2 \langle \epsilon^2(L) \rangle \quad (3.10)$$

where $\langle \epsilon^2(L) \rangle$ is the mean squared strain for the correlation distance L . From the plot of $A(L, S_i)$ (at fixed L) versus S_i^2 for several (at least two) reflections, the size Fourier

coefficients $A^S(L)$ are obtained from the intercepts and the strain Fourier coefficients are obtained from the slopes. The area-weighted column length can be determined from the size coefficients and $\langle \varepsilon^2(L) \rangle$ can be deduced from equation 3.10 (see also [182]). Assuming a spherical crystallite shape, the area-weighted grain size, D_a , can be given as $L = 2D_a/3$

For the W-A method, very good counting statistics and a wide angular measuring range are necessary. Such requirements can hardly be satisfied for *in-situ* diffraction experiments. The W-A method of analysis (for *ex-situ* measurements) was adopted to determine the grain-size distribution for a few selected specimens. To this end, long time measurements, at ambient temperature, were carried out for the 111-222 and 200-400 diffraction lines of the nanocrystalline Ni specimens.

In the absence of strain broadening $A^d(L, S_i)$ is constant (=1). Then the entire broadening can be attributed to crystallite-size broadening. Hence, the Fourier coefficients can be directly used to determine the area-weighted column-length and the column-length distribution $p(L)$ separately for each reflection from the second derivative of the cosine Fourier size coefficients $A^S(L)$ [183]. The instrumental corrections were performed by the Stokes deconvolution method using an annealed specimen of Ni, which is practically defect-free and coarse grained, for the determination of the instrumental broadening [93].

The determination of crystallite/grain-size distribution by the above procedure poses several problems ([184, 185] and references therein for an overview of the problems), such as oscillations in the plot of the $A^S(L)$ against L curve upon correction for instrumental broadening by deconvolution in Fourier space, small shifts in the $A^S(L)$ values depending on the counting statistics. In particular, the assumption used for the microstrain, necessary for the size-strain separation (e.g. Eq. 3.10), is probably the biggest source of error rendering, in the presence of appreciable strain broadening, such size-distribution determination unreliable.

Several alternative methods have been employed to overcome some of the problems however with a few assumptions. For e.g., fitting an analytical function, such as a Voigt or Pearson VII function, to the diffraction peak and using this fit function for Fourier transformation and further W-A analysis [63, 184]. While such a method leads to lower statistical fluctuations, easier determination of background and no truncation effects making handling of the data much easier, such assumptions impose “physical behaviour” incompatible with reality. Moreover, the mathematical formulation of such functions in case of an assumed Voigt function, for e.g., requires the ratio of the volume-averaged and area-averaged grain size to be in the range of 1.31 to 2 [186]. Another procedure of limited

validity is the adoption of an analytical approximation for the size distribution which usually implies a monomodal size distribution.

3.3 Experimental details

3.3.1 Specimen preparation and processing

Ball milling of Ni powder (purity 99.8 wt. %, particle size \leq 300 mesh) was carried out in a planetary mill (Fritsch Pulverisette P6) operated at a rotation speed of 150 rpm with a ball to powder weight ratio of 10:1 in a vessel made of Ni with Ni milling balls to avoid contamination by abrasion of the milling vessel and the balls. To avoid other contaminations (as oxygen from the atmosphere) handling of the powders and filling and sealing of the milling vessels was carried out in an argon glove box.

All powder specimens were analyzed for metallic impurities by inductively-coupled optical emission spectroscopy and for oxygen and nitrogen impurities by carrier-gas hot extraction. For the specimen milled for the longest duration for each element, oxygen contamination was found to be about 0.3 at. % and nitrogen contamination was found to be less than 0.01 at. %. The X-ray diffraction patterns of all the powder specimens did not show any presence of impurity phases.

3.3.2 X-ray diffraction measurements

X-ray diffraction (XRD) line-broadening measurements for microstructural investigations were performed with Cu-K α radiation employing a Bruker D8 Advance θ - θ diffractometer operating in Bragg-Brentano geometry equipped with a K β absorption edge filter of Ni in front of a 1D position-sensitive VANTEC-1 detector. The measured diffraction patterns were analyzed using the Philips Profile Fit V1.0c software [151] by fitting a pseudo-Voigt function with the α_2/α_1 ratio set to 0.5 for the determination of the diffraction-line positions, the intensities, the full widths at half maximum and the peak-shape parameters. The instrumental broadening was characterized by measuring a LaB₆ powder specimen (NIST Standard Reference Material 660a).

The heating experiments were conducted at various temperatures ranging from 300 °C to 850 °C on the specimen mounted on the diffractometer, under N₂ - H₂ atmosphere (98 % N₂, 2 % H₂), with a gas flow of 0.7 l/min in an Anton Paar HTK 1200N oven chamber. Both temperature varying (a heating rate of 0.5 °C/s was used) and isothermal measurements have been carried out by *in-situ* X-ray diffraction measurements. The

diffraction angle (2θ) scan range was divided into three ranges to optimize the measurement conditions (the time per step was selected so that a peak maximum intensity of at least 2000 counts was achieved) and reduce the measurement time. The entire measurement (all three ranges) took about 1 h.

3.4 Results and Discussion

3.4.1 Microstructural evolution upon milling

The Ni 111 diffraction profiles in Figure 3.1 show the peak broadening induced upon prolonged ball milling for a maximum milling time of 80 h. The diffraction-line broadening was analysed employing the single-line analysis (SLA) and the whole powder-pattern modelling (WPPM) method (cf. Sections 3.2.2.1 and 3.2.2.2).

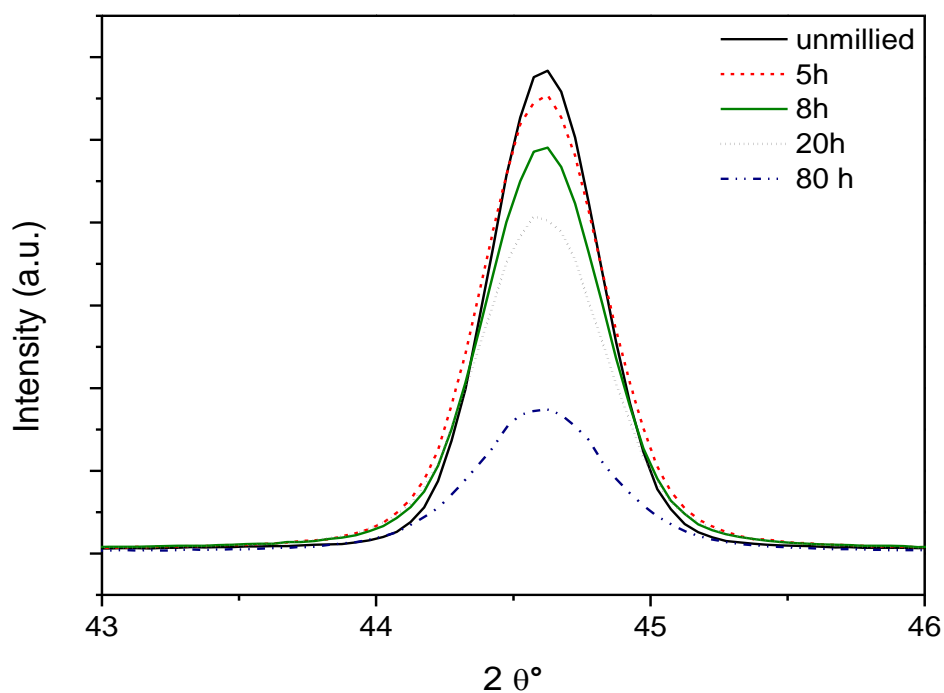


Figure 3.1: X-ray 111 diffraction-line profiles of Ni powder recorded after various milling times.

The results obtained from SLA for the volume-weighted average crystallite size from the column length (adopting spherically shaped grains) and the microstrain have been collected in Table 3.1 together with the results from WPPM for the mean crystallite size and the dislocation density. It follows that after an initial rapid decrease of the average crystallite size of Ni within the first 5 h of milling, the rate of reduction of crystallite size

decreases and a saturation crystallite size of about ~ 18 nm is reached after 80 hours of milling. The microstrain evolution obtained from SLA as well as the dislocation density obtained from WPPM show similar increasing trends with increasing milling time.

Table 3.1: Microstructural parameters as obtained by SLA (volume-weighted crystallite size assuming a spherical shape) and WPPM (average crystallite size assuming spherical shape and lognormal distribution) upon milling.

Milling time (h)	SLA		WPPM	
	D (nm)	Microstrain	D (nm)	Dislocation density ($10^{18} / \text{m}^2$)
0	86 (55)	5.29405E-4	124 (7)	0.00172
3	41 (32)	0.00123	54 (5)	0.00393
5	35 (29)	0.0013	38 (2)	0.00873
9	27 (26)	0.00109	24 (2)	0.01239
20	22 (17)	0.00201	23 (1)	0.01614
40	20 (13)	0.0025	22 (1)	0.01575
60	20 (13)	0.00312	19 (1)	0.01545
80	18 (10)	0.00271	18 (1)	0.01724

The stacking fault probability was obtained employing the WPPM method and from a separate quantitative evaluation of peak-position shifts [129](quantitative comparison). An excellent agreement of the stacking fault probabilities obtained by the two methods of analysis is evident from Figure 3.2. The crystallite-size distribution (Figure 3.3) (obtained adopting a log-normal size distribution of spherical crystallites) was obtained adopting the WPPM approach. It follows that a narrowing of the crystallite-size distribution occurs after about 9 h of milling. After 80h of milling, a very narrow crystallite-size distribution of small grains is obtained.

Upon ball milling, plastic deformation by dislocation processes can initially lead to elongation of grains and thus a broader size distribution in association with a non-homogeneous microstrain (for example see the results for the 5 h milled specimen). The formation of more equi-axed grains and a narrow size distribution (80 h milled specimen) in association with a uniform microstrain takes place upon prolonged deformation [187].

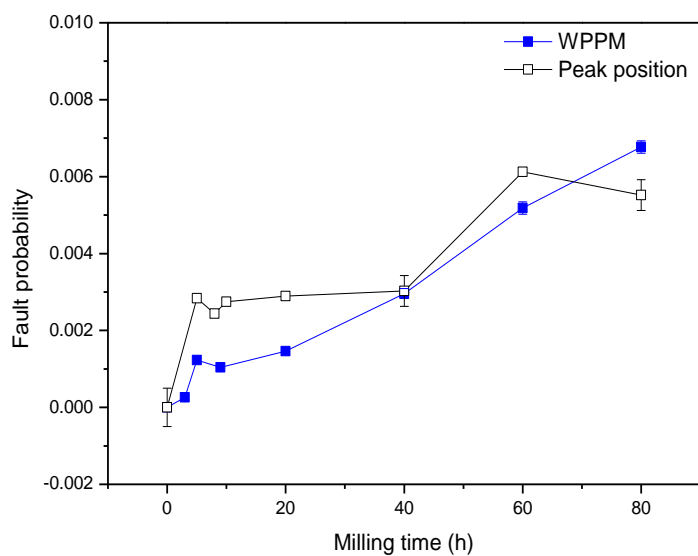


Figure 3.2: Stacking fault probability as obtained from WPPM and as calculated from the peak shifts.

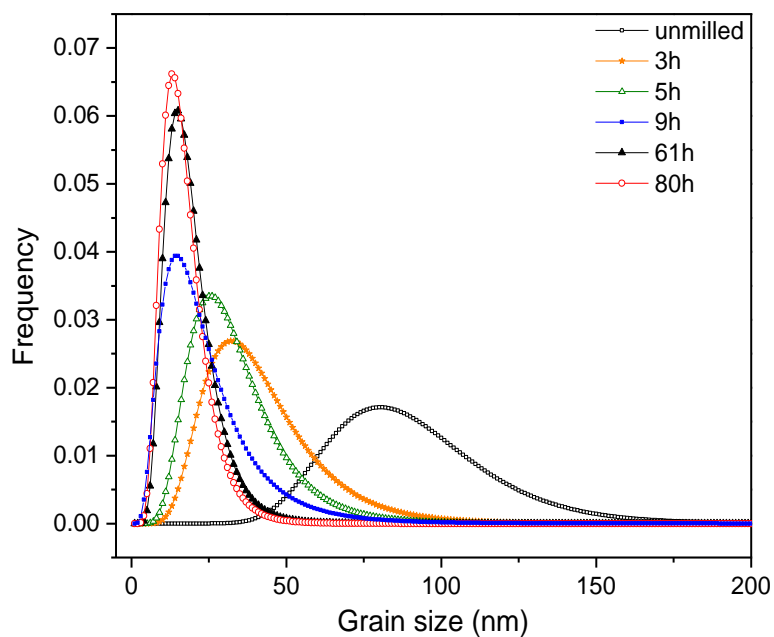


Figure 3.3: Grain-size distribution as a function of milling time obtained from WPPM.

3.4.2 Microstructural evolution upon annealing

Samples from powders milled for 5 h and 80 h were used for grain-growth studies recognizing their distinctly different initial microstructural features: The 5 h milled and 80 h milled specimens have crystallite size of about 30 nm and 15 nm, respectively. The microstrain is much larger in the 80 h milled specimen. The microstructure of the 80 h

milled specimen is likely more homogeneous than the 5 h milled specimen (note the very narrow crystallite-size distribution of the 80 h milled specimen: cf. Figure 3.3). The grain growth studies were carried out for extended annealing times in order to cover the entire growth process.

To investigate the grain coarsening behaviour, the milled samples were first examined by heating the 5 h milled and 80 h milled specimens at a rate of 0.5 K/s to a particular temperature, followed by isothermally annealing for 10 h (at each temperature), before proceeding to the next higher temperature. The 5 h milled specimen was annealed in steps of 25 °C, starting at room temperature and the 80 h milled specimen was annealed, in steps of 50 °C. Owing to the limited time period for XRD measurement, in view of the continuously changing microstructure during the isothermal holds, application of WPPM (requiring measurements over extended 2θ ranges) was impossible. The SLA method is less sensitive to such ongoing microstructural changes as single diffraction lines are analyzed. The obtained values for the crystallite size and the microstrain thus represent average values over the time period of one measurement. The column length and microstrain evolution for both specimens obtained employing the SLA has been plotted in Figure 3.4 for the first and last measurement at each temperature.

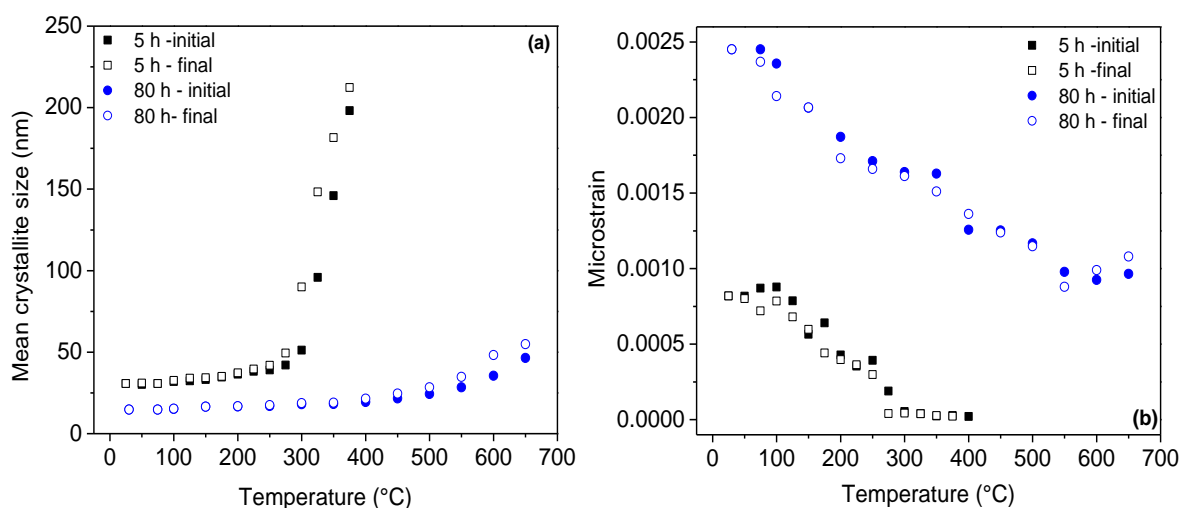


Figure 3.4: (a) Crystallite size and (b) microstrain evolutions as a function of annealing temperature for the 5 h and 80 h samples. (the filled symbols represents the data for the first measurement and the open symbol for the final measurement at the particular temperature)

It can be observed from Figure 3.4 that in the 5 h milled Ni specimen the grain size remains practically unchanged up to a temperature of about 250 °C while the microstrain continuously decreases. Upon reaching a temperature of 275 °C almost the entire

microstrain content has relaxed and the onset of grain growth occurs. For the 80 h milled specimen, the grain size remains almost constant up to even 500 °C, while the microstrain, similar to the 5 h milled specimen, decreases continuously. However, even after annealing to 700 °C, a significant amount of microstrain is still present (i.e. very much more than present in the 5 h milled specimen that was annealed up to 400 °C). It follows that the finer-grained specimen milled for 80 h shows a much higher stability against grain coarsening.

3.4.2.1 Isothermal grain-growth studies

Based on the measurements with constant holding times at each temperature (see above), appropriate temperatures for isothermal annealing investigations (i.e. temperatures at which noticeable grain growth occurs within a time period of 10 hours) were identified. The crystallite size and microstrain evolutions, as obtained by SLA, during isothermal annealing of specimens milled for 5 h at annealing temperatures between 250 °C and 375 °C, are shown in Figure 3.5.

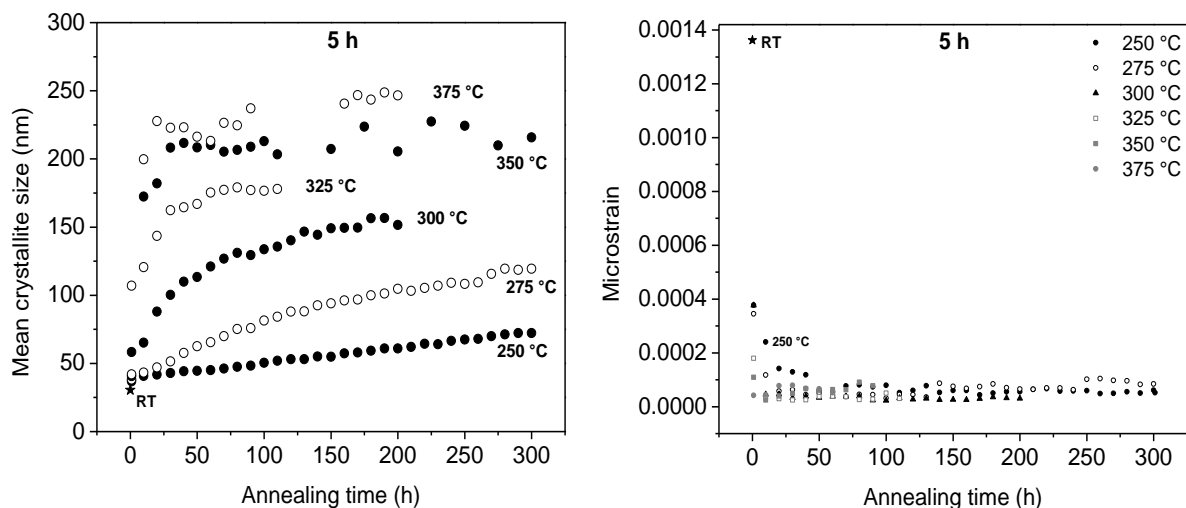


Figure 3.5: (a) Crystallite size and (b) microstrain evolutions as a function of annealing time at various temperatures for the 5 h milled specimen.

At each temperature, an initial, practically entire relaxation of the microstrain is accompanied by a stage of very rapid grain growth following apparently linear growth kinetics (Figure 3.6).

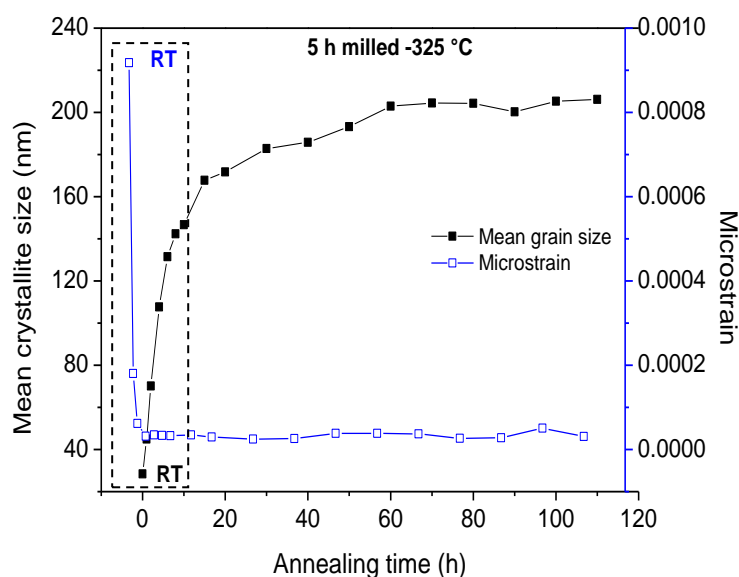


Figure 3.6: (a) Crystallite size and (b) microstrain evolution upon isothermal annealing of the 5 h milled specimen at 325 °C. The box indicates the region of rapid microstrain relaxation corresponding with fast initial grain growth.

At higher annealing temperatures a limiting ‘saturation value of’ crystallite size is reached and this saturation value of crystallite size increases with increasing annealing temperature. It can be expected that such saturation values of crystallite size also occur at the lower annealing temperatures (< 300 °C) upon prolonged annealing.

As compared to the 5 h milled specimen, a much higher temperature of 400 °C had to be applied to observe significant grain growth during a isothermal anneal of the 80 h milled specimen. Isothermal studies were thus conducted in the temperature range between 400 °C and 650 °C (Figure 3.7). At these temperatures, incessant linear growth occurred at each temperature. Remarkably, a ‘kink’ is observed in the growth kinetics at the stage where complete annihilation of microstrain has been realized (Figure 3.7c). The annealing at 500 °C was extended by about 700 h, and only revealed linear growth kinetics.

The microstrain, for both the 5 h milled specimen and the 80 h milled specimen, diminishes slowly at the lower annealing temperatures; the microstrain relaxation takes almost 50 h at 250 °C for the 5 h milled specimen and about 100 h at 400 °C for the 80 h milled specimen.

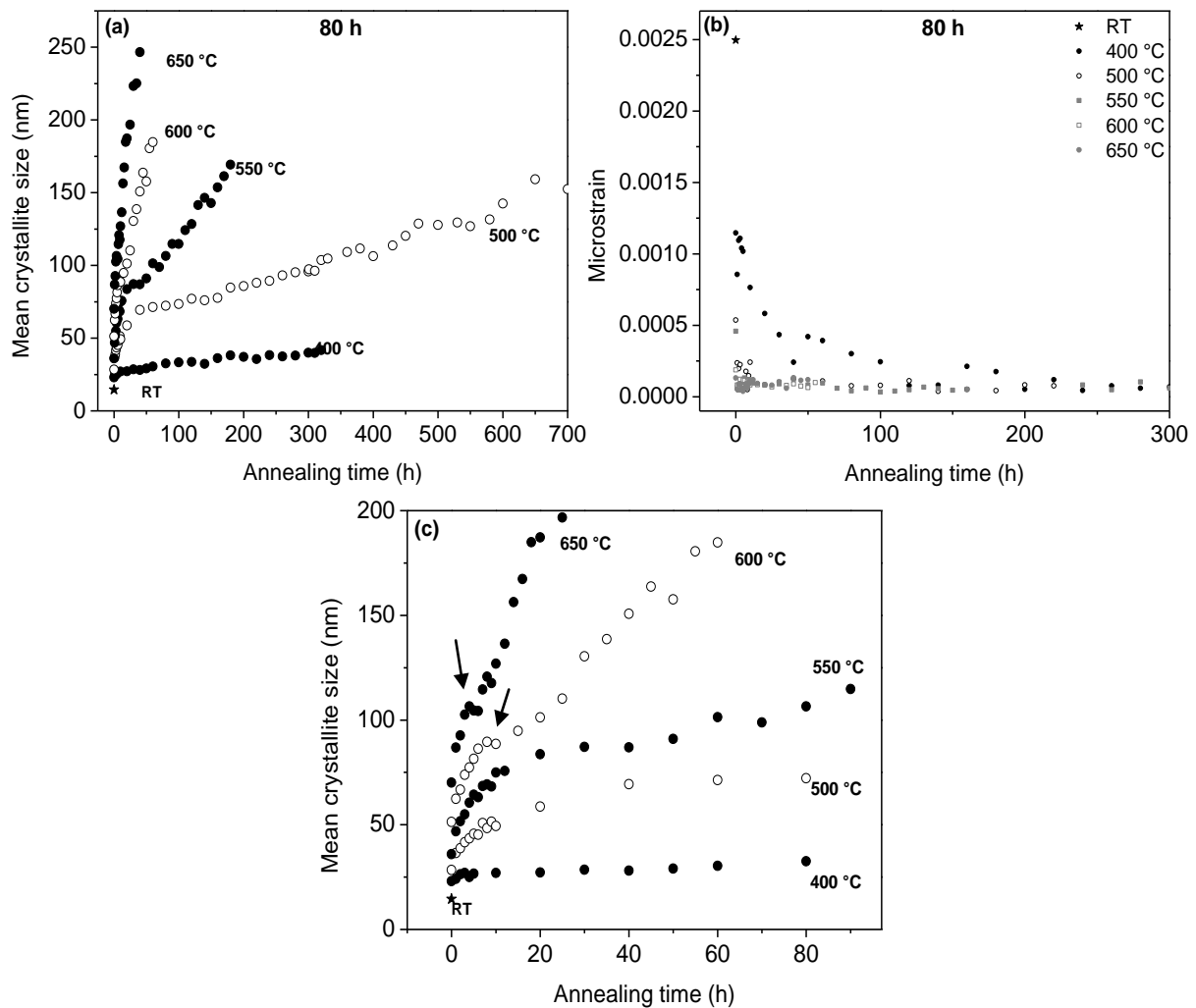


Figure 3.7: (a) Crystallite size and (b) microstrain evolutions as a function of time at various temperatures for the 80 h milled specimen. (c) Enlargement of (a) showing the 'kink' (marked with the arrows).

3.4.2.2 The grain-size distribution (GSD) upon annealing

The GSD has been evaluated for two selected specimens according to the WPPM and WA analyses: A specimen milled for 5 h was annealed at 300 °C for 7 h (this specimen will be referred as 5 h M-A in the following, M-A stands for milled-annealed). The 80 h milled specimen was annealed at 400 °C for 100 h (80 h M-A). After the annealing, both the specimens were rapidly cooled and X-ray diffraction measurements of the 111, 200, 222 and 400 Ni reflections were performed at ambient temperature. These specimens, according to the results obtained by adopting the single-line analysis, exhibit predominantly size broadening; the absence of strain broadening reduces possible errors associated with the size-strain separation (see discussion on size-distribution determination at the end of section 3.2.2.3).

The absence of strain was confirmed for the selected specimens for the 111-222 reflection pair by employing Eq. 3.10. In this case $A^d(L, S_i)$ was constant (=1) within experimental scatter. Hence only size broadening occurs. Hence W-A analysis is not required for the purely size broadened profiles. The Fourier coefficients were thus determined for all the reflections. The Fourier coefficients, $A^s(L)$, show ripples at higher L values (Figure 3.8), which makes a direct numerical calculation of the second derivative impossible: Therefore a polynomial fit was applied to the size Fourier coefficients (Figure 3.8). The area-weighted column-length distribution then obtained from the second derivative of the Fourier coefficients is shown in Figure 3.9 for two different reflections from both the specimens.

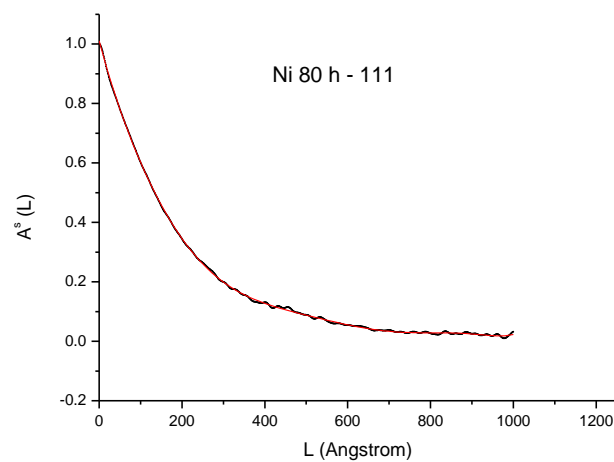


Figure 3.8: Fourier size coefficient, $A^s(L)$, of the 111 peak of the Ni 80 h M-A specimen. The smooth (red) line represents the polynomial fit of the profile.

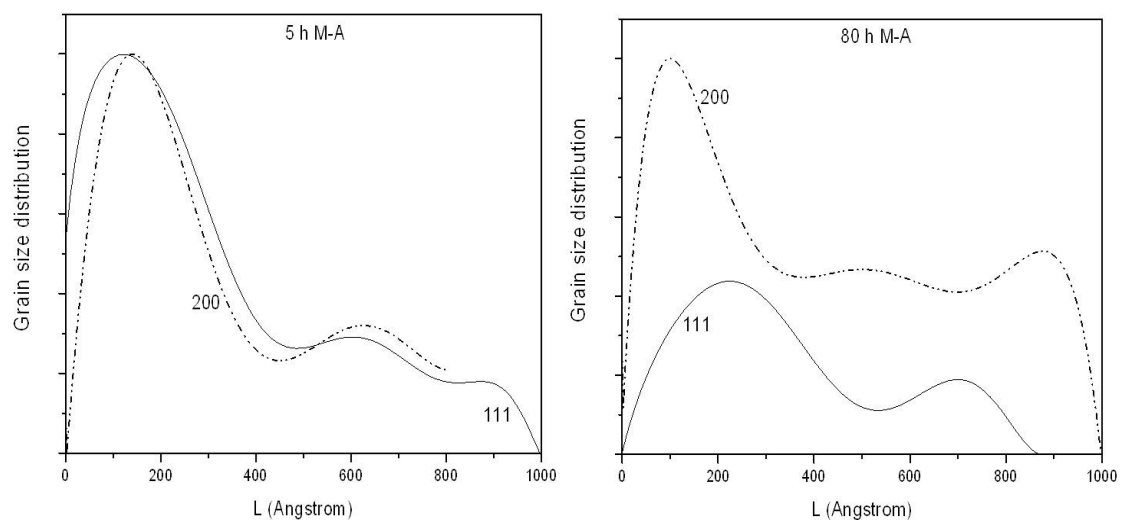


Figure 3.9: The area-weighted column length distributions obtained from the second derivative of the fitted size Fourier coefficients, $A^s(L)$, for the (a) 5 h M-A and (b) 80 h M-A specimens.

In the 5 h M-A specimen, a more or less bimodal distribution prevails. The close correlation of the size distributions derived from the 111 and 200 profiles suggests validity of the analysis. The similar results for the size distributions obtained from the 111 and 200 profiles of the 80 h M-A specimen agree less well: the size distribution obtained from the 111 reflection exhibits distinct bimodality, whereas the size distribution obtained from the 200 reflection can better be described as having a pronounced tail towards larger sizes.

The same reflections were also analyzed employing the WPPM method. However, a good fit was only possible for the 80 h M-A specimens (the result is shown in Figure 3.10). The crystallite size distribution of the 80 h milled specimen changed from a narrow to a broader size distribution upon annealing along with a small increase in the average crystallite size.

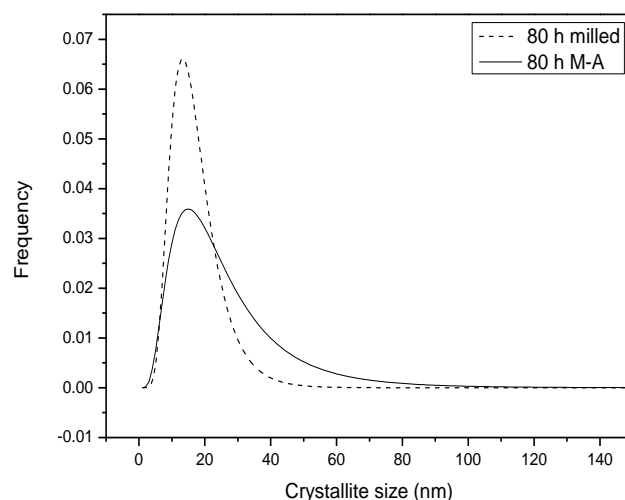


Figure 3.10: Comparison of the crystallite-size distributions obtained by WPPM before annealing (dashed line) and after annealing the 80 h milled specimens for 100 h at 400 °C.

The average crystallite/grain sizes (SLA: volume-weighted, W-A: area-weighted, WPPM: average - crystallite sizes), under the assumption of a spherical grain morphology, obtained by the different methods of analysis adopted in this work are gathered in the Table 3.2.

From the above results (Figure 3.9, Figure 3.10 and Table 3.2) it is concluded that the 5 h M-A specimen has a bimodal distribution of grain sizes while the 80 h M-A specimen has a very wide distribution. It is also observed that the SLA provides fair average crystallite-size values even if the specimen profile contribution to the overall peak broadening is small (5 h M-A specimen), and also if size distribution is not monomodal.

Table 3.2: Comparison of the grain size data obtained by different methods. (for WPPM of 5h M-A specimen – no reliable analysis is possible)

Sample	Crystallite size (nm)		
	SLA	WPPM	WA
5 h M-A (Bimodal distribution)	83	-	50 (111)
			40 (200)
80 h M-A (Multi/wide distribution)	38	26 (5)	30 (111)
			24 (200)

The grain-size distributions as developed after annealing show a dependency on the size distribution as present in the as-milled specimens. The size distribution of the 5 h milled specimen is wider than that of the specimen milled for 80 h (see Figure 3.3). Nanocrystalline materials of uniform microstructure (as exhibited by an equi-axed grain morphology and a narrow size distribution and a homogeneous microstrain; cf. section 3.4.1) are expected to possess a higher thermal stability than nanocrystalline materials of inhomogeneous microstructure [66]. Therefore, the 80 h milled specimen shows less pronounced grain growth than the 5 h milled specimen (e.g. see Table 3.2).

3.4.2.3 Grain-growth kinetics

The grain-growth kinetics in both the 80 h and 5 h milled, specimens were analysed by fitting the crystallite-size data obtained in the *in-situ* investigations by applying the single-line method (c.f. section 3.4.2.1; Figure 3.5 - Figure 3.7) adopting several grain-growth models (c.f. section 3.2.1). The corresponding model fits are shown in Figure 3.11 and Figure 3.12 for the 5 h and 80 h milled specimens, respectively. The three models considered do not provide overall satisfactory fits to the experimentally observed grain-growth kinetics:

- The *generalized parabolic grain-growth* model does not provide reasonable fits for the isothermal data for either of the samples. Improved fits were obtained by varying the growth exponent n with annealing temperature (results not shown). However, even with this additional fit parameter, the fits were still imperfect. Moreover, a drastic change of the value for the rate constant with change of temperature occurred which implies an unrealistic value for the activation energy of the grain boundary mobility.
- The *grain-growth model with impediment* shows a good fit only for the 5 h milled specimen at lower temperatures yielding (from the rate constant) activation energy

of about 115 kJ/mol. The model with *size-dependent impediment* exhibits, for the same specimen, a reasonable fitting only at higher temperatures yielding activation energy of the grain boundary mobility of about 148 kJ/mol. The *grain-growth model with impediment* applied to the data obtained for the 80 h milled specimen provides better fits at longer annealing times yielding an activation energy of the grain boundary mobility of about 108 kJ/mol. The grain growth model with *size dependent impediment* shows acceptable fits, for the 80 h milled specimens, only at higher temperatures yielding a value of the activation energy for grain boundary mobility of about 95 kJ/mol. All the models in general fit less well to the data of the 80 h milled specimen than those of the 5 h milled specimen.

- A common feature of all the fits for all three models is that, in particular, for the 80 h milled specimen, the fit is poor for the initial stage of annealing (the *rapid grain growth* region, cf. Figure 3.6).

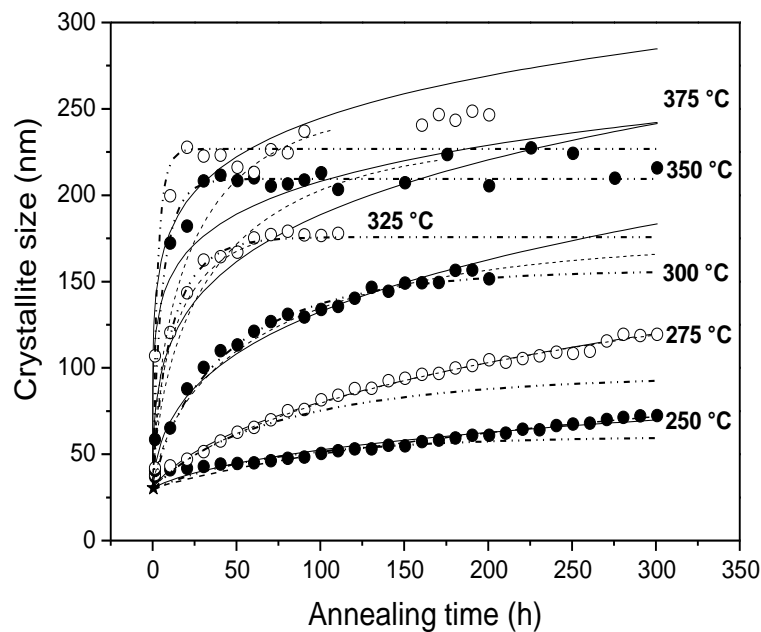


Figure 3.11: Fits of grain-growth models to the isothermal annealing data for the 5 h milled specimens. Full line: generalized parabolic grain-growth model; dashed line: grain-growth model with impediment; dash-dot : grain-growth model with size-dependent impediment.

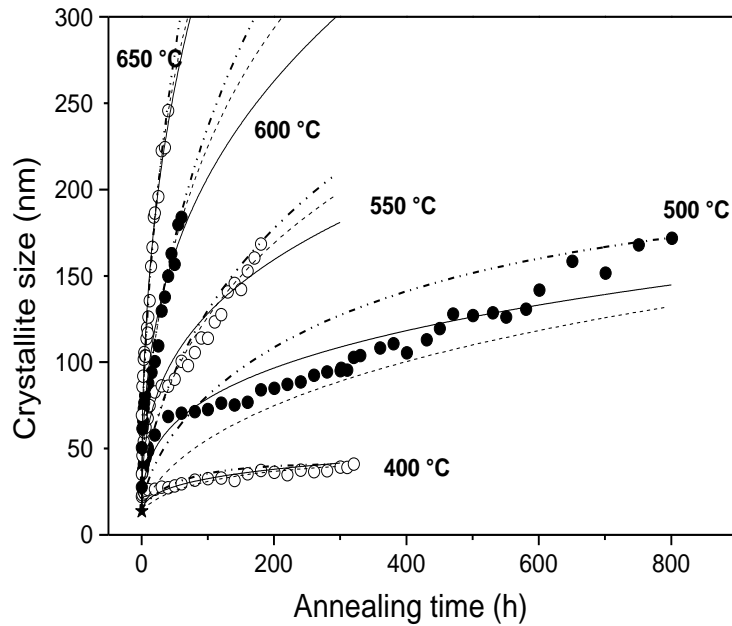


Figure 3.12: Fits of grain-growth models to the isothermal annealing data for the 80 h milled specimens. Full line: generalized parabolic grain-growth model; dashed line: grain-growth model with impediment; dash-dot : grain-growth model with size-dependent impediment.

The initial stage of grain growth can be divided into two regimes: first the initial rapid grain growth accompanying the microstrain relaxation (cf. Figure 3.6 and section 3.4.2.2) and second the almost linear grain growth which follows this regime.

The faster initial rapid grain growth in the 5 h milled specimen as compared to the 80 h milled specimen has been attributed to the higher thermal stability of the material possessing a narrow initial grain size distribution (here 80 h milled specimen) as compared to the material with a broader initial grain size distribution (5 h milled specimen) (cf. section 3.4.2.2).

In view of the discussion on the grain-growth models in section 3.2.1, and considering the above discussed imperfect fitting of the non-linear kinetics, the apparently linear grain growth regime that follows this rapid initial grain growth in both the specimens cannot be ascribed to grain boundary curvature driven kinetics. The effect may be a consequence of the presence of excess volume at the grain boundaries (cf. section 3.2.1) and hence the excess free volume model (Eq. 3.5) was applied. The initial linear grain-growth stage is shown in Figure 3.13a and Figure 3.14a, respectively for the 5 h and 80 h milled specimens. This initial growth rate is proportional to $T^{-1} \exp(-Q/k_B T)$ with Q as the activation energy for volume diffusion. Hence, the activation energy for D_{SD} (cf. Eq. 5) was

derived from the slope of an Arrhenius-type plot (see Figure 3.13b and Figure 3.14b for the Arrhenius plots for the 5 h and 80 h annealed specimens) yielding 158 kJ/mol and 100 kJ/mol for the 5 h and 80 h milled specimens, respectively. The excess volume per unit area of grain boundary, $\Delta V/A$, determined from the fit of the Eq. 3.5 and the Figure 3.13b and Figure 3.14b respectively, for the 5 h and 80 h milled specimens are $2 \cdot 10^{-5}$ nm and 0.0196 nm, respectively.

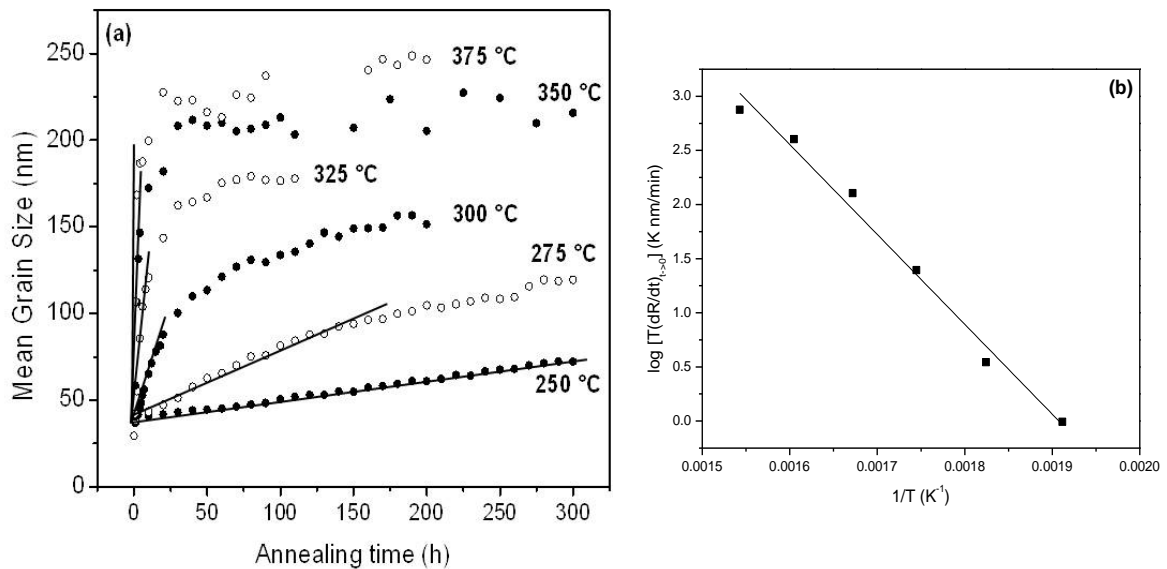


Figure 3.13: (a) Linear fits for the stage of linear grain growth in Ni 5 h specimens according to the Eq.3.5. (b) Arrhenius plot for the initial growth rate yielding activation energy of 158 kJ/mol and leading to an excess free volume of $2 \cdot 10^{-5}$ nm.

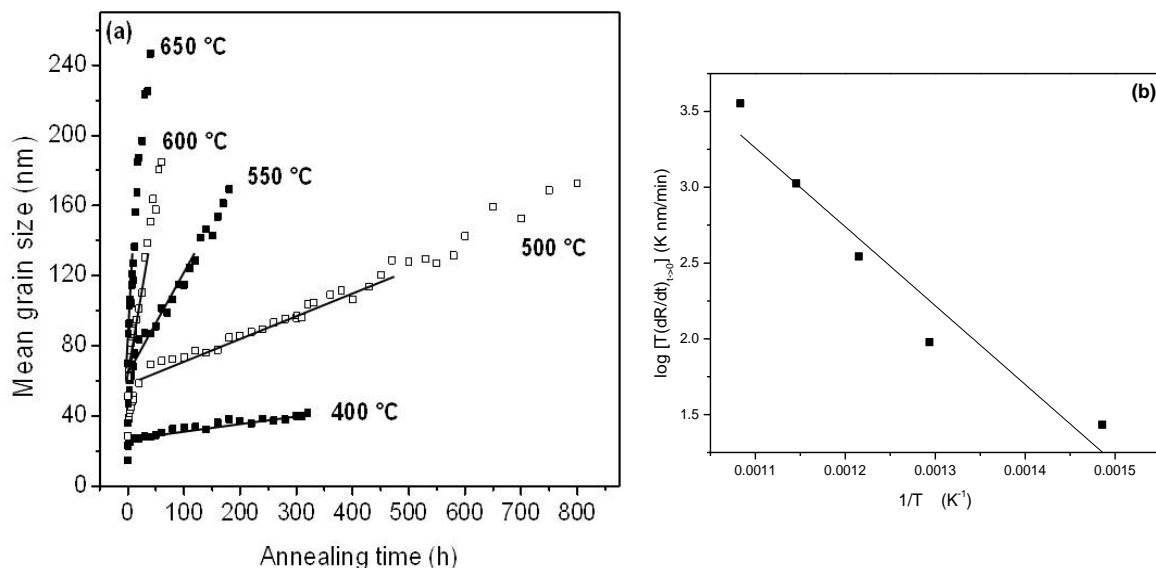


Figure 3.14: (a) Linear fits for the initial stage of grain growth in Ni 80 h specimens according to the Eq. 3.5. (b) Arrhenius plot for the initial growth rate yielding activation energy of 100 kJ/mol and leading to an excess free volume of 0.0196 nm.

The activation energies (for D_{SD}) obtained by this model are close to that for the grain-boundary self-diffusion (the literature value for the activation energy for grain boundary self-diffusion of Ni is 115-150 kJ/mol; the literature value for the activation energy for volume diffusion in Ni is ~270 kJ/mol [188]). However, according to the model (see Eq. 5), D_{SD} represents volume diffusion.¹ Hence, the excess free volume model (Eq. 3.5), which explains the linear growth kinetics on the basis of production and injection of vacancies into the bulk of the grains, cannot explain the observed kinetics. The low values for the activation energies for the stage of linear grain growth can be explained as a consequence of enhanced grain-boundary mobilities due to the presence of excess free volume remaining after the first stage of very fast grain growth [190]. Then the low value of the activation energy of the 80 h milled specimen thus is a simple consequence of the more deformed and finer nanocrystalline nature of this specimen implying a larger amount of excess free volume in its grain boundaries.

Finally, the present work has led to the following model description of grain growth in nanocrystalline materials: The very fast initial grain growth, that accompanies practically full microstrain relaxation, is caused by the high mobility of the grain boundaries of the nanocrystalline material due to the initial presence of a very large amount of excess free volume. The subsequent stage of linear grain growth is characterized by a relatively low value for the activation energy due to remaining excess free volume at the grain boundaries. This activation energy is smaller for the more deformed, finer nanocrystalline material as more excess free volume has been generated.

Yet, the finer nanocrystalline material exhibits distinct grain growth at a higher temperature than the coarser nanocrystalline material. This can be understood as a consequence of a much wider grain-size distribution for the coarser and thus suggests 'abnormal grain growth' [164, 175].

¹ In a previous study on ball milled Fe powders [70] the experimentally observed activation energy was found to be close to the activation energy for volume diffusion. Recently, the first author of Ref. [70] has now attributed the stage of linear grain growth in nanocrystalline Fe to triple junction controlled kinetics [79]. However, a recent study [189] has shown that triple junction controlled growth kinetics is important in Ni only up to maximally 300 K and below and hence triple junction limited grain growth can be neglected in the present study.

3.5 Conclusion

- 1) Ball milling of Ni powder leads to a decrease of grain size, down to a saturation level of 18 nm, a continuous increase of microstrain (dislocation density) and a continuous increase of the stacking fault probability. The grain-size distribution can be described with a lognormal distribution. Upon continued ball milling the grain-size distribution becomes very narrow.
- 2) Upon heating the nanocrystalline Ni powders, distinct grain-growth occurs after the microstrain has relaxed practically completely. The nanocrystalline material of wide grain-size distribution exhibits pronounced grain growth already at lower temperature than the nanocrystalline material of narrow grain-size distribution.
- 3) Upon isothermal annealing of the nanocrystalline Ni powders, a first stage of very fast linear grain growth, in association with practically complete release of the microstrain, is followed by a stage of more or less linear grain growth. In case of an initially wide grain-size distribution, grain growth occurs much faster and eventually a saturation value of grain size is reached that depends on the temperature (i.e. it increases with temperature). The developing grain-size distributions become of bimodal nature in case of an initially wide size distribution and exhibit pronounced broadening with a distinct tail to larger size values in case of an initially narrow size distribution.
- 4) Grain-growth models based on grain boundary curvature driven grain growth cannot describe the observed grain-growth kinetics.
- 5) Adopting linear growth, fitting of a corresponding model based on the injection of vacancies, originating from the excess free volume in the grain boundaries of the nanocrystalline material, in to the bulk of the grains, is possible, but leads to physically unrealistic values for the activation energy of volume self-diffusion.
- 6) The activation-energy values derived from the growth-rate constants for linear growth are in the range of 100 kJ/mol (for the nanocrystalline Ni of initially 18 nm grain size and narrow grain size distribution) to 158 kJ/mol (for the nanocrystalline Ni of initially 35-38 nm grain-size and a broad grain-size distribution).
- 7) The very first stage of very fast growth (see above conclusions 2 and 3), preceding the linear growth stage, is ascribed to a high mobility of the initially unrelaxed grain boundaries of the nanocrystalline material which initially contain a high amount of excess free volume. This amount of excess free volume in the grain boundaries is

likely larger for the finer grained (ball milled for a longer time) nanocrystalline material, which is compatible with the significantly lower value of the activation energy for the subsequent stage of linear grain growth in the finer nanocrystalline material as compared to the coarser nanocrystalline material (cf. conclusion 6).

- 8) The observation that the finer nanocrystalline material of much narrower size distribution has the lower activation energy of grain growth and yet exhibits pronounced grain growth at temperatures higher than the coarser nanocrystalline material of wider size distribution is ascribed to so-called 'abnormal grain growth' as the prevailing grain-growth mechanism.

Chapter 4

The microstructural evolution and thermal stability of nanocrystalline, ball milled Ni- 15 at. % W powder

G. K. Rane, D. Apel, U. Welzel, E. J. Mittemeijer

Abstract

A mixture of pure Ni powder and pure W powder with a nominal composition Ni - 15 at. % W was subjected to ball milling in a planetary mill and in a shaker mill. The microstructural evolution upon milling and subsequent annealing in the temperature range from 25 °C to 800 °C was investigated employing ex-situ and in-situ X-ray diffraction integral breadth (single-line and Williamson-Hall) methods and whole powder pattern modelling as well as scanning electron microscopy, transmission electron microscopy and differential scanning calorimetry. A nanocrystalline Ni(W) solid solution develops upon ball milling, with a higher W content by milling in the shaker mill as compared to the planetary mill. Grain coarsening studies indicated a very high stability of the nanocrystalline state, up to almost about 500 °C. Results of annealing at higher temperatures, while increasing the dissolved W content in the Ni matrix suggests that the high stability against grain coarsening could be due to modification of the grain boundary energy by segregating W atoms and/or the low mobility of the W atoms, i.e. a combined thermodynamic and kinetic barrier.

4.1 Introduction:

Nanocrystalline materials constitute a focal point of interest for fundamental scientific as well as applied research as such materials have a variety of applications in view of their properties which are often superior to the properties of coarse-grained materials [19, 65]. Examples of such properties are higher strength and hardness [191, 192], extreme ductility without strain hardening [9], hard magnetic properties [193], etc. Mechanical attrition provides a simple but efficacious method for producing large batches of nanocrystalline material exhibiting far-from-equilibrium microstructures and phases with tunable compositions produced by mechanical alloying. In addition, the grain size can be tailored by varying the milling time and/or the milling parameters [159, 194, 195].

Such nanocrystalline material (grain size < 100 nm) exhibits a high driving force for grain coarsening due to the high density of grain boundaries [194, 196]. The onset of grain coarsening for nanocrystalline materials can thus occur at distinctly lower homologous temperatures (even close to ambient temperature: “self annealing”) than for the corresponding coarse-grained materials [197, 198]. The grain-boundary velocity during grain growth is proportional to the driving force and the grain-boundary mobility. Thus, two approaches for suppressing grain growth in order to preserve the microstructure of nanocrystalline materials upon aging or application of some time-temperature program can be adopted:

- (i) The thermodynamic approach (e.g. [87, 194, 199-201]): The driving force, i.e. the grain-boundary energy, can be reduced by alloying. Specifically, grain-boundary segregation has been proposed as a mechanism for lowering the excess energy contained in grain boundaries.
- (ii) The kinetic approach (e.g. [84, 202]): Solute atoms or precipitates impose drag forces on the interface motion.

Though independent, under practical circumstances and depending on the system, both mechanisms might be operative simultaneously.

Nickel-tungsten (Ni-W) alloys with a high W content have found wide-ranging applications where high density, tensile strength and durability are required while combining with the useful magnetic properties of Ni [88]. Incorporation of W into Ni improves its mechanical properties by solid-solution strengthening. Combined with its high temperature resistance, this material is a good candidate for corrosion resistant material in high-temperature applications [89] (and in this context, is a good replacement for the

environmentally hazardous hexavalent chromium [90]); it exhibits great potential for use as substrates for high-temperature superconductor applications [203, 204]. Such substrates need to be mechanically strong and also should possess high cube texture with high surface quality. However, addition of W improves the mechanical property and reduces the unwanted ferromagnetism of Ni, it adversely affects the development of texture (due to the decreased stacking fault energy of Ni upon adding W) [205]. High energy ball milled Ni-W alloys resulted in more than 90% cube texture component upon their processing into substrates [206]. Powder metallurgical approach towards production of such material has thus gained momentum recently and could prove to be a promising alternative to the traditional melting-casting route [207, 208]. In addition, in nanomaterials where the classical scaling laws break down, control of the microstructure is extremely important. In recent years, research has been performed on nanocrystalline Ni-W system synthesized by electrodeposition [196, 209-212], sputtering [213] and ball milling [214-216]. Yet, knowledge and understanding of the properties of nanocrystalline Ni-W alloys is still in its infancy [217, 218].

The present work describes the microstructural evolution upon ball milling pure Ni powder and of a mixture of Ni powder and W powder with a nominal composition Ni - 15 at. % W. In order to study the microstructural developments, X-ray diffraction (XRD) has proved to be a powerful non-destructive tool and is used extensively in extracting the microstructural information of nanocrystalline samples [94]. XRD is often the most (also and in particular statistically) reliable tool at hand when studying bulk specimens. From the peak parameters such as peak width, position, shape and intensity of the diffraction lines information regarding the distribution of phases, crystallite size and shape distribution, concentration and distribution of crystal defects such as dislocations, faults, twins etc. can be determined [95, 96]. In this work, the evolution of the grain size and the microstrain was studied using X-ray diffraction analysis employing integral breadth (single-line and Williamson-Hall) methods [95] and the more recent method of whole powder pattern modelling (WPPM) [219]. Further, the evolution of the microstructure of the Ni(W) solid solution as produced by ball milling, was traced upon annealing, in particular, the grain-coarsening behaviour was investigated using in-situ XRD measurements in the temperature range between 25 °C and 850 °C. Preliminary results have been presented in ref. [215].

4.2 Theoretical background: X-ray diffraction line-profile analysis

4.2.1 Integral-breadth methods:

4.2.1.1 Single-line method

It is assumed that the specimen profile f can be described by a Voigt profile, which is a convolution of a Gaussian and a Lorentzian profile, where the Gaussian component of the profile is due to the microstrain ε and the Lorentzian component of the profile is due to the finite crystallite size [96, 154]. The integral breadths β_C^f and β_G^f of the Lorentzian (Cauchy) and Gaussian components, respectively, can be related to the volume-weighted column length L and the microstrain ε :

$$\beta_C^f = \frac{\lambda}{L \cos \theta} \quad (4.1)$$

$$\beta_G^f = 4 \varepsilon \tan \theta \quad (4.2)$$

where λ is the wavelength and θ is the Bragg angle.

The crystallite size (diameter) D can be calculated from the volume-weighted column length L if an assumption for the crystallite shape is adopted [177]. In this work, a spherical crystallite shape has been assumed, hence $L = 3D/4$.

The measured profile h is a convolution of the specimen profile f and the instrumental profile g . If it is assumed that the instrumental profile g and the measured profile h can also be represented by Voigt functions, a simple correction for instrumental diffraction line broadening on the basis of the integral breadths and Voigt parameters of the measured and instrumentally broadened line profiles is possible as well [96] by subtracting the instrumental Lorentzian and Gaussian integral breadths of the instrumental profile from the Lorentzian and Gaussian integral breadths of the measured profile linear and quadratically, respectively.

4.2.1.2 Williamson-Hall (WH) method [97]

Under the assumption that the integral breadths pertaining to the size- and the strain-broadened profiles are linearly additive, it follows that:

$$\beta^f = \frac{\lambda}{L \cos \theta} + 4\varepsilon \tan \theta \quad (4.3)$$

Converting to reciprocal space pendants of β and d , β^* and d^* , respectively, using $\beta^* = \beta \cos \theta / \lambda$ and $d^* = 2 \sin \theta / \lambda$, gives

$$(\beta^f)^* = \frac{1}{L} + 2 \varepsilon d^* \quad (4.4)$$

Hence a plot of $(\beta^f)^*$ vs d^* should result in a straight line and then the values for grain size and strain can be obtained from the intercept and the slope. In this work the Voigt-subtraction of the instrumental profile was adopted (a total integral breadth of the specimen profile was obtained from the Gaussian and Lorentzian integral breadths of the specimen profile).

The WH method in principle implies a uniform microstrain in all crystallographic directions and hence is questionable when applied to elastically anisotropic materials. A model taking the elastic anisotropy into consideration has also been used in this work and is briefly described below.

The uniform deformation stress (uds) model leads to an anisotropic microstrain state ε_{hkl} (with the stress independent of the orientation of the direction in the crystallites) [220, 221]. This anisotropic microstrain ε_{hkl} can be related to the uniform stress σ via Hook's law: $\sigma = \varepsilon_{hkl} \cdot E_{hkl}$ where E_{hkl} is the Young's modulus in the direction perpendicular to the hkl lattice plane, then, ε in Eq. 3 has to be replaced by ε_{hkl} .

$$\frac{\beta \cos \theta}{\lambda} = \frac{1}{L} + \frac{2\sigma d^*}{E_{hkl}} \quad (4.5)$$

4.2.2 Whole powder pattern modelling [94, 103, 178, 179]

In the whole powder pattern modelling (WPPM) method a diffraction pattern is synthesized directly from physical models describing the microstructure of the material under study and the model parameters are then fitted to the measured data, thus overcoming the possible bias which is introduced by integral breadth methods due to the arbitrariness of using analytical profile functions (cf. section 4.2.1). The method has been successfully applied in several cases; recent applications have been summarized in Ref. [180]. The basic theory is briefly described here. The diffraction profile can be written as

$$I_{(hkl)}(d^*, d_{(hkl)}^*) = k(d^*) \sum_{hkl} w_{hkl} \int_{-\infty}^{\infty} \mathbb{C}_{hkl}(L) \exp[2\pi i L(d^* - d_{(hkl)}^* - \delta_{hkl})] dL \quad (4.7)$$

where $d_{(hkl)}^*$ is the value of the reciprocal space variable d^* in the Bragg position and $k(d^*)$ includes constants and known functions of d^* . w_{hkl} and δ_{hkl} are, respectively, the weight of a reflection (related to its multiplicity) and the shift of a reflection from the exact Bragg position for an (hkl) member of the $\{hkl\}$ s family of crystallographic planes. The last parameter is related to lattice defects, like faulting, which, in addition to a profile broadening, cause different shifts of the various (hkl) subcomponents. As a consequence, the observed peak profile is expressed as a weighted sum of all the different subcomponents. The Fourier transform $\mathbb{C}_{hkl}(L)$ includes all the instrumental and specimen related effects

such as the instrumental profile, domain size, faulting, dislocations, antiphase domain boundaries all of which are described by physical models.

In the present work, the XRD patterns were modelled by using PM2K [222], a software based on the WPPM approach that allows refinement of the data by non-linear least squares routine. The instrumental component is handled by a pseudo – Voigt fit of a suitable line profile standard (eg. LaB₆ NIST SRM660a). The background described with Chebyshev polynomial (of degree 3), peak intensities, specimen displacement, lattice parameter of Ni and W were refined simultaneously for each pattern. The specimen-related physical broadening parameters to be determined by the fitting were the mean (μ) and variance (σ) of a lognormal size distribution adopted for the spherical crystallites, the dislocation density (ρ) and the effective outer cut-off radius for both Ni and W. Additional, the faulting parameters α (deformation) and β (twin) were included for Ni, which has an fcc crystal structure. The average contrast factors for edge and screw dislocations were calculated for the $\langle 110 \rangle \{111\}$ slip system with Burgers vector $a_0/(2^{1/2})$ for Ni and $\langle 111 \rangle \{110\}$ slip system with Burgers vector $a_0*(3^{1/2}/2)$ for W.

4.3 Experimental procedures

4.3.1 Ball milling

Ball milling was carried out at room temperature in a planetary ball mill (Fritsch Pulverisette P6) and in a high energy shaker mill (Spex 800M). Elemental powders of Ni having a purity of 99.8 wt.% and a particle size smaller than 50 μm (≤ 300 mesh) and of W having a purity of 99.95 wt.% and a particle size of 44-77 μm (≤ 200 mesh) were mixed to achieve a composition of 15 at.% W (both powders from Alfa Aesar GmbH & Co KG, Karlsruhe, Germany). The powder mixtures were milled in WC-Co vessels (93.8 wt.% WC, 6 wt.% Co) with WC-Co milling balls (10 mm in diameter) of the same purity maintaining a ball to powder ratio of 10:1. All powders were handled under Ar atmosphere while filling the milling vessel to avoid contamination with impurities. The rotation speed of the planetary mill was maintained at 150 rpm.

4.3.2 X-ray diffraction measurements

The materials under study have been characterized using a Bruker AXS D8 Advance θ - θ diffractometer operating in Bragg-Brentano geometry using Cu-K α radiation. The diffractometer is equipped with a Cu X-ray tube and a Ni absorption edge filter (to remove

Cu- $K\beta$ radiation) positioned in front of the 1D position-sensitive VANTEC-1 detector (Bruker AXS). The X-ray tube is operated at a tube voltage of 40 kV and a tube current of 40 mA. An ‘infinitely thick’ sample with a flat surface was prepared by gently pressing the sample into the sample holder cavity. The XRD patterns of the ball milled powder samples were recorded in the range of $2\theta = 30^\circ - 140^\circ$ (comprising the Ni 111, 200, 220, 311, 222, 400 reflections and the W 110, 200, 211, 220, 310, 222 and 321 reflections) using a 0.25° divergence slit and a 0.5° antiscatter slit.

Heating experiments were conducted under N_2-H_2 atmosphere (98 % N_2 - 2 % H_2) with a gas flow of 0.7 l/min, in an Anton Paar HTK 1200N oven chamber in the temperature range of $300^\circ C$ to $850^\circ C$. A heating rate of $0.5^\circ C/s$ was used to reach each temperature. During the heat treatment, *in-situ* X-ray diffraction measurements were performed. The 2θ scan range was divided into three ranges to optimize the measurement conditions for minimal measurement time (the time per step was selected so that a peak maximum intensity of at least 2000 counts was achieved) and reduce the measurement time. The entire measurement (comprising all three 2θ -ranges) took about 1 h. The measured diffraction patterns were analyzed either by fitting pseudo-Voigt functions with the α_2/α_1 ratio set to 0.5 (for Williamson-Hall and single-line analysis; see below) or by whole powder pattern modelling. The instrumental broadening was characterized by measuring a LaB_6 powder specimen (NIST Standard Reference Material 660a).

4.3.3 Scanning and transmission electron microscopy

The microstructure and morphology of the powder particles after various milling times were characterized by scanning electron microscopy (SEM). A JEOL 6300F microscope was used and operated in secondary-electron imaging mode (SE) at acceleration voltages between 3-5 kV depending on the specimen. For each specimen, a small amount of powder was embedded in Polyfast, ground and then polished.

Transmission electron microscopy was performed on the ball milled and annealed specimens. The electron transparent foils for TEM were prepared employing a focused ion beam (FIB) Nova Nanolab 600 workstation by the lift-out technique. To this end, first a protective Pt layer was deposited covering the surface of a selected powder particle to prevent Ga^+ damage in the region of interest during the following cutting and thinning process. Then, applying a focusing Ga^+ ion beam operating at 30 KeV, a thin slice of the Ni powder particle was cut and ion-beam cleaned. This slice of the powder particle was picked thereafter using a micro-manipulator and then welded onto a Cu grid for TEM examination.

Finally, this sample was thinned to electron transparency using low Ga^+ ion currents of 10-30 pA. The TEM investigation was performed on a Philips CM200 transmission electron microscope operated with a 200 kV electron beam.

4.3.4 Differential Scanning Calorimetry

Calorimetric experiments were conducted in a Perkin Elmer Pyris 1 differential scanning calorimeter (DSC) (under high-purity argon gas flowing at a rate of 20 ml/min) using approximately 60 mg of powder. The temperature and the heat flow were calibrated by measuring the melting temperatures and the heats of fusion of pure In, Sn and Zn. The samples were first heated to 80 °C at a heating rate of 10 °C/min followed by an isothermal hold for 300 min at 80 °C. The specimens were then heated to 340 °C at a heating rate of 20 °C/min. After reaching 340 °C the specimens were cooled to 50 °C at a cooling rate of 20 °C/min followed by an isothermal hold for 10 min at 50 °C.

4.4 Results and discussions

4.4.1 Microstructural evolution upon milling

4.4.1.1 Scanning electron microscopy investigations of the milled powders

SEM micrographs of the powders milled in the planetary mill and the shaker mill are shown in Figure 4.1 and Figure 4.2, respectively. The bright grey phase is W and the dark grey phase is Ni. The SEM micrograph in Figure 4.1a shows that, after milling for 5 h in the planetary mill, the W and Ni particles have been welded together but that the locations of the two elements are still distinctly separated. After 80 h milling (Figure 4.1b), the microstructure has undergone substantial changes and consists of lamellae of the more brittle W embedded inside the more ductile Ni. Thereby a significant increase of the contact area of W and Ni has been realized.

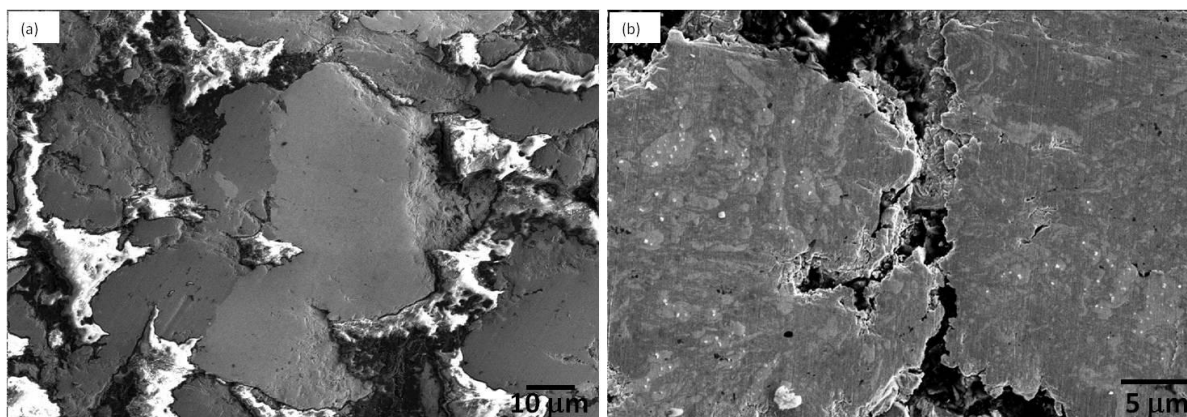


Figure 4.1: SEM (SE) micrograph of powder particles on milling Ni – 15at.% W powder mixture in the planetary mill for (a) 5 h and (b) 80 h. Bright grey phase: W-rich phase, Dark grey phase: Ni-rich phase.

However, it is seen that a similar lamellar structure is obtained for powder prepared in the shaker mill already after 5 h of milling (Figure 4.2a). Further milling (Figure 4.2b; milling for 30 h) has led to the formation of a very fine dispersion of W particles in the Ni matrix; a separate W phase can hardly be distinguished.

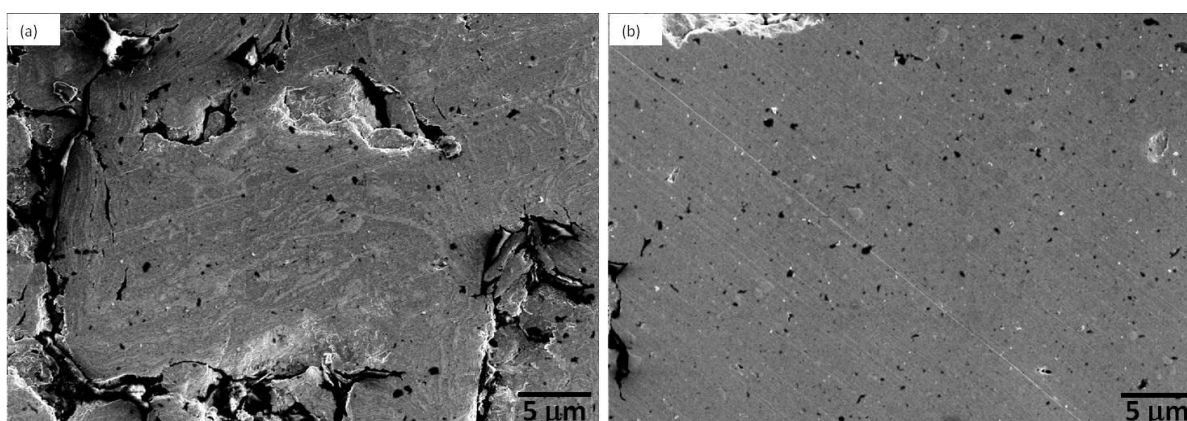


Figure 4.2: SEM (SE) micrograph of powder particles on milling Ni – 15at.% W powder mixture in the shaker mill for (a) 5 h and (b) 30 h. Bright grey phase: W-rich phase, Dark grey phase: Ni-rich phase. The different phases are indistinguishable in (b); (the black phase belongs to the embedding material).

4.4.1.2 X-ray diffraction survey scans; W dissolution in Ni

Sections of the diffraction patterns of the initial powder mixtures (Ni-15 at. % W) and the powders milled for the longest milling times in the shaker and planetary mills are shown in Figure 4.3. Both, the W 110 and the Ni 111 and 200 diffraction lines broaden considerably upon ball milling due to the reduction of the size of the diffracting crystallites and an increase in microstrain (see section 4.4.1.3).

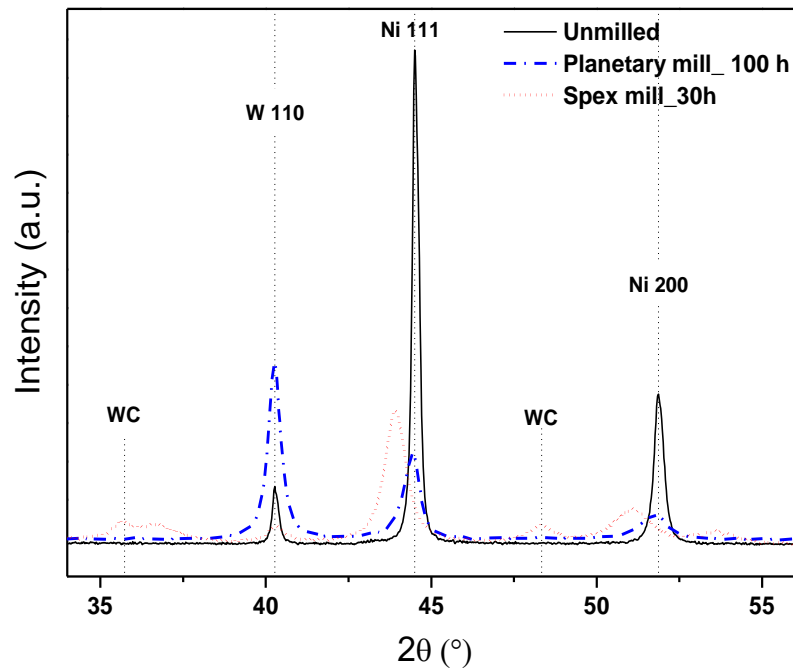


Figure 4.3: X-ray diffractograms of Ni – 15 at. % W powder mixture milled in planetary mill and shaker mill for the longest milled specimens.

A shift of the Ni peaks to lower angles is ascribed to the dissolution of W in Ni (i.e. the lattice constant of Ni is increased upon W dissolution), which is much more pronounced for the powder milled employing the shaker mill despite the much shorter milling time. The W concentration in Ni can be calculated from the peak shift using lattice-parameter data for the Ni-rich Ni(W) solid solution from Ref. [213]. The obtained results have been gathered in Figure 4.4. The sample milled in the planetary mill shows initially small increase of the W content which stays practically constant up to 80 h of milling, followed by a major increase to about 2 at. % W after 100 h of milling. For the powders milled in the shaker mill, the W peaks have almost completely vanished after 30 h of milling and the peak positions of the Ni peaks have shifted pronouncedly to lower 2θ values thereby indicating almost complete dissolution of W into Ni. The composition of the alloy formed, as deduced from the line shifts, reveals that about 12 at. % of W has dissolved into Ni after 30 hours of milling. Thus, mechanical alloying in the shaker mill using WC milling balls results in the formation of a Ni(W) solid solution of roughly the alloy composition. On the contrary, no peak shift has been observed for the W reflections and thus no dissolution of Ni in W takes place, as expected according to the equilibrium phase diagram.

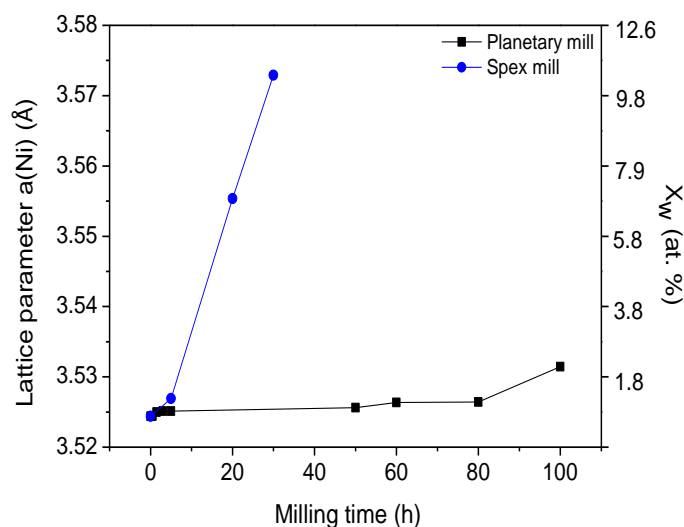


Figure 4.4: Lattice parameter variation of Ni in Ni – 15at. % W powder mixture milled in the planetary and shaker mills as a function of the milling time, also showing the composition of the solid solution finally formed.

Whereas the Ni (solid solution) peak maximum intensities decrease upon prolonged ball milling due to increasing peak broadening, the peak intensity of the W 110 diffraction line increases pronouncedly after 100 h of ball milling in the planetary mill, even though the peak broadening also increases significantly (i.e. the integrated intensity increases pronouncedly). A possible explanation for this striking behaviour could be the occurrence of pronounced extinction for the relative coarse-grained W powder in the early stages of ball milling; upon prolonged ball milling, the relevance of extinction vanishes due to an increase of the crystalline imperfection.

The powder milled in the shaker mill with WC milling balls is contaminated, as can be seen from the diffraction pattern showing WC peaks, which is due to the abrasion of the brittle milling balls in the high energy mill. The powders milled in the planetary mill do not show the presence of excessive impurities (according to chemical analysis by inductively coupled plasma optical emission spectroscopy, less than a total 1 wt. % of C, N, O was present in the longest milled specimens).

4.4.1.3 Line-broadening analysis

The results obtained by applying the different methods of line-broadening analysis (cf. section 4.2) have been gathered in tables 4.1 and 4.2 for powders milled in the planetary mill and shaker mill, respectively. The integral breadth methods yield the volume-weighted column length, from which the crystallite size (diameter) can be calculated assuming a spherical crystallite shape (cf. Section 4.2.1). The WPPM method yields the average

crystallite diameter under the assumption of a spherical crystallite shape and a lognormal size distribution.

According to the SLA and WPPM methods (cf. Table 4.1), after an initial rapid decrease of the average crystallite size of both Ni and W within the first 5 h of milling, the rate of reduction of crystallite size decreases and a saturation crystallite size of about ~ 15 nm for Ni and 16 nm for W according to SLA, 16 nm for Ni and 13 nm for W according to WPPM, is reached after 100 hours of milling in the planetary mill. Slightly smaller crystallite sizes are obtained according to the different methods for powders milled in the shaker mill: A saturation crystallite size of about ~ 9 nm for Ni and 33 nm for W according to SLA and 12 nm for Ni according to WPPM, is reached after 30 hours of milling. Analysis of the W peaks with WPPM was not possible for the longest milling time in the Shaker mill due to the too low intensity of the W diffraction lines (indeed, an unrealistically high grain size is obtained also in the SLA).

Table 4.1: Size-strain analysis results according to SLA, uds method and WPPM for Ni – 15at. % W milled in Planetary mill; (SLA, uds yield the Microstrain; WPPM yields the dislocation density in units of $10^{18}/m^2$)

Milling time t (h)	Ni						W					
	Grain Size (nm)			Microstrain (uds/SLA); Dislocation density (WPPM)			Grain Size (nm)			Microstrain (uds/SLA); Dislocation density (WPPM)		
	uds	SLA	WPPM	uds	SLA	WPPM	uds	SLA	WPPM	uds	SLA	WPPM
0	161	85	124	0.10	0.06	0.0001	217	136	110	0.03	0.01	0.0001
5	113	43	28	0.24	0.12	0.016	353	52	34	0.28	0.14	0.013
50	77	24	21	0.32	0.14	0.208	169	36	32	0.31	0.13	0.02
80	37	17	17	0.49	0.19	0.198	91	17	13	0.51	0.16	0.04
100	29	15	16	0.54	0.28	0.300	88	16	13	0.52	0.16	0.06

Table 4.2: Size-strain analysis results according to SLA, uds method and WPPM for Ni – 15 at. % W milled in Shaker mill; (SLA, uds yield the Microstrain; WPPM yields the dislocation density in units of $10^{18}/m^2$).

Milling time t (h)	Ni						W					
	Grain Size (nm)			Microstrain (uds/SLA); Dislocation density (WPPM)			Grain Size (nm)			Microstrain (uds/SLA); Dislocation density (WPPM)		
	uds	SLA	WPPM	uds	SLA	WPPM	uds	SLA	WPPM	uds	SLA	WPPM
0	161	85	124	0.10	0.06	0.0001	217	136	110	0.03	0.01	0.0001
5	28	13	10	0.54	0.25	0.16	61	14	7	0.51	0.12	0.02
20	19	8	8	0.9	0.34	0.39	26	17	6	0.36	0.28	0.003
30	25	9	12	0.77	0.32	2	19	33	-	0.02	0.54	-

The microstrain in Ni, according to SLA, increases continuously upon prolonged ball milling in the planetary mill. A similar trend for the dislocation density is revealed employing WPPM. The microstrain in W attains a more or less constant value according to SLA already after 5 h of ball milling in the planetary mill. Similarly, the dislocation density of W determined employing WPPM increases drastically after 5 hours of ball milling and thereafter exhibits an only moderate increase upon prolonged ball milling (except for the longest milling time).

W, having a very high melting point (3410 °C) and a high elastic modulus ($W = 411$ GPa, $Ni = 200$ GPa), upon plastic deformation behaves much different than the relatively soft FCC Ni. Plastic deformation in BCC metals is relatively difficult due to lesser number of available slip systems. In the case of W the grain-size reduction upon ball milling may not be due to plastic deformation alone (i.e. by dislocation motion and sub grain formation) but also due to fracturing of the brittle particles. Recognizing that grain-size reduction due to breaking of particles occurs by transgranular fracture makes the occurrence of grain-size reduction without pronounced increase of the microstrain/dislocation density, as observed for W, plausible. This interpretation is supported by the SEM micrographs showing a finely dispersed W phase in relatively large Ni grains on prolonged milling (cf. Figure 4.1b).

Milling in the high energy shaker mill resulted in the introduction of the same amount of microstrain in 5 h that took almost about 80 h of milling in the planetary mill (cf. Table 4.1 and Table 4.2).

The results of the SLA and WPPM methods provide qualitatively similar picture for the microstructural evolution. The uds-WH analysis tends to attribute the peak broadening to a larger extent to microstrain than to the crystallite size. Thus, by WH analyses, larger microstrain values and larger crystallite sizes are obtained, in particular for the W phase (cf. Table 4.1). This can be understood recognizing that the diffraction line shape of W changed from predominantly Lorentzian to Gaussian upon prolonged milling: As the Williamson-Hall analysis, as applied here, is based on a linear combination of measured and instrumental breadths and a linear combination of size- and strain-induced line broadening and thus presupposes Lorentzian line shape, the validity of the assumptions underlying the WH analysis become more and more questionable upon prolonged ball milling.

In addition to the mean crystallite size, the WPPM method also yields the width (variance) of the crystallite-size distribution, which helps in appreciating the effect of milling on the shape of the distribution. The as-received Ni powder (Figure 4.5a) shows an

asymmetric, broad size distribution; the size distribution for the as-received W powder is less broad and more symmetric (Figure 4.5b). In the early stages of milling (0 - 3 h) in the planetary mill, the crystallite-size distribution for Ni (Figure 4.5a), while shifting to smaller grain sizes becomes slightly narrower and more asymmetric. After 5 h of milling, the size distribution gets narrower and the asymmetry starts reducing, indicating the formation of fine grains with a very small dispersion upon prolonged milling. In contrast with the results for the Ni solid solution, W (Figure 4.5b) exhibits an increasingly broad and asymmetric distribution up to almost 50 h of milling time. After 50 h of milling, the distribution abruptly gets narrow, and becomes almost symmetric as well as shifts to smaller average grain size. Milling in the shaker mill (Figure 4.6) shows similar trends as in the planetary mill, however the width of the size distribution is smaller in the case of milling carried out in the shaker mill than in the planetary mill.

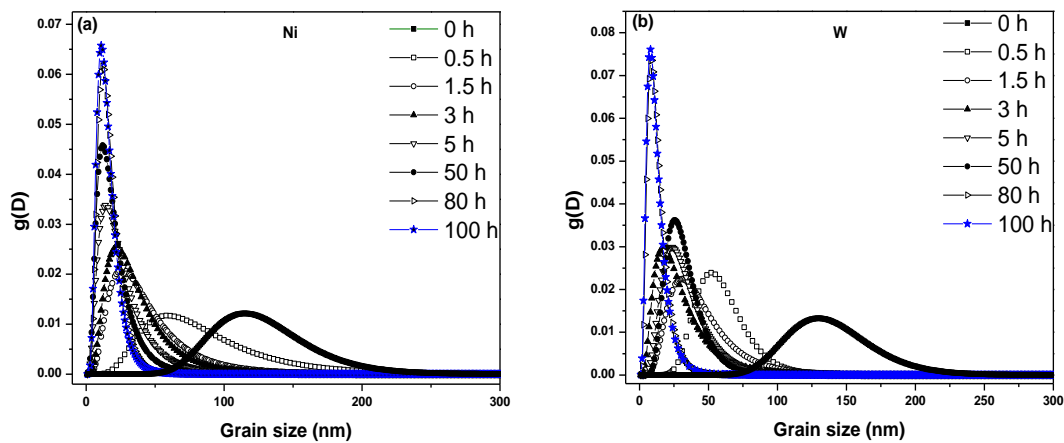


Figure 4.5: Crystallite/Grain size distribution with milling for (a) Ni and (b) W in Ni – 15 at. % W powder mixture milled in the planetary mill.

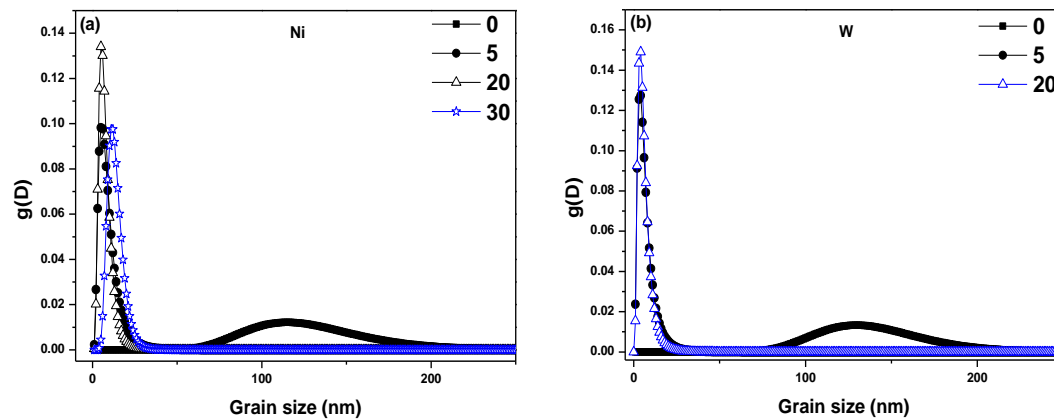


Figure 4.6: Crystallite/Grain size distribution with milling for (a) Ni and (b) W in Ni – 15 at. % W powder mixture milled in the shaker mill.

Detailed analysis of the diffraction-peak shapes reveals the occurrence of peak asymmetry for the Ni diffraction lines for the longest milling time of 100 h in the planetary mill. The development of a more pronounced broadening at the low-angle sides of the diffraction lines (“left-hand asymmetry”) is indicative of W dissolution, resulting in a lattice parameter increase; apparently, the W concentration in Ni is not (fully) homogeneous: W enrichment occurs in the proximity of Ni-W interfaces (see Figure 4.1; the microstructure at this stage consists of lamellae of the more brittle W embedded inside the more ductile Ni; see also what follows in Section 4.4.2). Milling in the shaker mill apparently leads to a more homogeneous distribution of W in Ni, as no pronounced Ni diffraction peak asymmetry can be discerned. It should be noted that neither the integral breadth nor the WPPM methods of line profile analysis consider a W concentration profile as a source of line broadening and therefore, the microstructural parameters (in particular the microstrain) as obtained after 100 h of ball milling in the planetary mill should be considered with caution.

4.4.2 Microstructural evolution upon annealing after milling: Non-ambient X-ray diffraction measurements

4.4.2.1 Line-broadening analysis

To investigate the coarsening behaviour of the milled nanocrystalline material, non-ambient X-ray diffraction measurements have been performed only on the powders milled in the planetary mill. The milling carried out in the shaker mill led to contamination (cf. section 4.4.1.2) due to abrasion of the milling equipment and therefore these specimens were not subjected to subsequent anneals. Studies were performed on the sample milled for 100 h in the planetary mill by heating to various temperatures between 300 °C and 850 °C in steps of 50 °C, making *in-situ* X-ray diffraction measurements at the selected temperatures. Sections of the thus recorded diffraction patterns containing the Ni 111 and W 110 reflections have been gathered in Figure 4.7. Repeated measurements were performed at each temperature, holding the temperature until no further changes in the diffraction pattern occurred, before proceeding to the next, higher temperature.

Except for peak shifts due to thermal expansion, no significant changes of the diffraction patterns of both the Ni-rich Ni(W) solid solution and W phases occur up to 450 °C. At 500 °C, after annealing for one hour, considerable broadening of the Ni(W) 111 reflection occurs, paralleled by an intensity decrease of the W 110 reflection. Upon continued annealing at 500 °C (for 14 hours; see Figure 4.7), it becomes evident that the broadening is caused by the development of a pronounced shoulder at the low-angle side of

the Ni(W) 111 reflection; the W 110 reflection intensity decreases further. This signifies the onset of dissolution of (remaining after milling) W into the Ni(W) solid solution leading to a concentration gradient in the Ni-rich solid solution (with higher W concentration at the Ni-W interfaces), resulting in an asymmetrically broadened peak of the Ni(W) solid solution. After continued intensity increase of the low-angle shoulder of the Ni(W) 111 reflection, a sharpening of the Ni(W) 111 reflection occurs during annealing to 700 °C due to progressing homogenization of the W concentration in Ni(W); at this temperature the W 110 diffraction line has almost completely vanished. Above 700 °C the intermetallic phase Ni₄W starts to develop. At 850 °C, the entire material consists of a Ni - ~12 at. % W solid solution and the Ni₄W phase (in agreement to the phase diagram).

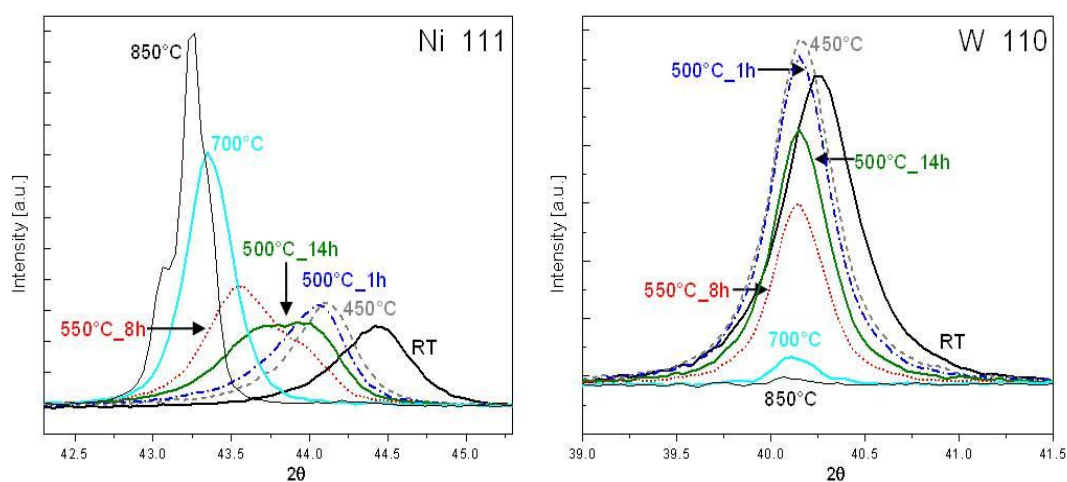


Figure 4.7: X-ray diffraction peak evolution of Ni(W) solid solution on in-situ annealing at different successive annealing temperatures for Ni 111 peak in Ni(W) solid solution and 110 peak of W.

These observed changes can be interpreted as follows: The onset of pronounced dissolution of W into the Ni-rich Ni(W) solid solution occurs at 500 °C. This leads to a concentration variation in Ni(W) such that W-rich regions develop in the proximity of the interfaces of the finely dispersed W particles, embedded in Ni grains, with the Ni matrix, implying that regions with a lower W concentration prevail: Pronounced broadening of the Ni(W) 111 reflection occurs. Upon further heating, a homogenisation of the W concentration, associated with Ni(W) 111 peak narrowing and a further decrease of the intensity of the W 110 reflection occur. Upon reaching the solubility limit for W in Ni, the intermetallic phase Ni₄W forms.

Since the broadening of the Ni peaks, induced by annealing of the nanocrystalline powders produced in the planetary mill, is due to W dissolution, the line-broadening

analysis methods used for the as-milled powder (section 4.2) cannot be employed here straightforwardly to extract microstructural information upon annealing. Therefore, the following approximate analysis described below has been adopted to extract data on the microstructural changes during annealing of the nanocrystalline powders.

All asymmetric peaks of the Ni(W) solid solution in the diffraction patterns measured upon annealing are fitted using two symmetric pseudo-Voigt functions; the high-angle-peak is attributed to a Ni(W) solid solution with a lower W content and the low-angle peak is attributed to a Ni(W) solid solution with a high W content. This fitting procedure allows the deconvolution of the asymmetric diffraction profiles into peaks pertaining to the respective W-rich and W-poor Ni(W) phases. Examples of this fitting procedure are provided in Figure 4.8.

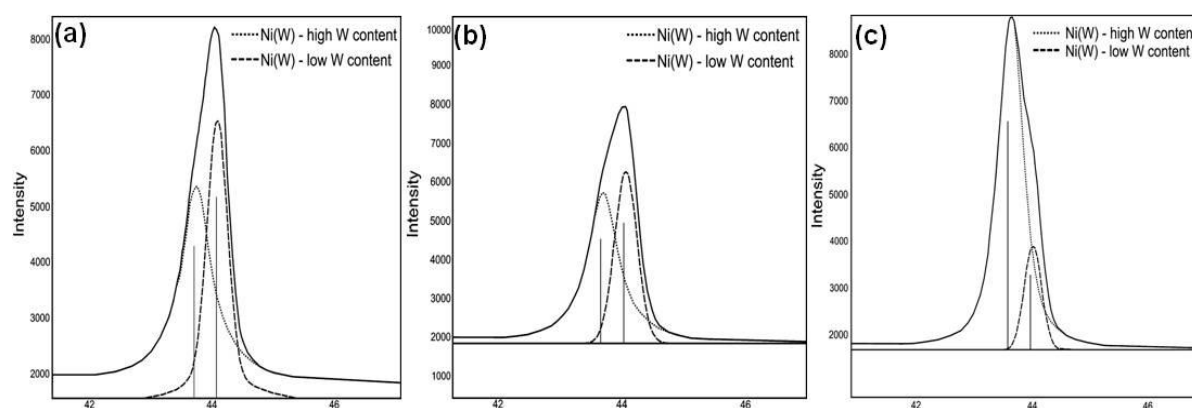


Figure 4.8: Applied fitting procedure for evaluation of the diffraction data showing the 111 Ni-W peak and the two symmetric peaks fitted to a single asymmetric profile peak due to compositional variations for the powder annealed at (a) 500 °C for 2 h, (b) 500 °C for 10 h and (c) 550 °C for 8 h.

It follows from Figure 4.8 that with increasing annealing time at 500 °C the integrated intensity of the peak attributed to Ni(W) solid solution with a high W content increases, whereas the integrated intensity of the peak from the Ni(W) solid solution with a low W content decreases. Similarly, upon continued annealing at 550 °C, further increase of the intensity of the high-W content peak occurs, concurrently with a decreasing intensity of the low-W content Ni(W) peak, along with narrowing of all diffraction profiles. Eventually, as the broadening further reduces at higher temperatures, the profile can again be fitted with one single symmetric function.

On the above basis, the crystallite size and the microstrain have been calculated using the single-line analysis by averaging over all measured reflections. The thus

determined developments of the crystallite size and microstrain with increasing temperature for the different phases are shown in Figure 4.9.

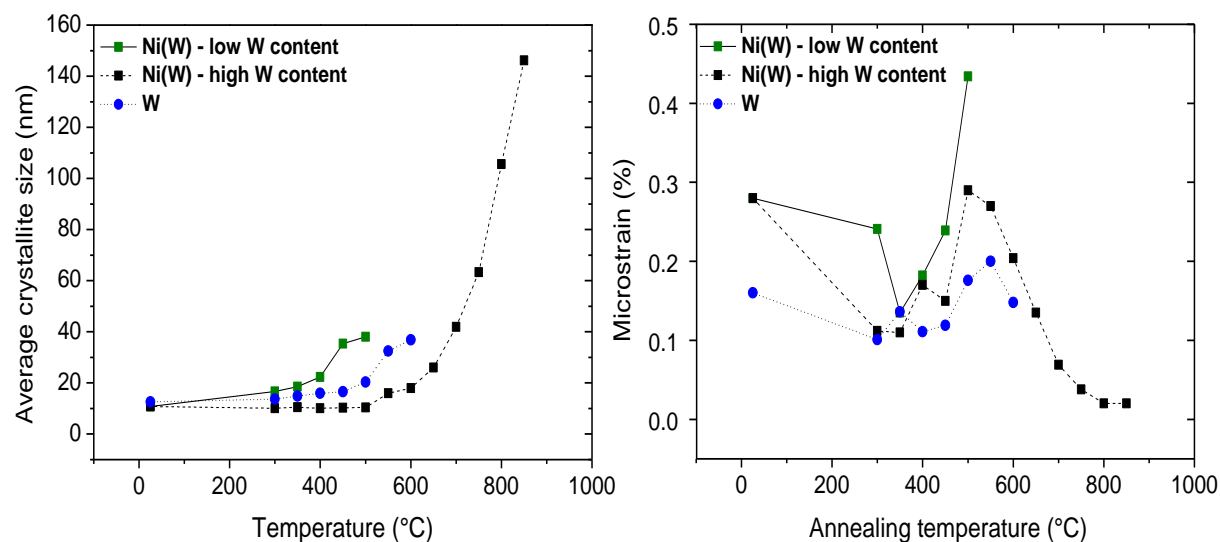


Figure 4.9: Development of the crystallite size and microstrain of the different phases (low- and high- W content Ni; and W) as a function of temperature. The plotted values are calculated from the last measurement at the respective temperature.

The results shown above reveal that with increasing annealing temperature, the Ni-rich crystallites containing a relatively higher content of W are more stabilized against grain growth than the Ni-rich crystallites of smaller W content: Grain growth is suppressed for the W-rich Ni(W) solid solution up to a temperature of almost 600 °C; grain growth in the W-poor Ni(W) solid solution starts at a temperature of about 400 °C. This increased microstrain for the W-poor Ni(W) solid solution at 400 °C can be understood as due to concentration inhomogeneity [223]. Starting at a temperature of 650 °C, the Ni(W) diffraction peaks can be well fitted (again) with a single (symmetric) Pseudo-Voigt function; (the W peak intensities have reduced considerably, so that further line-broadening analysis of the W peaks has become impossible). This result indicates homogenization of the W concentration in the Ni grains upon increasing the annealing temperature.

The lattice parameter of the Ni(W) solid solution eventually reaches a saturation value upon increasing annealing temperature as the maximum solubility of W in Ni is attained (~ 12 at. %).

The grain growth evolution exhibits a grain size < 20 nm even after annealing at a temperature of 600 °C. Subsequent annealing at higher temperature involves pronounced grain growth with a simultaneous recovery (exhibited by smoothly decreasing microstrain

content): a mean grain size of ~ 140 nm is reached at 850 °C (with then a negligible microstrain). TEM micrographs made from this stage of annealing (Figure 4.10) confirm the magnitude of grain growth as determined by XRD: The as-milled specimen consist of crystallites with sizes of about 10 nm's (Figure 4.10a) which grow more or less uniformly during annealing to 850 °C (Figure 4.10b), i.e. showing no signs of abnormal grain growth.

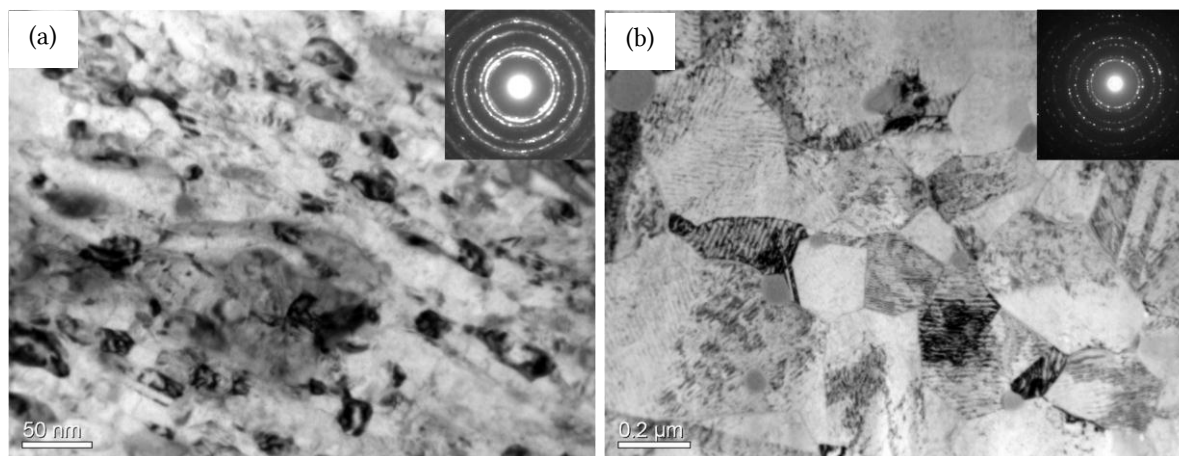


Figure 4.10: TEM bright field micrographs of the Ni – 15 at. % W (a) as milled for 100 h in planetary mill and (b) on annealing the milled specimen to 850 °C.

For a more detailed investigation of the grain coarsening behaviour, isothermal annealing experiments were conducted in the temperature range from 500 °C to 650 °C. The grain size and microstrain evolutions, upon isothermal annealing at various temperatures, for the W-rich Ni(W) solid solution are shown in Figure 4.11. The microstructural evolution of ball-milled pure Ni powder, prepared under exactly the same milling conditions, annealed isothermally at 500 °C (★ data points) has also been included in Figure 4.11. Evidently, the nanocrystalline Ni(W) solid solution exhibits a much less distinct grain growth than nanocrystalline pure Ni. In line with the present work, it has been reported in Ref. [196] that a nanocrystalline microstructure was stabilized in electrodeposited Ni-W films containing between 6 and 21 at. % up to a temperature as high as 500 °C.

At 500 °C no grain growth occurs for the W-rich Ni(W) solid solution. At higher temperatures, grain growth takes place (Figure 4.11). The crystallite/grain size appears to attain a saturation value at each temperature. This saturation value increases with increasing annealing temperature (Figure 4.12). The microstrain during isothermal annealing is more or less the same for all annealing temperatures. A possible decrease of the microstrain due to crystalline imperfection, as observed to take place prominently for pure Ni (★ data points), may be masked by a microstrain-like broadening due to compositional inhomogeneity.

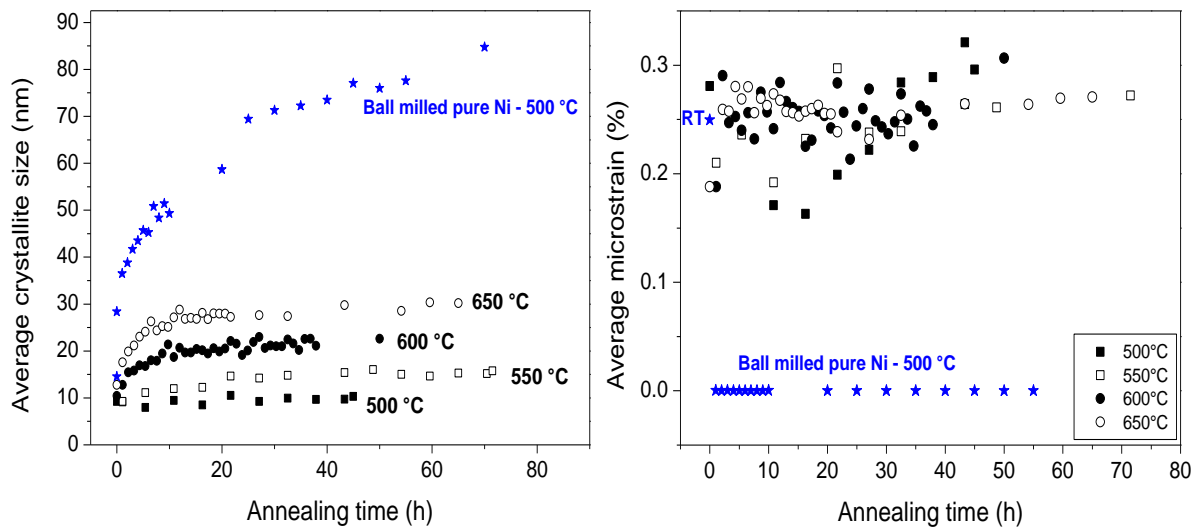


Figure 4.11: Development of the crystallite size and microstrain of the W-high content Ni on isothermal annealing. Shown in the figure (star data points, RT denotes the data point of the as milled Ni before annealing) microstructural evolution of pure Ni which was ball milled under exactly the same conditions and having quite similar initial microstructure as the Ni-W specimen taken for the isothermal annealing studies.

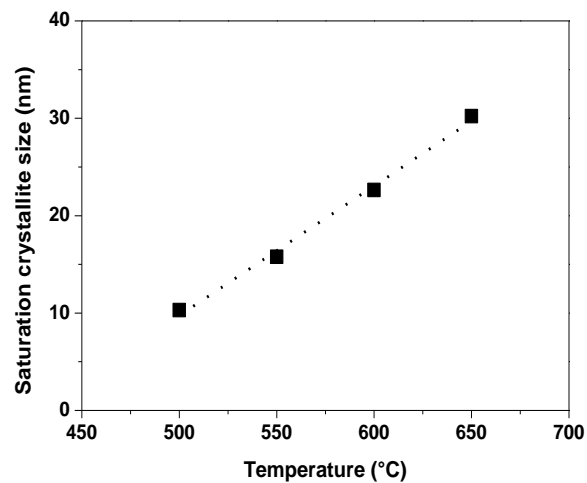


Figure 4.12: Maximum crystallite size obtained on isothermal annealing at each temperature.

The stability of the microstructure of the nanocrystalline W-rich Ni(W) solid solution, as compared to nanocrystalline pure Ni, up to an annealing temperature of about 600 °C has to be ascribed to the presence of dissolved W. On the one hand grain-boundary-energy reduction can be caused by W segregation, i.e. the driving force for grain coarsening is reduced, on the other hand, an increased activation-energy for grain-boundary migration may be due to the presence of dissolved W [218, 224].

4.4.2.2 Composition of the Ni(W) solid solution formed on annealing.

To determine the W content dissolving into Ni during annealing, the development of the lattice parameter of the Ni(W) solid solution, as derived for both the high- and low- W-content peak positions, was traced by XRD. The dependence of the Ni(W) lattice parameter on W content was adopted according to Ref. [213],

The development of the lattice parameter of the respective Ni(W) solid solution with high- and low- W-content, as determined at the end of each isothermal annealing process, (i.e. the saturation crystallite size) has been established and is shown in table 4.3.

Table 4.3: W content of the Ni(W) solid solution as determined from lattice parameter measurements (a) for the Ni(W) solid solution with a low W content and (b) for the Ni(W) solid solution with a high W content, for the samples isothermally annealed at various temperatures.

Temperature (°C)	X_W (at. %)	
	Low W-content peak	High W-content peak
500	2.13	9.72
550	4.37	11.45
600	7.04	11.79
650	9.18	11.81

The high-W content Ni(W) phase attains the maximum equilibrium concentration of ~ 12 at. % according to the phase diagram at 550 °C. The low-W content Ni(W) phase shows a W content still much below the maximum equilibrium concentration. This distinct concentration gradient in the Ni grains even at such high temperatures, thereby indicates a very slow dissolution (and homogenisation) of W into Ni. This is not unlikely considering the small negative heat of mixing of Ni and W ~ -3 kJ/mol and the relatively low value for the diffusion coefficient of W in Ni.

4.4.2.3 Heat evolution upon annealing after milling; differential scanning calorimetry

A number of studies have focused on the heat (enthalpy) evolution during annealing of both pure [112, 225] and alloyed [81, 226] nanocrystalline materials. Exothermic effects have mainly been attributed to two irreversible reactions: grain-boundary relaxation and grain growth. During grain-boundary relaxation, energy stored in the form of excess grain-boundary dislocations (i.e. additional dislocations with respect to the geometrically

necessary grain-boundary dislocations that account for the misorientation across the boundaries and which are associated with the structural geometry of the boundaries) is released as the boundary transforms to a more stable configuration. Crystallite growth also is an exothermic process because of the associated reduction of total grain-boundary area in the specimen [48].

In the present work, calorimetric measurements have been carried out, on ball milled specimens of different grain sizes (i.e. powders obtained after different milling times), at low temperatures where, negligible grain growth is expected. As can be seen from Figure 4.13, for larger grained specimen (32 nm) a small exothermic peak is observed at lower temperature which is followed by a broad endotherm at higher temperature. This endothermic peak decreases in intensity with decreasing grain size and is completely absent for small grain sizes (below 13 nm) where a continuous broad exothermic peak starts at ~ 120 °C and extends beyond the measurement region, probably also overshadowing the endothermic event. There is also an indication of two exothermic processes occurring separated by the endothermic event (24 nm and 18 nm). The total amount of heat released for the different samples cannot be determined because no clear peaks of the exothermic signals can be defined due to incomplete reaction in the measurable temperature range. However, it can be said positively that the amount of heat released scales inversely with grain size.

The presence of an endothermic peak in ball milled specimens has been reported before [227] but its origin is a topic of controversy. Some authors interpret it simply as due to desorption of gases [228], to the homogenization of solid solution involving dissolution of an intermediate intermetallic phase [226], to the occurrence of partial amorphisation [229] or as a consequence of lattice expansion on reduction of grain size [230, 231]. Since the magnitude of the endothermal event reduces with increased milling time, it is unlikely that the endothermic peak is due to desorption of gases, since with increasing milling time, adsorption of gases can only increase which would lead to larger endothermic event.

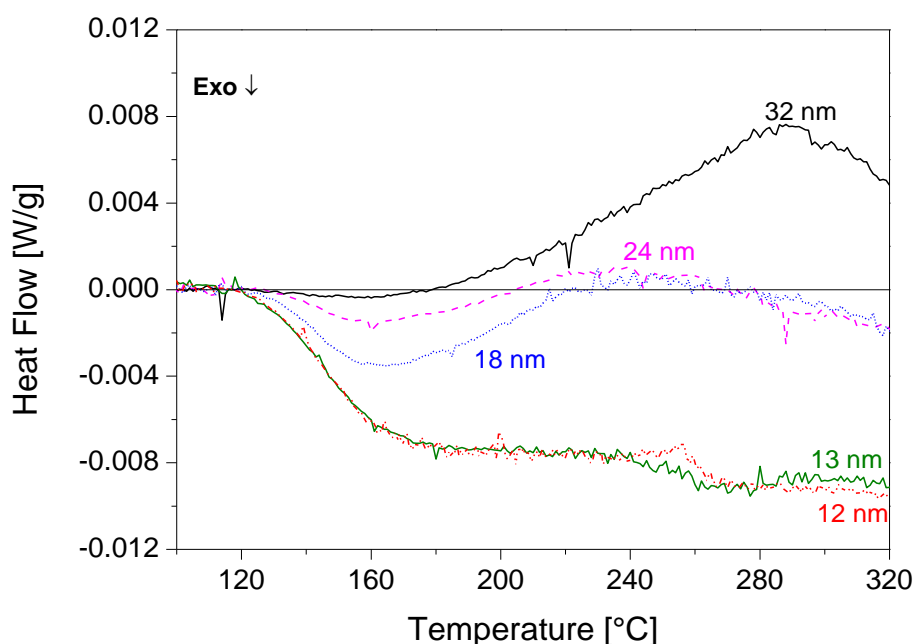


Figure 4.13: DSC results showing the irreversible heat release in the samples milled for various times in the planetary ball mill.

Further, since such an endotherm is also observed in pure metals [232], hence the peak may not be attributed to homogenization of solid solution. At present, the origin of the endothermic event is unclear and would require further studies.

However, the significant amount of heat released (exotherm) with the onset temperature of 120 °C (before grain growth takes place), can be attributed to grain-boundary relaxation. These results are in good agreement with data reported in Ref. [196] on electrodeposited NiW specimens with different grain sizes which showed an onset temperature of ~ 120 °C for the exothermic reactions and was attributed to grain-boundary relaxation.

4.5 Summary

- 1) Ball milling of elemental powder mixtures of Ni and W with a nominal composition of Ni – 15 at. % W carried out in a planetary mill and a high-energy shaker mill leads to the formation of nanocrystalline, strained Ni-W alloy.
- 2) The milling process in the shaker mill is much more efficient than the milling process in the planetary mill: Similar reductions in crystallite size and increases in microstrain can be obtained by employing the shaker mill in a much shorter

time as compared to the planetary mill. A maximum concentration of ~ 12 at. % W in Ni was obtained upon milling in the shaker mill for 30 h.

- 3) The integral-breadth methods (single-line analysis and the modified Williamson-Hall method) revealed qualitatively similar trends for the evolution of the microstructural parameters crystallite/grain size and microstrain, determined as a function of milling time. Whole powder pattern modelling led to similar trends as well.
- 4) As compared to nanocrystalline pure Ni powder, the nanocrystalline Ni(W) solid solution is stable up to about 600 °C. At higher temperatures (but below 700 °C), crystallite/grain growth occurs. At the same time, W dissolves into the Ni(W) solid solution, resulting in concentration inhomogeneities exhibited by pronounced diffraction-line broadening. Dissolution of almost ~ 12 at. % W into Ni was reached upon annealing at a temperature of 850 °C.
- 5) Before grain growth takes place, significant grain-boundary relaxation takes place, as revealed by significant release of heat at this stage. The high stability of the Ni(W) solid solution, against grain coarsening, at elevated temperatures is attributed to the combined effect of grain-boundary-energy reduction (by W segregation), i.e. the driving force for grain coarsening is reduced, and an increase of the activation energy for grain-boundary migration takes place.

Chapter 5

Summary

The unique properties exhibited by nanocrystalline materials have been the subject of widespread research for over two decades due to fundamental scientific interest as well as the increasing technological importance of such materials. The extremely large interfacial area per unit volume of nanocrystalline materials has a significant influence on the properties of these materials and the specific anomalies observed are related to the particular *microstructure* of the nanocrystalline state. Microstructural studies, by definition, encompass the study of the arrangement of crystallites (of same or differing phase constitution) and of the crystal defects. This thesis titled '*Microstructure and grain growth of nanosized materials*' addresses these microstructural features of nanoscaled materials.

The microstructure of a material depends pronouncedly on the fabrication method. The method employed in this work for the preparation of nanocrystalline materials is mechanical milling which leads to the formation nanocrystalline materials with far-from equilibrium structures owing to the large amount of defects introduced upon milling. Plastic deformation leads to not only defects in the form of grain boundaries, dislocations and faults within the grains but also, high-density ensembles of non-equilibrium dislocations in the grain boundaries along with an excess concentration of vacancies are generated. The microstructure of such nanocrystalline materials has been investigated in the present work primarily by employing dedicated X-ray diffraction line profile analyses which are very efficacious methods to extract detailed microstructural information.

Investigations of the dependence of the lattice parameter on the crystallite size have been presented in **chapter 2**. Pure elemental nanocrystalline metal powders having different crystal structures (Ni, Cu (fcc) and Fe, W (bcc)) showed an anomalous variation of the lattice parameter with decreasing crystallite size: A *lattice contraction* followed by *lattice expansion* with decreasing crystallite size. This behavior has been attributed to two competing effects (see Figure 5.1):

- 1) Interface tension leading to lattice contraction (Gibbs-Thomson effect): Due to the reduction of the crystallite size, the increased radius of curvature induces compressive stress which increases with decreasing crystallite size.
- 2) Excess free volume leading to lattice expansion: The stress field induced by excess free volume, originating at the grain boundaries, and its propagation into the grains leads to deviation of atoms from its ideal position and thus to lattice expansion.

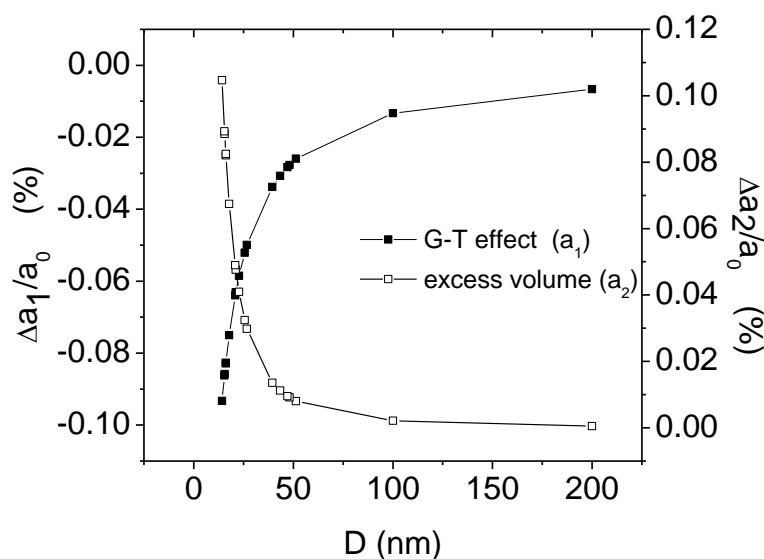


Figure 5.1: Relative change of lattice parameter as a function of grain size as a result of the Gibbs-Thomson effect (lattice contraction) and as a result of the presence of excess free volume at the grain boundaries (lattice expansion).

A simple model combining the effects of excess free volume and the interface stress can be used to assess the value of the interface stress by fitting this model to the experimental data, with the interface stress as the only fit parameter. The interface stress appears to increase almost linearly with increasing melting point. The interface stress values thus obtained are comparable with literature values.

Chapter 3 is devoted to the investigation of the microstructural evolution upon ball milling of nickel and the thermal stability of the resulting nanocrystalline microstructure by applying different methods of X-ray diffraction line profile analysis. Single-line analysis, whole powder-pattern modelling and the Warren-Averbach method were employed. Ball milling leads to a decrease of grain size, down to a saturation level of 18 nm, a continuous increase of microstrain (dislocation density) and a continuous increase of the stacking fault probability. The grain-size distribution can be described by a lognormal distribution. Upon continued ball milling the grain-size distribution becomes very narrow.

The thermal stability and the grain growth kinetics of two microstructurally distinct specimens were traced by isothermal annealing studies employing in-situ and ex-situ X-ray diffraction measurements: Samples from powders milled for 5 h and 80 h were used for grain-growth studies recognizing their distinctly different initial microstructural features: The 5 h milled and 80 h milled specimens have crystallite size of about 30 nm and 15 nm, respectively. The microstrain is much larger in the 80 h milled specimen. The microstructure of the 80 h milled specimen is likely more homogeneous than the 5 h milled specimen. The grain growth studies were carried out for extended annealing times in order to cover the entire growth process. The milled samples were first examined by heating the 5 h milled and 80 h milled specimens at a rate of 0.5 K/s to a particular temperature, followed by an isothermal anneal for 10 h (at each temperature), before proceeding to the next higher temperature (see Figure 5.2). A striking grain size dependent thermal stability was observed: The 80 h milled specimen with a smaller average crystallite size (≈ 18 nm) showed distinctly higher thermal stability against coarsening (i.e. pronounced grain growth occurred at a higher temperature) than the 5 h milled specimen with a larger average crystallite size (≈ 30 nm) (see Figure 5.2).

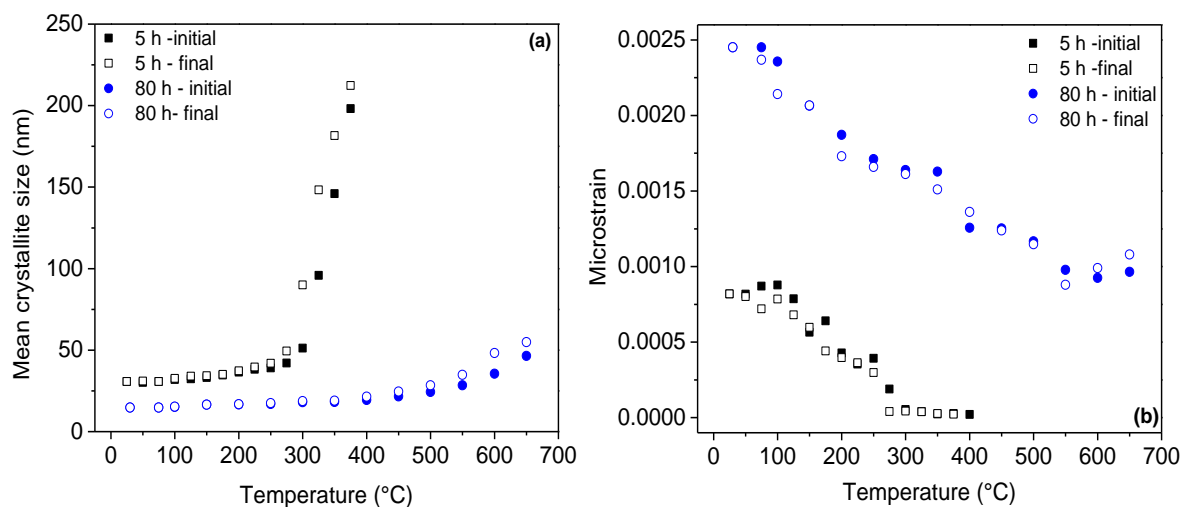


Figure 5.2: (a) Crystallite size and (b) microstrain evolution as a function of annealing temperature for the 5 h milled and 80 h milled specimens (the filled symbol represents the data for the first measurement and the hollow symbol for the final measurement after 10 h at the particular temperature)

Based on this preliminary characterization, isothermal investigations for extended periods of time were performed at selected temperatures (for further details, see Chapter 3). The isothermal grain growth kinetics also differed for the two specimens. An initial very rapid grain growth which accompanied microstrain relaxation in the materials was common to both the specimens, followed by a stage of more or less linear grain growth. In

case of an initially wide grain-size distribution (5 h milled specimen), grain growth occurs much faster and eventually a saturation value of grain size is reached that depends on the temperature (i.e. it increases with temperature). The developing grain-size distributions (derived from the size Fourier coefficients of different diffraction lines) become of bimodal nature in case of the 5 h milled specimen with an initially wide size distribution and exhibits pronounced broadening with a distinct tail to larger size values in case of the 80 h milled specimen with an initially narrow size distribution.

Grain-growth models based on grain-boundary curvature driven grain growth cannot describe the observed grain-growth kinetics. The activation-energy values derived from the growth-rate constants for linear growth are in the range of 100 kJ/mol (for the nc Ni of initially 18 nm grain size and narrow grain size distribution) to 158 kJ/mol (for the nc Ni of initially 35-38 nm grain-size and a broad grain-size distribution). The very first stage of fast growth (see above), preceding the linear growth stage, is ascribed to a high mobility of the initially unrelaxed grain boundaries of the nanocrystalline material which initially contain a high amount of excess free volume. This amount of excess free volume in the grain boundaries is likely larger for the finer grained (80 h milled) nanocrystalline material, which is compatible with the significantly lower value of the activation energy for the subsequent stage of linear grain growth in the finer nanocrystalline material as compared to the coarser nanocrystalline material. The observation that the finer nanocrystalline material of much narrower size distribution has the lower activation energy of grain growth and yet exhibits pronounced grain growth at temperatures higher than the coarser nanocrystalline material of wider size distribution (cf. Figure 5.2) is ascribed to so-called 'abnormal grain growth' as the prevailing grain-growth mechanism.

In **Chapter 4**, the influence of alloying Ni with W on the thermal stability has been investigated. To this end, the microstructural evolution upon milling and subsequent annealing in the temperature range from 25 °C to 800 °C was investigated employing ex-situ and in-situ X-ray diffraction integral breadth (single-line and Williamson-Hall) methods and whole powder pattern modelling as well as scanning electron microscopy, transmission electron microscopy and differential scanning calorimetry.

For mechanical alloying two types of ball mills were used: a planetary mill and a high energy shaker mill. The milling process in the shaker mill is much more efficient than the milling process in the planetary mill: Similar reductions in crystallite size and increases in microstrain can be obtained by employing the shaker mill in a much shorter time as compared to the planetary mill. While about 2 at. % W dissolved in Ni after 100 h of milling

in a planetary mill, the maximum solid solubility (according to the phase diagram) of W in Ni (12 at. %) has been reached after already 30 h of milling in shaker mill. However, abrasion of the milling equipment occurred for the high energy shaker mill. Therefore, the such prepared specimens were not subjected to subsequent anneals; investigations of the thermal stability of the Ni-W powder were performed only for the material prepared employing the planetary mill.

As compared to nc pure Ni powder, the nc Ni(W) solid solution is stable up to about 500 °C (see Figure 5.3). At higher temperatures crystallite/grain growth occurs. At the same time, W dissolves into the Ni(W) solid solution, resulting in concentration inhomogeneities exhibited by pronounced diffraction-line broadening. Dissolution of almost ~ 12 at. % W into Ni was reached upon annealing at a temperature of 850 °C.

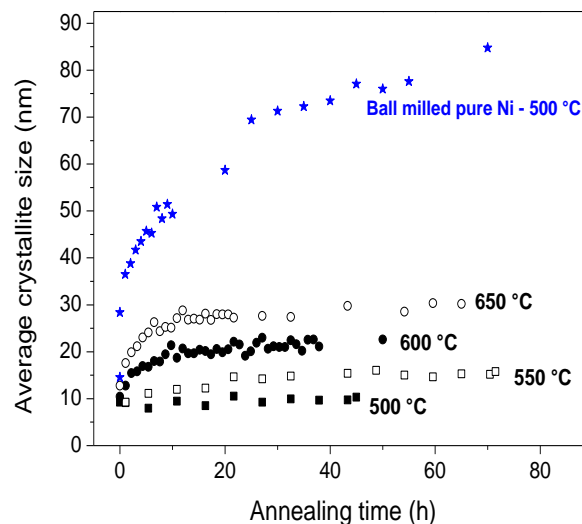


Figure 5.3: Development of the crystallite size of the Ni(W) solid solution with a high W content (for further details see Chapter 4) upon isothermal annealing. The microstructural evolution of pure Ni powder which was ball milled under exactly the same conditions and which exhibits a similar initial microstructure as the Ni-W specimen has been indicated by the star symbols (★) in the figure as well.

The high stability of the Ni(W) solid solution, against grain coarsening, at elevated temperatures is attributed to the combined effect of grain-boundary-energy reduction (by W segregation), i.e. the driving force for grain coarsening is reduced, and an increase of the activation energy for grain-boundary migration. Before grain growth takes place, significant grain-boundary relaxation takes place, as revealed by significant release of heat at this stage.

Chapter 6

Zusammenfassung in deutscher Sprache

Die einzigartigen Eigenschaften nanokristalliner Materialien waren sowohl aufgrund wissenschaftlichen Interesses, als auch wegen ihrer technologischen Bedeutung seit mehr als zwei Jahrzehnten Gegenstand zahlreicher Forschungsarbeiten.

Die extrem hohe Grenzfläche pro Einheitsvolumen von nanokristallinen Materialien hat einen signifikanten Einfluss auf die Eigenschaften dieser Materialien und die beobachteten spezifischen Besonderheiten in den Eigenschaften lassen sich auf die nanokristalline *Mikrostruktur* zurückführen. Die vorliegende Arbeit mit dem Titel „*Mikrostruktur und Kornwachstum von nanoskaligen Materialien*“ ist der Untersuchung einiger dieser besonderen Eigenschaften von nanoskaligen Materialien gewidmet.

Die Mikrostruktur eines Materials hängt wesentlich von dessen Herstellungsmethode ab. Die Herstellungsmethode, die in dieser Arbeit verwendet wurde, ist das mechanische Mahlen, das zu der Bildung von nanokristallinen Materialien führt mit Mikrostrukturen, die aufgrund des Einbringens zahlreicher Defekte während des Mahlens weit entfernt von Gleichgewichtszuständen sind. Nanokristallisation aufgrund von plastischer Deformation führt nicht nur zu Defekten in Form von Korngrenzen und Versetzungen, sowie Gitterfehlern innerhalb der Körner, aber auch zu Überschuss-Versetzungen in den Korngrenzen und einer Überschusskonzentration an Leerstellen.

Die Mikrostrukturen von nanokristallinen Materialien wurde in der vorliegenden Arbeit insbesondere mittels geeigneter Röntgenbeugungs-Linienprofilanalysen untersucht, die eine sehr geeignete Methode zur Extraktion der verschiedenen mikrostrukturellen Charakteristika darstellt. Die wesentlichen Ergebnisse dieser Dissertation können wie folgt zusammengefasst werden.

Untersuchungen zur Abhängigkeit des Gitterparameters von der Kristallitgröße werden in **Kapitel 2** vorgestellt. Nanokristalline Metallpulver aus reinen Elementen unterschiedlicher Kristallstruktur (Ni, Cu (kubisch flächenzentriert) und Fe, W (kubisch raumzentriert)) zeigten eine anomale Variation des Gitterparameters mit abnehmender Kristallitgröße: Eine *Gitterkontraktion* gefolgt von einer *Gitterdehnung* mit abnehmender

Kristallitgröße. Dieses Verhalten konnte durch das Auftreten von zwei konkurrierenden Effekten erklärt werden (siehe Abb. 6.1):

- 1) Die Grenzflächenspannung führt zu einer Gitterkontraktion (Gibbs-Thomson-Effekt): Die Abnahme der Kristallitgröße führt zu einem vergrößerten Krümmungsradius welcher mit abnehmender Kristallitgröße zunehmende Druckspannungen hervorruft.
- 2) Ein Überschuss von freiem Volumen an den Korngrenzen führt zu einem Spannungsfeld und damit zu einer Gitterdehnung (Aufweitung).

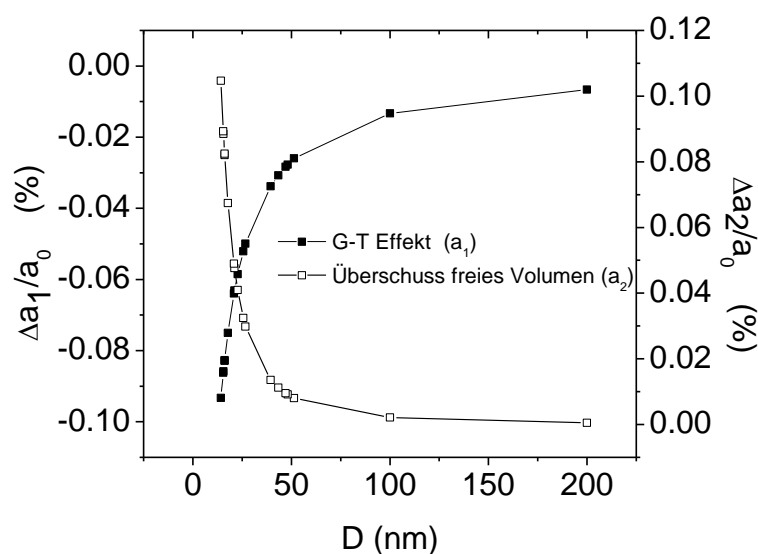


Abb. 6.1: Erwartete relative Änderung des Gitterparameters als Funktion der Korngröße als Resultat des Gibbs-Thomson-Effekts und des Überschusses von freiem Volumen an den Korngrenzen.

Ein einfaches Modell, das die Auswirkungen der Grenzflächenspannung und des freien Volumens an den Korngrenzen auf den Gitterparameter berücksichtigt, kann zur Abschätzung der Grenzflächenspannung benutzt werden indem das Modell an die experimentell ermittelten Daten angepasst wird, wobei die Grenzflächenspannung den einzigen freien Parameter darstellt. Es ergeben sich mit der Literatur vergleichbare Grenzflächenspannungen, die nahezu linear mit der Schmelztemperatur der untersuchten Materialien ansteigen.

Kapitel 3 ist der Untersuchung von reinem Nickel während des Kugelmahlens und der thermischen Stabilität der resultierenden nanokristallinen Mikrostruktur gewidmet. Hierzu wurden verschiedene Methoden der Röntgenbeugungs-Linienprofilanalyse, nämlich Einzellinienanalyse, Whole Powder Pattern Modeling, sowie die Warren-Averbach-Methode verwendet.

Das Mahlen führt zu einer Abnahme der mittleren Kristallitgröße bis auf ca. 18 nm und einem Ansteigen der Mikrodehnung (Versetzungsdichte) und der Stapelfehlerwahrscheinlichkeit. Die Kristallitgrößenverteilung kann durch eine lognormal-Verteilung angenähert werden, deren Breite mit zunehmender Mahldauer abnimmt.

Die thermische Stabilität und die Kinetik des Kornwachstums wurden sowohl ex-situ als auch in-situ mittels isothermer Wärmebehandlungen untersucht. Dabei wurden die folgenden Proben betrachtet: *80 h gemahlenes Ni* mit einer anfänglichen Korngröße von ~ 15 nm und einer Mikrodehnung von $\sim 0,3\%$, und einer engen Korngrößenverteilung, sowie *5 h gemahlenen Ni* mit ungefähr doppelt so großer anfänglicher Korngröße (~ 30 nm), einer Mikrodehnung von $\sim 0,15\%$ und einer breiten Korngrößenverteilung. Die Mikrostruktur der für 80 h gemahlene Probe ist als homogener anzunehmen.

Die gemahlene Proben wurden zunächst mit einer Rate von 0,5 K/s auf eine bestimmte Temperatur aufgeheizt und dann vor dem nächsten Temperaturschritt für 10 Stunden isotherm geglüht (siehe Abb. 6.2.). Dabei wurde eine erstaunliche korngrößenabhängige thermische Stabilität festgestellt: Die Probe mit relativ kleiner mittlerer Korngröße (≈ 18 nm, 80 h Probe) zeigt eine deutlich höhere thermische Stabilität als die Probe mit höherer mittlerer Korngröße (≈ 30 nm, 5 h Probe; siehe Abb. 6.2).

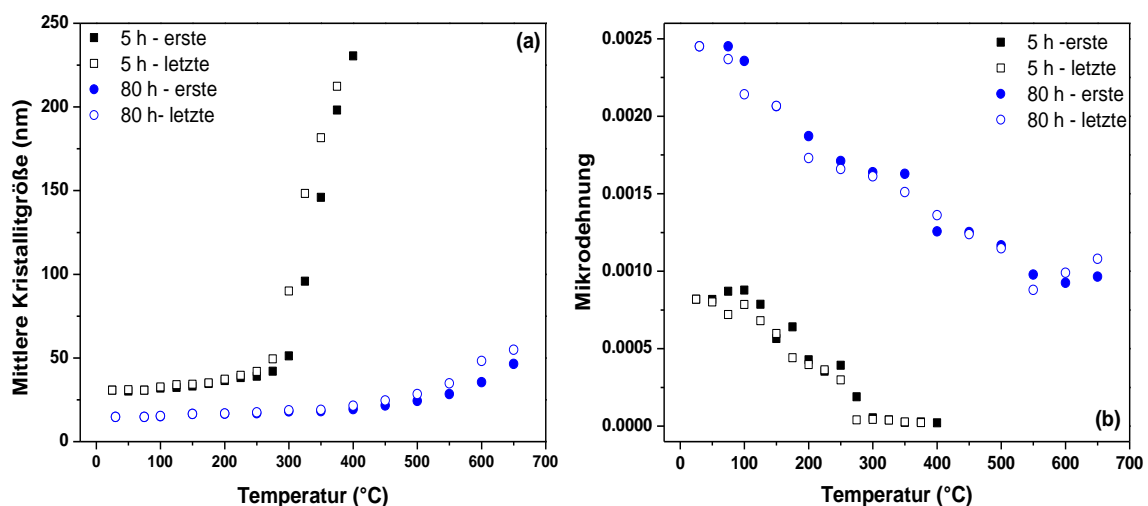


Abb. 6.2: (a) Kristallitgrößen- und (b) Mikrodehnungs- Entwicklung als Funktion der Glühtemperatur für die 5 h und 80 h Proben (die ausgefüllten Symbole kennzeichnen die Daten für die erste Messung und die offenen Symbole die letzte Messung bei der jeweiligen Temperatur).

Auf Basis dieser Untersuchungen wurden Temperaturen für die Untersuchungen der isothermen Kornwachstumskinetik für ausgedehnte Zeiträume ausgewählt (für weitere Details siehe Kapitel 3). Die isotherme Kornwachstumskinetik wies ebenfalls eine starke

Abhängigkeit von der anfänglichen Mikrostruktur auf. Während des isothermen Kornwachstums zeigten beiden Ni-Proben (5 h und 80 h gemahlen) ein anfänglich lineares, sehr schnelles Kornwachstum, das von einer ausgeprägten Abnahme der Mikrodehnung begleitet wird. Nach dieser schnellen Kornwachstumsphase folgt ein Bereich von mehr oder weniger linearem Kornwachstum. Für den Fall einer breiten Kristallitgrößenverteilung in der gemahlten Probe (5 h Probe) tritt sehr viel schnelleres Kornwachstum auf und es wird letztendlich ein Sättigungswert der Kristallitgröße erreicht, der mit zunehmender Temperatur ansteigt. Die aus den Fourierkoeffizienten für die Kristallitgröße bestimmten Kristallitgrößenverteilungen zeigen einen bimodalen Charakter für die 5 h Probe, welche im Ausgangszustand (nach dem Mahlen) eine breite Kristallitgrößenverteilung aufweist; für die 80 h Probe, die im Ausgangszustand eine enge Kristallitgrößenverteilung aufweist, ergibt sich nach der Wärmebehandlung eine sehr breite Kristallitgrößenverteilung mit einem ausgeprägtem Ausläufer zu großen Kristallitgrößen.

Keines der bekannten Kornwachstumsmodelle (basierend auf der Krümmung von Korngrenzen als Triebkraft) konnte die in dieser Arbeit ermittelte Kornwachstumskinetik zutreffend beschreiben. Die Aktivierungsenergien, die aus den Wachstumskonstanten für den Bereich des linearen Wachstums bestimmt wurden, liegen im Bereich zwischen 100 kJ/mol (für die 80 h gemahlene Probe mit einer Kristallitgröße von 18 nm und einer engeren Kristallitgrößenverteilung) und 150 kJ/mol (für die 5 h gemahlene Probe mit einer Kristallitgröße von 30 nm und einer breiteren Kristallitgrößenverteilung). Die dem Stadium des linearen Wachstums vorausgehende Phase des sehr schnellen Kornwachstums kann der sehr hohen Mobilität der nach dem Mahlen unrelaxierten Korngrenzen zugeschrieben werden, die viel freies Volumen enthalten. Die Menge dieses freien Volumens ist für die 80 h Probe vermutlich viel größer und deswegen ergibt sich für diese Probe eine geringere Aktivierungsenergie (siehe oben) im nachfolgenden Stadium des linearen Kornwachstums. Dass trotzdem für die 80 h Probe (engere Kristallitgrößenverteilung mit geringerer mittlerer Kristallitgröße) verglichen mit der 5 h Probe (breitere Kristallitgrößenverteilung mit höherer mittlerer Kristallitgröße) erst bei sehr viel höherer Temperatur merkliches Kornwachstum auftritt (siehe Abb. 6.2) muss dem Auftreten von ‚abnormalem Kornwachstum‘ als vorherrschendem Wachstumsmechanismus zugeschrieben werden.

In **Kapitel 4** wurden das mechanische Legieren und dessen Einfluss auf die thermische Stabilität durch Mahlen von Ni mit W untersucht. Hierzu wurden zwei Arten von Mühlen benutzt: Eine Hochenergie-Schüttelmühle und eine Planetenkugelmühle. Während ungefähr 2 At % W nach einer Mahldauer von 100 h in der Planetenkugelmühle in

Ni gelöst werden konnten, wurde die maximale (gemäß Phasendiagramm) Löslichkeit von 12 At % W in Ni bereits nach einer Mahldauer von 30 h in der Schüttelmühle erreicht. Allerdings traten beim Mahlprozess in der Schüttelmühle Verunreinigungen des Pulvers durch Abrieb des Mahlwerkzeugs auf. Aus diesem Grund wurde nur das für 100 h in der Planetenkugelmühle gemahlene Ni-W Pulver mit 2 At. % W gegläht (bis 800 °C) um die thermische Stabilität zu untersuchen.

Kornvergrößerungsuntersuchungen zeigten eine sehr hohe Stabilität des nanokristallinen Zustands bis zu einer Temperatur von ca. 500 °C. Zusätzlich tritt ab etwa 600 °C ein Lösen von verbleibendem (reinen) W aus der mechanischen Mischung in den Ni(W)-Mischkristall auf; eine Sättigungskonzentration von gelöstem W in Ni von 12 At. % wird bei ca. 800 °C erreicht. Die Änderung des Gitterparameters der Ni-W Festkörperlösung mit zunehmender Konzentration von W führte zu einer ausgeprägten, asymmetrischen Verbreiterung der Beugungsreflexe.

Ein Vergleich der isothermen Kornwachstumskinetik von reinem kugelgemahlenem Ni mit der Ni(W) Festkörperlösung zeigt, dass die relative thermische Stabilität der Ni(W) Festkörperlösung viel ausgeprägter ist (siehe Abb. 6.3). Desweiteren kam es auch in dieser Ni(W) Festkörperlösung zum Auftreten einer „Sättigungs“-Korngröße und eines ähnlichen Anstiegs derselben mit zunehmender Glühzeit, wie bei reinem Ni (vgl. auch Kapitel 3).

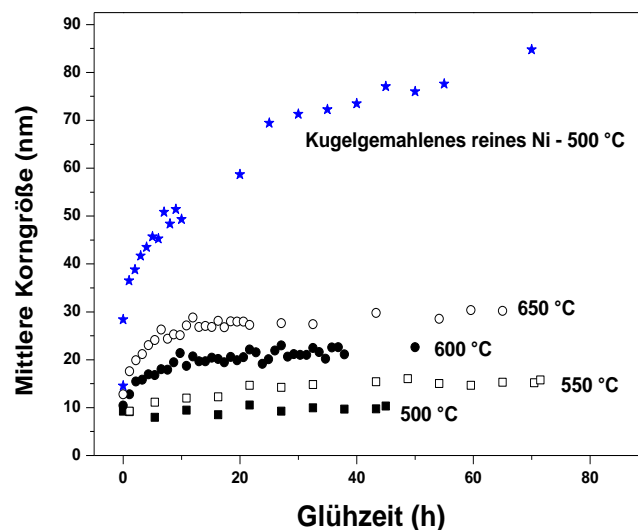


Abb. 6.3: Entwicklung der Kristallitgröße der Ni(W) Festkörperlösung mit hohem W-Gehalt (für weitere Details, siehe Kapitel 4) beim isothermen Glühen. In der Abb. ist auch die mikrostrukturelle Entwicklung von reinem Ni (★ Datenpunkte) dargestellt, welches unter identischen Bedingungen gemahlen wurde und eine sehr ähnliche anfängliche Mikrostruktur aufwies wie die Ni(W) Festkörperlösung.

Die hohe Stabilität der Ni(W) Festkörperlösung kann durch eine Kombination der Reduzierung der Korngrenzenenergie durch W Segregation (d.h. die Triebkraft für Kornwachstum wird verringert) und ein Ansteigen der Aktivierungsenergie für die Korngrenzenbeweglichkeit erklärt werden.

References

- [1] Faraday M. *Philosophical Transactions of the Royal Society London* 1857;147:145.
- [2] Suryanarayana C, Mukhopadhyay D, Patankar SN, Froes FH. *Journal of Materials Research* 1992;7:2114.
- [3] Birringer R. *Mater. Sci. Eng. A-Struct. Mater. Prop. Microstruct. Process.* 1989;117:33.
- [4] Gleiter H. *Prog. Mater. Sci.* 1989;33:223.
- [5] Siegel RW. *MRS Bull.* 1990;15:60.
- [6] Kumar KS, Van Swygenhoven H, Suresh S. *Acta Materialia* 2003;51:5743.
- [7] Chen CQ, Shi Y, Zhang YS, Zhu J, Yan YJ. *Physical Review Letters* 2006;96:075505.
- [8] Youssef KM, Scattergood RO, Murty KL, Koch CC. *Appl. Phys. Lett.* 2004;85:929.
- [9] Lu L, Sui ML, Lu K. *Science* 2000;287:1463.
- [10] Mintova S, Olson NH, Valtchev V, Bein T. *Science* 1999;283:958.
- [11] Horch S, Lorensen HT, Helveg S, Laegsgaard E, Stensgaard I, Jacobsen KW, Norskov JK, Besenbacher F. *Nature* 1999;398:134.
- [12] Suryanarayana C, Koch CC. *Hyperfine Interact.* 2000;130:5.
- [13] Kneller EF, Luborsky FE. *J Appl Phys* 1963;34:656.
- [14] Hernando A, Marin P, Lopez M, Kulik T, Varga LK, Hadjipanayis G. *Phys Rev B* 2004;69.
- [15] Lai SL, Guo JY, Petrova V, Ramanath G, Allen LH. *Physical Review Letters* 1996;77:99.
- [16] Suryanarayana C. *Int. Mater. Rev.* 1995;40:41.
- [17] Meyers MA, Mishra A, Benson DJ. *Prog. Mater. Sci.* 2006;51:427.
- [18] Palumbo G, Thorpe SJ, Aust KT. *Scr. Metall. Materialia* 1990;24:1347.
- [19] Gleiter H. *Acta Materialia* 2000;48:1.
- [20] Zhou Y, Erb U, Aust KT, Palumbo G. *Scr. Mater.* 2003;48:825.
- [21] Ovid'ko IA, Sheinerman AG. *Rev. Adv. Mater. Sci.* 2004;6:41.
- [22] Chen Y, Schuh CA. *Phys Rev B* 2007;76:064111.
- [23] Valerie R. *Acta Materialia* 2004;52:4067.
- [24] Kumar M, King WE, Schwartz AJ. *Acta Materialia* 2000;48:2081.
- [25] Koch C, Ovid'ko I, Seal S, Veprek S. *Structural Nanocrystalline Materials* Cambridge University Press, 2007.
- [26] Siegel RW. *Processing of Metals and Alloys*. In: Cahn RW, Haasen P, Kramer EJ, editors. VCH, Weinheim, 1991. p.583.
- [27] Xu T, Li M. *Philosophical Magazine* 2010;90:2191.
- [28] Siegel RW. *Mater. Sci. Forum* 1997;235–238:851.
- [29] Yip S. *Nature* 1998;391:532.
- [30] Yamakov V, Wolf D, Phillpot SR, Mukherjee AK, Gleiter H. *Nat Mater* 2002;1:45.
- [31] Van Swygenhoven H, Derlet PM, Froseth AG. *Nat Mater* 2004;3:399.

- [32] Schiotz J, Di Tolla FD, Jacobsen KW. *Nature* 1998;391:561.
- [33] Yamakov V, Wolf D, Salazar M, Phillpot SR, Gleiter H. *Acta Materialia* 2001;49:2713.
- [34] Wang J, Duan HL, Huang ZP, Karihaloo BL. *Proceedings of the Royal Society a-Mathematical Physical and Engineering Sciences* 2006;462:1355.
- [35] Wohlschlogel M, Welzel U, Mittemeijer EJ. *Appl. Phys. Lett.* 2007;91.
- [36] Qin W, Nagase T, Umakoshi Y. *J Appl Phys* 2007;102:124303.
- [37] Gärtner F, Bormann R, Birringer R, Tschöpe A. *Scr. Mater.* 1996;35:805.
- [38] Kirchheim R, Huang XY, Cui P, Birringer R, Gleiter H. *Nanostructured Materials* 1992;1:167.
- [39] Fecht HJ. *Physical Review Letters* 1990;65:610.
- [40] Smithells CJ, Brandes EA, Brook GB. *Smithells metals reference book: Butterworth-Heinemann, BH, 1999.*
- [41] Ohta Y, Finnis MW, Pettifor DG, Sutton AP. *Journal of Physics F-Metal Physics* 1987;17:L273.
- [42] Fecht H, Hellstern E, Fu Z, Johnson W. *Metallurgical and Materials Transactions A* 1990;21:2333.
- [43] Ovid'Ko IA, Sheinerman AG. *Philosophical Magazine* 2003;83:1551.
- [44] Qin W, Nagase T, Umakoshi Y, Szpunar JA. *J. Phys., Condens. Matter.* 2007;19:8 pp.
- [45] Apai G, Hamilton JF, Stohr J, Thompson A. *Physical Review Letters* 1979;43:165.
- [46] Mays CW, Vermaak JS, Kuhlmann.D. *Surface Science* 1968;12:134.
- [47] Yu XF, Liu X, Zhang K, Hu ZQ. *Journal of Physics-Condensed Matter* 1999;11:937.
- [48] Chatterjee PP, Pabi SK, Manna I. *J Appl Phys* 1999;86:5912.
- [49] Wang ZM, Wang JY, Jeurgens LPH, Phillipp F, Mittemeijer EJ. *Acta Materialia* 2008;56:5047.
- [50] Birringer R, Zimmer P. *Acta Materialia* 2009;57:1703.
- [51] Lamparter P, Mittemeijer EJ. *International Journal of Materials Research* 2007;98:485.
- [52] Gamarnik MY. *Phys Status Solidi B* 1991;168:389.
- [53] Okram GS, Devi KN, Sanatombi H, Soni A, Ganesan V, Phase DM. *J. Nanosci. Nanotechno.* 2008;8:4127.
- [54] Liu XD, Zhang HY, Lu K, Hu ZQ. *Journal of Physics Condensed Matter* 1994;6:L497.
- [55] Heinemann K, Poppa H. *Surface Science* 1985;156:265.
- [56] Gamarnik MY. *Phys Status Solidi B* 1991;164:107.
- [57] Vermaak JS, Mays CW, Kuhlmann D. *Surface Science* 1968;12:128.
- [58] Lu K, Sui ML. *Scripta Metall. Mater.* 1993;28:1465.
- [59] Lu K, Sun NX. *Philosophical Magazine Letters* 1997;75:389.
- [60] Qin W, Chen ZH, Huang PY, Zhuang YH. *Journal of Alloys and Compounds* 1999;292:230.
- [61] Perebeinos V, Chan SW, Zhang F. *Solid State Communications* 2002;123:295.
- [62] Burke JE, Turnbull D. *Recrystallization and grain growth, 1952.*

-
- [63] Natter H, Schmelzer M, Löffler MS, Krill CE, Fitch A, Hempelmann R. *Journal of Physical Chemistry B* 2000;104:2467.
- [64] Malow TR, Koch CC. *Acta Materialia* 1997;45:2177.
- [65] Koch CC, Ovid'ko IA, Seal S, Veprek S. *Structural Nanocrystalline Materials - Fundamentals and Applications*. Cambridge University Press, 2007.
- [66] Suryanarayana C. *JOM Journal of the Minerals, Metals and Materials Society* 2002;54:24.
- [67] Song XY, Yang KY, Zhang JX. *J. Nanosci. Nanotechnol.* 2005;5:2155.
- [68] Ames M, Markmann J, Karos R, Michels A, Tschöpe A, Birringer R. *Acta Materialia* 2008;56:4255.
- [69] Ovid'ko IA. *Philosophical Magazine Letters* 2003;83:611.
- [70] Krill CE, Helfen L, Michels D, Natter H, Fitch A, Masson O, Birringer R. *Physical Review Letters* 2001;86:842.
- [71] Steinbach I, Song XY, Hartmaier A. *Philosophical Magazine* 2010;90:485.
- [72] Zollner D, Streitenberger P. Computer simulations and statistical theory of normal grain growth in two and three dimensions. In: Bacroix B, Driver JH, LeGall R, Maurice C, Penelle R, Regle H, Tabourot L, editors. *Recrystallization and Grain Growth, Pts 1 and 2*, vol. 467-470. Zurich-Uetikon: Trans Tech Publications Ltd, 2004. p.1129.
- [73] Anderson MP, Grest GS, Srolovitz DJ. *Philos. Mag. B-Phys. Condens. Matter Stat. Mech. Electron. Opt. Magn. Prop.* 1989;59:293.
- [74] Haslam AJ, Moldovan D, Phillpot SR, Wolf D, Gleiter H. *Comput. Mater. Sci.* 2002;23:15.
- [75] Czubayko U, Sursaeva VG, Gottstein G, Shvindlerman LS. *Acta Materialia* 1998;46:5863.
- [76] Gottstein G, Shvindlerman LS. *Scr. Mater.* 2006;54:1065.
- [77] Upmanyu M, Srolovitz DJ, Shvindlerman LS, Gottstein G. *Interface Science* 1998;6:287.
- [78] Estrin Y, Gottstein G, Shvindlerman LS. *Scr. Mater.* 1999;41:385.
- [79] Paul H, Krill CE, III. *Scr. Mater.* 2011;65:5.
- [80] Zhou F, Lee J, Lavernia EJ. *Scr. Mater.* 2001;44:2013.
- [81] Choi P, da Silva M, Klement U, Al-Kassab T, Kirchheim R. *Acta Materialia* 2005;53:4473.
- [82] Boylan K, Ostrander D, Erb U, Palumbo G, Aust KT. *Scr. Metall. Materialia* 1991;25:2711.
- [83] Shvindlerman LS, Gottstein G. *Zeitschrift Fur Metallkunde* 2004;95:239.
- [84] Michels A, Krill CE, Ehrhardt H, Birringer R, Wu DT. *Acta Materialia* 1999;47:2143.
- [85] Beke DL, Cserhati C, Szabo IA. *J Appl Phys* 2004;95:4996.
- [86] Kirchheim R. *Acta Materialia* 2002;50:413.
- [87] Krill CE, Ehrhardt H, Birringer R. *Zeitschrift Fur Metallkunde* 2005;96:1134.
- [88] Younes-Metzler O, Zhu L, Gileadi E. *Electrochimica Acta* 2003;48:2551.
- [89] Yao S, Zhao S, Guo H, Kowaka M. *Corrosion* 1996;52:183.
- [90] Osada M, Maeda K, Kawamoto Y, Shimizu Y, Nishimura T, Yamaharu S. US patent 2004 No. 6,773,247.

- [91] SGTE Landolt-Börnstein - Group IV Physical Chemistry. Springer-Verlag Berlin and Heidelberg GmbH & Co. KG., 2006.
- [92] Klug HP, Alexander LE. X-ray diffraction procedures for polycrystalline and amorphous materials: Wiley, 1974.
- [93] Warren BE. X-ray Diffraction: Addison-Wesley, Reading MA, 1969.
- [94] Mittemeijer EJ, Scardi P, editors. Diffraction Analysis of the Microstructure of Materials. . Germany: Springer, 2004.
- [95] Mittemeijer EJ, Welzel U. Z. Kristallogr 2008;223:552.
- [96] Delhez R, dekeijser TH, Mittemeijer EJ. Fresenius Zeitschrift Fur Analytische Chemie 1982;312:1.
- [97] Williamson GK, Hall WH. Acta Metallurgica 1953;1:22.
- [98] Scardi P, Leoni M, Delhez R. J. Appl. Crystallogr. 2004;37:381.
- [99] Delhez R, de Keijser TH, Mittemeijer EJ. Fresenius' Zeitschrift für Analytische Chemie 1982;312:1.
- [100] Warren BE, Averbach BL. J Appl Phys 1950;21:595.
- [101] Warren BE, Averbach BL. J Appl Phys 1952;23:497.
- [102] van Berkum JGM, Vermeulen AC, Delhez R, de Keijser TH, Mittemeijer EJ. J. Appl. Crystallogr. 1994;27:345.
- [103] Scardi P, Leoni M. Whole powder pattern modelling: Theory and applications. Diffraction Analysis of the Microstructure of Materials, vol. 68. Berlin: Springer-Verlag Berlin, 2004. p.51.
- [104] Wolf D, Yamakov V. MD Simulation of Deformation Mechanisms in Nanocrystalline Materials: Wiley-VCH Verlag GmbH & Co. KGaA, 2009.
- [105] Yamakov V, Wolf D, Phillpot SR, Mukherjee AK, Gleiter H. Philosophical Magazine Letters 2003;83:385
- [106] Gutkin MY, Ovid'ko IA, Pande CS. Rev. Adv. Mater. Sci. 2001;2:80.
- [107] Zehetbauer MJ, Zhu YT, editors. Bulk Nanostructured Materials: Wiley-VCH Verlag GmbH & Co. KGaA, Weinheim, Germany, 2009.
- [108] Kuru Y, Wohlschlogel M, Welzel U, Mittemeijer EJ. Appl. Phys. Lett. 2007;90.
- [109] Schaefer HE, Würschum R, Birringer R, Gleiter H. Journal of the Less Common Metals 1988;140:161.
- [110] Fecht HJ. Acta Metallurgica Et Materialia 1990;38:1927.
- [111] Wagner M. Phys Rev B 1992;45:635.
- [112] Zhao YH, Sheng HW, Lu K. Acta Materialia 2001;49:365.
- [113] Wunderlich W, Ishida Y, Maurer R. Scr. Metall. Materialia 1990;24:403.
- [114] Divakar R, Raghunathan VS. Sadhana-Acad P Eng S 2003;28:47.
- [115] Haubold T, Birringer R, Lengeler B, Gleiter H. Physics Letters A 1989;135:461.
- [116] Vermaak JS, Mays CW, Kuhlmann-Wilsdorf D. Surface Science 1968;12:128.

-
- [117] Lu K, Sui ML. *Scripta Metallurgica et Materiala* 1993;28:1465.
- [118] Liu XD, Zhang HY, Lu K, Hu ZQ. *Journal of Physics Condensed Matter* 1994;6:L497.
- [119] Birringer R, Hoffmann M, Zimmer P. *Physical Review Letters* 2002;88.
- [120] Banerjee R, Sperling EA, Thompson GB, Fraser HL, Bose S, Ayyub P. *Appl. Phys. Lett.* 2003;82:4250.
- [121] Gaffet E, Harmelin M. *Journal of The Less-Common Metals* 1990;157:201.
- [122] Gaffet E. *Materials Science and Engineering A* 1991;136:161.
- [123] Eastman JA, Fitzsimmons MR. *J Appl Phys* 1995;77:522.
- [124] Eastman JA, Fitzsimmons MR, Thompson LJ. *Philos. Mag. B-Phys. Condens. Matter Stat. Mech. Electron. Opt. Magn. Prop.* 1992;66:667.
- [125] Zirnmer P, Birringer R. *Appl. Phys. Lett.* 2008;92.
- [126] Zhang K, Alexandrov IV, Valiev RZ, Lu K. *J Appl Phys* 1996;80:5617.
- [127] Sheng J, Welzel U, Mittemeijer EJ. *Appl. Phys. Lett.* 2010;97.
- [128] Apai G, Hamilton JF, Stohr J, Thompson A. *Physical Review Letters* 1979;43:165.
- [129] Sheng J, Rane G, Welzel U, Mittemeijer EJ. *Physica E: Low-dimensional Systems and Nanostructures* 2011;43:1155.
- [130] Gibbs JW. *Collected Works: Longmans, Green, and Company, Inc., New York., 1928.*
- [131] Solliard C, Flueli M. *Surface Science* 1985;156:487.
- [132] Wang J, Xing J, Qiu Z, Zhi X, Cao L. *Journal of Alloys and Compounds* 2009;488:117.
- [133] Li ZQ, et al. *Journal of Physics D: Applied Physics* 1996;29:1373.
- [134] Zhang BQ, Lu L, Lai MO. *Physica B-Condensed Matter* 2003;325:120.
- [135] Seitz F. *Adv. Phys.* 1952;1:43.
- [136] Ovid'ko IA, Reizis AB. *Physics of the Solid State* 2001;43:35.
- [137] Xiao W, Liu CS, Tian ZX, Geng WT. *J Appl Phys* 2008;104:053519.
- [138] Gottstein G, Shvindlermann LS. *Grain Boundary Migration in Metals: Thermodynamics, Kinetics, Applications: CRC Press, Boca Raton, Florida, 1999.*
- [139] Hull D, Rimmer DE. *Philosophical Magazine* 1959;4:673
- [140] Van Petegem S, Dalla Torre F, Segers D, Van Swygenhoven H. *Scr. Mater.* 2003;48:17.
- [141] Schaefer HE, Wurschum R, Birringer R, Gleiter H. *Phys Rev B* 1988;38:9545.
- [142] Zehetbauer MJ, Steiner G, Schafler E, Korznikov A, Korznikova E. *Nanomaterials by Severe Plastic Deformation* 2006;503-504:57.
- [143] Lu K, Zhao YH. *Nanostructured Materials* 1999;12:559.
- [144] Fecht HJ. *Physical Review Letters* 1990;65:610.
- [145] Baretzky B, Baro MD, Grabovetskaya GP, Gubicza J, Ivanov MB, Kolobov YR, Langdon TG, Lendvai J, Lipnitskii AG, Mazilkin AA, Nazarov AA, Nogues J, Ovidko IA, Protasova SG, Raab GI, Revesz A, Skiba NV, Sort J, Starink MJ, Straumal BB, Surinach S, Ungar T, Zhilyaev AP. *Rev. Adv. Mater. Sci.* 2005;9:45.
- [146] Nazarov AA, Romanov AE, Valiev RZ. *Acta Metallurgica Et Materialia* 1993;41:1033.

- [147] Qin W, Szpunar JA. *Philosophical Magazine Letters* 2005;85:649.
- [148] Eshelby JD, (editors), Smallman RE, Harris JE. *Vacancies '76*, The Metals Society, London.:3.
- [149] Chattopadhyay PP, Nambissan PMG, Pabi SK, Manna I. *Physical Review B (Condensed Matter)* 2001;63:054107/1.
- [150] Prenitzer BI, Giannuzzi LA, Newman K, Brown SR, Irwin RB, Shofner TL, Stevie FA. *Metallurgical and Materials Transactions A: Physical Metallurgy and Materials Science* 1998;29:2399.
- [151] ProFit for Windows. User's Guide Philips Analytical X-ray 1996.
- [152] Welzel U, Mittemeijer EJ. *Powder Diffr.* 2005;20:376.
- [153] Welzel U. *International Journal of Materials Research* 2011;102:846.
- [154] dekeijser TH, Langford JI, Mittemeijer EJ, Vogels ABP. *J. Appl. Crystallogr.* 1982;15:308.
- [155] Paterson MS. *J Appl Phys* 1952;23:805.
- [156] Warren BE. *X-ray Diffraction: Addison-Wesley, New York, 1990.*
- [157] Wagner CNJ. *Local atomic arrangements studied by X-ray diffraction: Gordon and Breach, New York 1966.*
- [158] Klug HP, Alexander LE. *X-ray Diffraction Procedures: John Wiley and Sons, New York, 1974.*
- [159] Suryanarayana C. *Prog. Mater. Sci.* 2001;46:1.
- [160] Eckert J, Holzer JC, Krill CE, Johnson WL. *Journal of Materials Research* 1992;7:1751.
- [161] Brandl C, Derlet PM, Van Swygenhoven H. *Phys Rev B* 2007;76:054124.
- [162] Michels D, Krill CE, Brunelli M, Birringer R. In: *Verhandl. DPG (VI) 39, 2/2004, D.*
- [163] Wolf D, Yamakov V, Phillpot SR, Mukherjee A, Gleiter H. *Acta Materialia* 2005;53:1.
- [164] Mittemeijer EJ. *Fundamentals of Materials Science: Springer, 2010.*
- [165] Pantleon K, Somers MAJ. *J Appl Phys* 2006;100.
- [166] Gottstein G, Shvindlerman LS. *Acta Materialia* 2002;50:703.
- [167] Estrin Y. *Vacancy effects in grain growth. Berlin: Springer-Verlag Berlin, 2001.*
- [168] Estrin Y, Gottstein G, Rabkin E, Shvindlerman LS. *Scr. Mater.* 2000;43:141.
- [169] Koch CC. *Nanostructured Materials* 1993;2:109.
- [170] Schaefer HE, Wurschum R, Gessmann T, Stockl G, Scharwaechter P, Frank W, Valiev RZ, Fecht HJ, Moelle C. *Nanostructured Materials* 1995;6:869.
- [171] Kolobov YR, Grabovetskaya GP, Ratochka IV, Ivanov KV. *Nanostructured Materials* 1999;12:1127.
- [172] Révész Á, Ungár T, Borbély A, Lendvai J. *Nanostructured Materials* 1996;7:779.
- [173] Moelle CH, Fecht HJ. *Nanostructured Materials* 1995;6:421.
- [174] Estrin Y, Gottstein G, Shvindlerman LS. *Scripta Materialia* 1999;41:385.
- [175] Humphreys FJ, Hatherly M. *Recrystallization and Related Annealing Phenomena: Pergamon Press: Oxford, 1996.*

-
- [176] Grey EA, Higgins GT. *Acta Metallurgica* 1973;21:309.
- [177] Langford JI, Wilson AJC. *J. Appl. Crystallogr.* 1978;11:102.
- [178] Scardi P, Leoni M. *J. Appl. Crystallogr.* 2006;39:24.
- [179] Scardi P, Leoni M, D'Incau M. *Z. Kristallogr* 2007;222:129.
- [180] Scardi P. Chapter 13 Microstructural Properties: Lattice Defects and Domain Size Effects. *Powder Diffraction: Theory and Practice*. The Royal Society of Chemistry, 2008. p.376.
- [181] Warren BE. *Progress in Metal Physics* 1959;8:147.
- [182] Delhez R, Mittemeijer EJ. *J. Appl. Crystallogr.* 1976;9:233.
- [183] Bertaut EF. *Acta Crystallographica* 1952;5:117.
- [184] Balzar D. *J. Appl. Crystallogr.* 1992;25:559.
- [185] Krill CE, Birringer R. *Philos. Mag. A-Phys. Condens. Matter Struct. Defect Mech. Prop.* 1998;77:621.
- [186] Balzar D, Ledbetter H. *J. Appl. Crystallogr.* 1993;26:97.
- [187] Ovid'ko IA. *Int. Mater. Rev.* 2005;50:65.
- [188] Landolt-Börnstein Database. Springer-Verlag Berlin and Heidelberg GmbH & Co. KG., 2006.
- [189] Chokshi AH. *Scr. Mater.* 2008;59:726.
- [190] Kuru Y, Wohlschlogel M, Welzel U, Mittemeijer EJ. *Appl. Phys. Lett.* 2009;95.
- [191] Meyers MA, Mishra A, Benson DJ. *JOM* 2006;58:41.
- [192] Meyers MA, Mishra A, Benson DJ. *Prog. Mater. Sci.* 2006;51:427.
- [193] Croat JJ, Herbst JF, Lee RW, Pinkerton FE. *J Appl Phys* 1984;55:2078.
- [194] Koch C, Scattergood R, Darling K, Semones J. *Journal of Materials Science* 2008;43:7264.
- [195] Murty BS, Ranganathan S. *Int. Mater. Rev.* 1998;43:101.
- [196] Detor AJ, Schuh CA. *Journal of Materials Research* 2007;22:3233.
- [197] Hansen K, Pantleon K. *Scr. Mater.* 2008;58:96.
- [198] Ames M, Markmann J, Karos R, Michels A, Tschoepe A, Birringer R. *Acta Materialia* 2008;56:4255.
- [199] Weissmüller J. *Nanostructured Materials* 1993;3:261.
- [200] Liu F, Kirchheim R. *Journal of Crystal Growth* 2004;264:385.
- [201] Liu KW, Mücklich F. *Acta Materialia* 2001;49:395.
- [202] Eckert J, Holzer JC, Johnson WL. *J Appl Phys* 1993;73:131.
- [203] Goyal A, Feenstra R, Paranthaman M, Thompson JR, Kang BY, Cantoni C, Lee DF, List FA, Martin PM, Lara-Curzio E, Stevens C, Kroeger DM, Kowalewski M, Specht ED, Aytug T, Sathyamurthy S, Williams RK, Ericson RE. *Physica C: Superconductivity* 2002;382:251.
- [204] HongLi S, Yue Z, Min L, Lin M, Dong H, YingXiao Z, MeiLing Z. *Applied Superconductivity, IEEE Transactions on* 2007;17:3420.
- [205] Tearney T, Grant N. *Metallurgical and Materials Transactions A* 1982;13:1827.

- [206] Zhou YX, Ghalsasi SV, Hanna M, Tang ZJ, Meng RL, Salama K. Applied Superconductivity, IEEE Transactions on 2007;17:3428.
- [207] Gao MM, et al. Journal of Physics: Conference Series 2010;234:022010.
- [208] Bhattacharjee PP, Ray RK. Materials Science and Engineering: A 2007;459:309.
- [209] Eliaz N, Sridhar TM, Gileadi E. Electrochimica Acta 2005;50:2893.
- [210] Trelewicz JR, Schuh CA. Acta Materialia 2007;55:5948.
- [211] Trelewicz JR, Schuh CA. Phys Rev B 2009;79.
- [212] Yamasaki T. Scr. Mater. 2001;44:1497.
- [213] Welzel U, Kummel J, Bischoff E, Kurz S, Mittemeijer EJ. Journal of Materials Research 2011;26:2558.
- [214] González G, Sagarzazu A, Villalba R, Ochoa J. Journal of Alloys and Compounds 2007;434-435:525.
- [215] Rane GK, Apel D, Welzel U, Mittemeijer EJ. Zeitschrift für Kristallographie Proceedings Nr. 1. 2011;I+II:247.
- [216] Aning AO, Wang Z, Courtney TH. Acta Metallurgica Et Materialia 1993;41:165.
- [217] Detor AJ, Schuh CA. Acta Materialia 2007;55:4221.
- [218] Choi P, Al-Kassab T, Gärtner F, Kreye H, Kirchheim R. Materials Science and Engineering: A 2003;353:74.
- [219] Scardi P, Leoni M. Acta Crystallogr. Sect. A 2002;58:190.
- [220] Biju V, Sugathan N, Vrinda V, Salini SL. Journal of Materials Science 2008;43:1175.
- [221] Rosenberg Y, Machavariani VS, Voronel A, Garber S, Rubshtein A, Frenkel AI, Stern EA. Journal of Physics-Condensed Matter 2000;12:8081.
- [222] Leoni M, Confente T, Scardi P. Z. Kristallogr 2006:249.
- [223] Leineweber A, Mittemeijer EJ. J. Appl. Crystallogr. 2004;37:123.
- [224] Detor AJ, Schuh CA. Acta Materialia 2007;55:371.
- [225] Jang D, Atzmon M. J Appl Phys 2006;99.
- [226] Blázquez JS, Ipus JJ, Millán M, Franco V, Conde A, Oleszak D, Kulik T. Journal of Alloys and Compounds 2009;469:169.
- [227] Suriñach S, Baró MD, Segura J, Clavaguera-Mora MT, Clavaguera N. Materials Science and Engineering: A 1991;134:1368.
- [228] Révész Á, Lendvai J. Nanostructured Materials 1998;10:13.
- [229] Liu YJ, Chang ITH. Acta Materialia 2002;50:2747.
- [230] Qin XY, Wu XJ, Cheng LF. Nanostructured Materials;2:99.
- [231] Zhao KY, Li CJ, Tao JM, Ng DHL, Zhu XK. Journal of Alloys and Compounds 2010;504, Supplement 1:S306.
- [232] Oleszak D, Shingu PH. J Appl Phys 1996;79:2975.

Acknowledgements

The present work was performed at the Max Planck Institute for Intelligent Systems (formerly Max Planck Institute for Metals Research) and at the Institute for Materials Science, University of Stuttgart.

First of all I would like to thank Prof. Dr. Ir. E. J. Mittemeijer for accepting me as a PhD student in his department. His constant guidance and encouragement has been a major source of motivation. With his immense knowledge, timely scientific discussions, suggestions and his openness to scientific thoughts, he has tremendously contributed to the completion of my research work along. Finally, I would like to thank him for writing the main opinion ('Hauptbericht') for the thesis.

I would also like to express my sincere gratitude to Prof. Dr. J. Bill for writing the second opinion ('Mitbericht') for the thesis and to Prof. Dr. T. Schleid for accepting the Chairmanship for the examination committee.

I am immensely thankful to my daily supervisor Dr. U. Welzel for his inestimable guidance. His expertise and suggestions considerably contributed to the successful completion of this work. I would like to thank him also for helping me improve my writing skills by correcting my raw manuscripts and monthly reports. His kind attitude helped me to adjust easily to the work environment.

I am grateful to the International Max Planck Research School for Advanced Materials (IMPRS-AM) for providing financial support.

I thank Holger Selg for assistance with the German translation of the summary of this work and all colleagues in the Department Mittemeijer and the Institute for the cooperation, their help with respect to various technical and scientific questions and the constructive and pleasant working atmosphere. My research and life at the institute would not have been as fulfilling without the support of my colleagues and friends. I would also like to thank all my friends outside the institute (mainly, Saisharmi) for making my stay in Stuttgart memorable.

Finally, I have no words to acknowledge my gratitude to the most important people in my life – My family and friends (especially Vijay Parsi and Rakesh Rao) for their love and support.

Curriculum Vitae

Personal Data

Name Gayatri Koyar Rane
Date of Birth 07.01.1986
Place of Birth Belgaum, Karnataka, India.
Marital Status Single
Nationality Indian

Education

1991 - 2001 Kendriya Vidyalaya. Central Board of Secondary Education, Goa, India
2001 - 2003 Dr. T.B. Cunha Higher Secondary School. Central Board of Secondary Education, Goa, India.

Higher education

2003 – 2006 Bachelor of Science.
Dhempe College of Arts and Science.
Goa University, Goa, India
2006 – 2008 Master of Science (Chemistry)
Goa University, Goa, India

Dissertation

September 2008 – June 2012 Ph.D. student at Max Planck Institute for Intelligent Systems (formerly Max Planck Institute for Metals Research)
Department Prof. Dr. Ir. E. J. Mittemeijer
(International Max Planck Research School – IMPRS)
Universität Stuttgart, Germany.
Thesis title: “Microstructure and grain growth of nanosized materials”.